PHASES AND CRITICAL ANALYSIS OF QUANTUM SYSTEMS IN PRESENCE OF QUASIPERIODIC POTENTIAL

Shilpi Roy

Roll No. - 176121109

Supervisor: Prof. Saurabh Basu

A Thesis Presented to the

Department of Physics

of

Indian Institute of Technology Guwahati

in Partial Fulfillment of the Requirements for the Degree of

Doctor of Philosophy

Department of Physics

Indian Institute of Technology Guwahati

Guwahati-781039, Assam, India

PHASES AND CRITICAL ANALYSIS OF QUANTUM SYSTEMS IN PRESENCE OF QUASIPERIODIC POTENTIAL

Shilpi Roy

Disorder is universal in quantum systems. It has an enormous effect on electronic motion in solids. Consequently, the system undergoes a localization transition from a metal to an insulator under the drive of random disorder strength in three dimensions. On the contrary, another type of deterministic potential, namely, the quasiperiodic (QP) potential allows exhibiting of the localization transition in one-dimensional systems.

In this thesis, our primary motivation is to study the localization properties corresponding to a dimer model in presence of the QP potential. More specifically, the dimer model has been chosen for the purpose of breaking the self-dual symmetry, thereby aiming to introduce mobility edge (ME) in the one-dimensional system. The combination of these two, such as the dimerization and the QP potential, reveals a noteworthy observation. In particular, the results which are analyzed via computing the participation ratio, eigenenergies, density of states and finite-size scaling analysis etc., imply a reentrant localization transition that transcends the existing conventional theory in literature. Further, we analyzed the critical behavior corresponding to this reentrant localization transition using a multifractal analysis, followed by a critical state analysis, and via computing the Hausdorff dimension. Moreover, this dimer model, aided by p-wave superconducting pairing in presence of QP potential, preserves topological properties, which was missing in the purely dimerized model with QP potential. Thus by exploring the localization and the topological properties,

we have reported significant results on a series of phase transitions occurring in the system. While studying the localization properties via participation ratio, fractal dimension and level spacing, we inferred two different types of anomalous MEs in addition to realizing a multifractal phase. Further, by examining the topological properties via calculating the real-space winding number and the number of Majorana zero modes, we observe several phase transitions from topologically trivial to topologically Anderson to Anderson localized phase. In the end, in addition to the non-interacting one-dimensional quantum systems, we have also studied a two-dimensional interacting system in presence of a QP potential. Using the site-decoupled mean-field approximation, percolation analysis and the finite-size scaling analysis, we have explored the phase diagram, and subsequently investigated the critical properties of the various phase transitions occurring in the system.

In memory of my Father

ACKNOWLEDGEMENTS

The years I spent at IITG have been the most exciting, memorable, and transformative period of my life. This would not have been possible without the guidance of my supervisor Prof. Saurabh Basu. His constant support, encouragement, and friendly gestures with kindness remain a great source of motivation from the beginning. Not only I learn how to do research, but his training also teaches me to look the world straight in the eye.

My sincere gratitude also goes to our collaborators, Prof. Tapan Mishra, Dr. Sk Noor Nabi, Dr. Sourav Chattopadhyay, Prof. Ivan M Khaymovich, and Prof. Bilal Tanatar. Their valuable suggestions and insightful comments have helped me to improve my understanding of the field.

I am also grateful to my Doctoral Committee members for their helpful suggestions from time to time, which aided in further improving the quality of my research work.

I would like to thank my seniors and present group members, particularly Sudin da, Noor da, Priyadarshini di, Sunayana di, Priyanka di, Sayan, Mijanur, Dipendu, Srijata, Koustav, and Shreya, for their support and cooperation. My special thanks go to Sayan for his consistent support in uncountable ways.

I am also grateful to Sourav da for his kind and friendly support in every step of my research and personal life. His enormous computation skills and profoundly calm personality can fascinate anyone. I am not an exception here.

Moreover, I would like to thank my family members. With all my heart, I would like to thank my parents. The place I come from took a lot of work for them to support a daughter this far. Without their support, it would not be achievable. I am also thankful to Dada, Anamika, and Ayush.

I would like to give a special thanks to Rituparna, Mandira, Sayan and San-

ket for making my graduate years so memorable. Campus life would not be so easy and enjoyable without your presence.

I would like to give my special thanks to Esha for understanding me on every good or bad day, month, and year. I can not thank enough for being my side in every possible way as my best friend.

Last but not least, I would like to thank myself for trying to be the best version of myself and for aiming toward becoming a human being first.

DISCLAIMER

The bibliography included in this thesis is, by no means complete but contains the ones which are consulted thoroughly by me. I apologize for inadvertently missing out some of the research papers, review articles, and other scientific documents pertaining to the focus of this thesis which should also have been cited. For illustration purpose some of the figures in this thesis are taken from other sources and properly cited.

CERTIFICATE

This is to certify that the work contained in the thesis entitled "*Phases and Critical Analysis of Quantum Systems in presence of Quasiperiodic Potential*" by Ms. Shilpi Roy (Roll no.-176121109), a Ph.D. student of the Department of Physics, Indian Institute of Technology Guwahati is carried out under my supervision and has not been submitted elsewhere for the award of any other degree.

Saurabh Basu
Department of Physics
Indian Institute of Technology Guwahati Guwahati - 781039

DECLARATION

The work in this thesis entitled "*Phases and Critical Analysis of Quantum Systems in presence of Quasiperiodic Potential*" has been carried out by me under the supervision of Prof. Saurabh Basu, Department of Physics, Indian Institute of Technology Guwahati. No part of this thesis has been submitted elsewhere for award of any other degree or qualification. The research work has been carried out during the period from January, 2018 to January, 2023. In keeping with general practice of reporting scientific observations, due acknowledgments have been made wherever the work described is based on the findings of other investigations.

Shilpi Roy
Department of Physics
Indian Institute of Technology Guwahati Guwahati - 781039

LIST OF PUBLICATIONS

The following are described in this thesis:

1. *Interplay of off-diagonal random disorder and quasiperiodic potential in a one-dimensional Aubry-André model*,

   Shilpi Roy and S. Basu

   EPL (Europhysics Letters) **128** (4), 47005 (2020).

2. *Reentrant Localization Transition in a Quasiperiodic Chain*,

   Shilpi Roy, Tapan Mishra, B. Tanatar, and Saurabh Basu

   Phys. Rev. Lett. **126**, 106803 (2021).

3. *Critical analysis of the reentrant localization transition in a one-dimensional dimerized quasiperiodic lattice*,

   Shilpi Roy, Sourav Chattopadhyay, Tapan Mishra, and Saurabh Basu

   Phys. Rev. B **105**, 214203 (2022).

4. *Phase Properties of Interacting Bosons in Presence of Quasiperiodic Disorder*,

   Sk Noor Nabi, **Shilpi Roy**, and Saurabh Basu

   Annals of Physics **448**, 169171 (2023).

5. *Critical and Topological Phases of Dimerized Kitaev Chain in Presence of Quasiperiodic Potential*,

   Shilpi Roy, Sk Noor Nabi, and Saurabh Basu

   Phys. Rev. B **107**, 014202 (2023)..

The following is not described in this thesis:

1. *Localization and ergodicity breaking in long-range self-dual models with correlated disorder*,

   Shilpi Roy, Saurabh Basu, and Ivan M. Khaymovich

   in preparation (2023)

Conference Attended

1. Oral presentation at 3**rd National Conference on Frontiers of Modern Physics (NCFMP** 2021**)** , on 26th and 27th November, 2021 (organized by the Department of Physics School of basic and Applied Sciences, Adamas University).
2. Oral presentation at **Annual Conference on Quantum Condensed Matter (QMAT 2022)**, on 18th to 22th September, 2022 (organized by Department of Physics, IIT Kanpur).
3. Poster presentation at **Emergence Phenomena in Quantum Materials (E-QMAT)** on 12th to 14th October, 2022 (organized by Department of Physics, IIT Roorkee), will be published in IOP Conference Proceedings.

CURRICULUM VITAE

Shilpi Roy was born on 3rd January 1993, in West Bengal, India. She did her B. Sc. with physics honors in 2013 from the University of Calcutta and her M.Sc in physics in 2015 from the University of Delhi. She had enrolled in the Ph.D. program at the Indian Institute of Technology Guwahati in 2018 (January). She had qualified for CSIR-UGC NET in 2016, Joint Entrance Screening Test (JEST) in 2017, and Graduate Aptitude Test in Engineering (GATE) in 2017.

TABLE OF CONTENTS

LIST OF TABLES

LIST OF FIGURES

CHAPTER 1

INTRODUCTION

The study of electronic transport properties in quantum systems is a topic under constant focus in condensed matter physics. The understanding of electronic transport in the presence of periodic potential is well established. In such systems, the solution of the Schrödinger equation follows the Bloch theorem [9]. Thus, the resulting eigenstates spread uniformly over the entire lattice, yielding a metallic behavior by the systems. However, disorder is ubiquitous in materials, which enormously affects the experimental results. Thus, the question arises, what will happen to the motion of electrons in the non-interacting systems in presence of in-homogeneous or non-periodic background? According to general perception, the conductivity should decay with the strength of disorder present in the system. This problem was solved by P. W. Anderson and discovered a very unusual phenomenon [10]. This phenomenon emerges as a complete vanishing of the conductivity beyond a critical disorder strength, irrespective of the kinetic energy of the electrons. Later, this is known as Anderson localization (AL), leading to the metal-insulator transition in random disorder systems. Further, the scaling theory of localization developed by Abrahams, Anderson, Licciardello, and Ramakrishnan allows exploring the dimensional dependency of the localization transition [11]. Consequently, it is illustrated that the AL transition (i.e., metal-insulator transition) occurs only in a system dimension higher than two [12, 13]. On the other hand, there is a complete localization exhibit corresponding to all the single-particle eigenstates for one and two-dimensional systems. However, studying the localization transition remains challenging due to the process of disorder averaging in numeric computation, especially for large systems and the inability to treat disorder as a

controllable quantity in physical systems.

The discovery of ultracold atoms in optical lattices provides an enormous opportunity to recreate the AL transition in the lab. In 2008, Billy et al. first observed this phenomenon in an experiment using the speckle potential in an optical lattice [1]. At the same time, there is an experiment reported by Roati et al. to observe AL using quasiperiodic (QP) potential [4]. This potential can be generated by superposing two or more optical potentials corresponding to two incommensurate wavelengths [14, 15, 16]. Most interestingly, a localization transition occurs in presence of QP potential in one-dimensional system, and thus is in sharp contrast to the random potential.

The QP potential belongs to the intermediate regime of periodic and random potential, yielding a deterministic nature [17]. A paradigmatic model to study quantum transport in the presence of QP potential is the Aubry-André (AA) model [18]. The model shows a phase transition from a metal to an insulator through a critical transition point. The transition can be understood by a fascinating property known as the self-duality. The self-dual point also coincides with that of the Harper model [19]. The Harper model was introduced in a two-dimensional lattice model in presence of perpendicular magnetic field. The energy spectrum of the model was studied by Hofstadter [20] who showed a self-similar structure of the energy spectrum to emerge in presence of an external magnetic field. The structure is known as the "Hofstadter Butterfly". However, the breaking of the self duality of the AA model, or further generalizations of it have shown to exhibit the localization transition associated with more involved physics [21, 22, 23, 24, 25, 26, 27, 28, 29, 30, 31, 32, 33, 34].

Subsequently, in a certain generalized AA model, and in other quasiperiodic

systems the transitions from the extended to the localized phases are often associated with a critical region where both the extended and the localized states coexist [35, 36, 37, 38]. The key feature of this critical region is the existence of mobility edge (ME) which corresponds to a critical energy separating the extended and the localized states of the system [12]. Due to the recent progress in the field of quantum gases in optical lattices, realizing localization transition, and exploring the possible existence of the ME in quasiperiodic systems have gained considerable interest [39, 15, 36, 40, 31, 16, 41, 37, 42, 43, 44] leading to their recent experimental observations [45, 46, 47, 48, 49]. It is known that the eigenstates at the mobility edge are multifractal in nature [50]. Interestingly, a QP potential can host regimes comprising of critical (multifractal) states in a wide range of parameter space, leading to a multifractal phase [35, 51, 22, 52, 53]. These multifractal states are fundamentally different from the extended and the localized states, thereby making it feasible to explore new opportunities in different branches of physics, such as, non-ergodic physics, Anderson localization transition, and transport properties of the systems at the critical point etc. [50, 54, 55]. Conventionally, the mobility edge is considered as a critical point between the extended and the localized states. However, some works have reported different kinds of mobility edges that are realized intervening the multifractal and the extended phases, and also between the multifractal and the localized phases [51, 22].

Apart from the localization transition in 1D, this potential offers a range of interesting physics, including critical eigenstaes behavior [50, 26, 25, 56, 57, 58, 24, 59, 23, 60, 22], fractal (self-similar) energy spectra [59, 61], many-body-localization [54, 62, 63, 64], and topology [65, 66, 67] which have been studied in great detail in a variety of systems [68]. The potential is found in a vast area

of systems, such as optical lattices [4, 49, 14, 21, 69, 60, 48], photonic crystals [70, 71, 72, 73, 74], phononic medium [75, 76], cavity polaritons [77, 78], Moiré lattices [79], superconducting circuits [80] etc.

1.1 Tight binding model

The study of electronic transport properties in a solid-state material is one of the focused topics in condensed matter physics. Generally, the motion of the carriers in materials is described by a suitable theoretical model, which allows for analyzing the properties of the material. Tight-binding model is one of such model which accounts for the motion in the presence of atomic or ionic potentials; however, it excludes inter-particle interactions. In this model, the electrons are assumed to be bound to the core of the atoms, resulting in assigned discrete atomic sites. Therefore, the tight-binding approximation holds only for the lower atomic orbitals.

Let us demonstrate the utility of the tight binding model in the simplest situation, namely a one-dimensional (1D) chain with L number of atoms in Fig. 1.1.

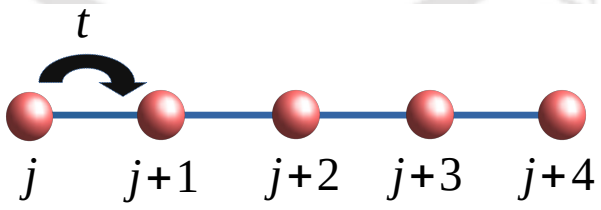

Figure 1.1: A one-dimensional lattice with the nearest-neighbor hopping strength t is shown here.

The corresponding Hamiltonian is given by,

$$H = t\sum_{j=1}^{L}(\hat{c}_{j+1}^{\dagger}\hat{c}_j + \text{h.c.}) + \sum_{j=1}^{L} V_j \hat{c}_j^{\dagger}\hat{c}_j \tag{1.1}$$

where t is the nearest-neighbor tunneling strength. The creation (annihilation) operator to create (destroy) an electron at site j is given by $c_j^{\dagger}$ (c_j). The onsite potential, due to the (periodic) presence of the atoms, is represented by V_j. The atomic orbitals are chosen as the basis eigenstates in the tight binding approximation.

We further simplify the above Hamiltonian [Eq. 1.1] by considering a constant onsite periodic potential and neglecting it. Thus, the Hamiltonian becomes,

$$H = t\sum_{j=1}^{L}(\hat{c}_{j+1}^{\dagger}\hat{c}_j + \text{h.c.}). \tag{1.2}$$

Now, using the Fourier transformation,

$$\hat{c}_j^{\dagger} = \frac{1}{L}\sum_k \hat{c}_k^{\dagger} e^{-ikja} \tag{1.3}$$

where k and a are the quasi-momenta and the lattice constant, respectively. The lattice constant is taken to be unity ($a = 1$). Here, the summation is taken over all the values of k within the first Brillouin zone (BZ) $[-\pi, \pi]$. Substituting Eq. [1.3] in Eq. 1.2, we get,

$$H_k = \sum_k E(k)\hat{c}_k^{\dagger}\hat{c}_k \tag{1.4}$$

where the dispersion relation is given by,

$$E(k) = -2t\cos(k). \tag{1.5}$$

In general, depending on the landscapes of the onsite potential, the properties of the material change significantly.

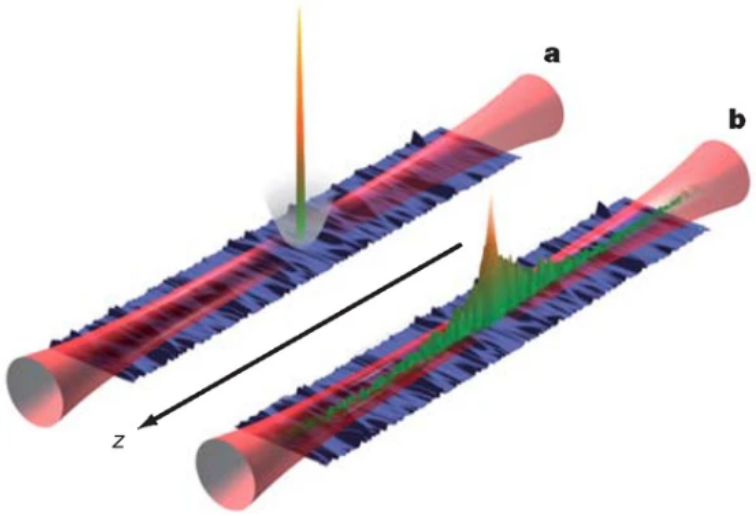

Figure 1.2: The initial state of the BEC is shown in (a). AL localization of the BEC is observed in (b). This figure is taken from Ref. [1].

1.2 Anderson localization

It was well established that, in presence of a periodic potential, the single-particle eigenstates are extended in nature. Thus, the effects of disorder, which can be introduced in the system through external agencies or present inherently, act as a perturbation. Hence, it was expected that the nature of the eigenstates would still remain extended in presence of finite disorder. However, in 1958, P. W. Anderson discovered that, in a non-interacting system beyond a critical disorder strength, all the single-particle eigenstates become completely localized irrespective of the tunneling energy of the electrons. Thus, ceasing the motion of each electron within a small region results in an insulating phase. This phenomenon is known as Anderson localization (AL) [10]. In a non-interacting system, this is the key mechanism behind the metal-insulator transition. The localization phenomenon results from the interference effect of multiple reflections of single-particle eigenstates by the scatters, which are randomly arranged. Un-

like the periodic potential, the phases and the amplitudes of the reflected waves are quite different in a disordered medium. As a result, the waves would interfere destructively and decay exponentially in position space as,

$$\psi(x) \sim e^{-|x-x_0|/\xi} \tag{1.6}$$

where ξ denotes the localization length and x_0 is the point from which the decay of the envelope starts for $|x - x_0| >> 1$.

As a practical example, AL in matter waves was first observed by Billy et al. in 2008 [1]. This experiment deals with the Bose-Einstein condensation (BEC) in a 1D waveguide in presence of controlled disorder. In particular, the disorder is created via an optical speckle field. To begin with, BEC is confined in an opto-magnetic hybrid trap. This trap combines a longitudinal magnetic trap and a horizontal (along the z-axis) optical waveguide, which leads to transverse confinement. Further, by turning off the longitudinal confinement at $t = 0$, it is observed that BEC tends to spread out over the waveguide along the z-direction. In the later case, by adding optical disorder to the above discussed system and further turning off the longitudinal confinement, it is illustrated that the spreading of the BEC arises; however, it stops rapidly in contrast to the previous case (See Fig. 1.2 (b)). In addition to the matter wave, the localization effect in the disordered background can be observed in a plethora of classical and quantum systems, such as in light waves [81, 82], ultrasound waves [83, 84], microwave [85], quantum waves [86, 87], optical lattices [88, 89, 90, 91], and photonic lattices [92].

The AL phenomenon in a tight binding non-interacting model can be stud-

ied by the Hamiltonian, which is given by,

$$H = -t \sum_{j=1}^{L} (c_{j+1}^{\dagger} c_j + h.c.) + \sum_{j=1}^{L} \epsilon_j c_j^{\dagger} c_j \tag{1.7}$$

where t is the hopping strength between nearest-neighbor sites. $c_j^{\dagger}$ (c_j) is the creation (annihilation) operator of an electron at the site j. The onsite energy at each lattice is uniformly distributed. The random energies (ϵ_j) are assumed to be taken from an energy range $[-W/2 : +W/2]$, where W is the random potential strength. It is observed that all the single-particle eigenstates are localized corresponding to $W > 0$, while they are extended for $W = 0$ in one dimension. Thus, the system suffers a complete localization in presence of an infinitesimal disorder. The same is true for two-dimensions (2D) as well, which disallows any possibility of a transition from conducting to insulating states. However, there is a metal-insulator phase transition observed in higher dimensions.

1.2.1 Scaling theory of localization

In 1979, Abrahams, Anderson, Licciardello, and Ramakrishnan (known as the 'gang of four') introduced the scaling theory of localization [11]. This theory demonstrates the dimensional dependency of the localization transition using a single parameter scaling.

In order to understand the theory of localization, we chose a measure of the effect of disorder, which is conductance. While it has a finite value corresponding to the metallic phase, it vanishes for the insulating phase. More specifically, Thouless introduced the formula for the dimensionless conductance, which is given by, [93]

$$g = G\left(\frac{h}{e^2}\right). \tag{1.8}$$

Here, $g(L)$ does not depend on the microscopic details of the material. However, it has a dependency on the system size L. The main idea of the scaling theory suggests that the conductance of a d-dimensional block with volume $(BL)^d$ (B is an integer) is only dependent on the conductance of B^d number of blocks corresponding to the volume L^d. In other words, the conductance can be written as,

$$g(BL) = f[g(L), B] \tag{1.9}$$

which suggests a re-scaling of $g(L)$ into $g(BL)$ can be possible using the function $g(L)$ and the scaling factor B. Furthermore, Eq. [1.9] can be written in differential form as,

$$\beta(g) = \frac{d(lng(L))}{d(lnL)} \tag{1.10}$$

where the scaling function β is only depend on the conductances.

Now, we want to study the asymptotic behavior of the function $\beta(g)$ corre-

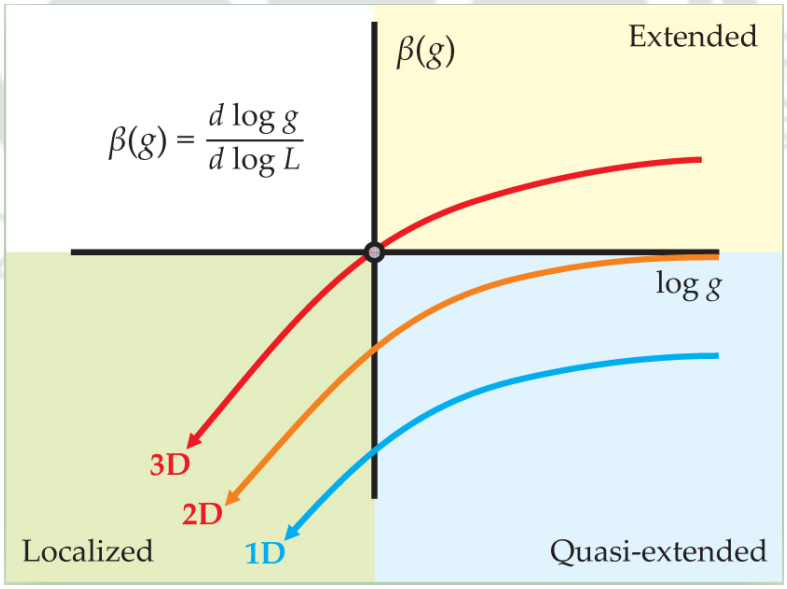

Figure 1.3: A Schematic plot is shown for the scaling function $\beta(g)$ as a function of $ln(g)$ corresponding to 1D, 2D, and 3D. This figure is taken from Ref. [2].

sponding to two limiting cases of weak and strong conductance $g(L)$. In the weakly disordered limit, the eigenstates are extended in nature; hence it follows Ohm's law. Thus the Ohmic conductance has the form,

$$g(L) = \sigma L^{d-2} \tag{1.11}$$

where σ is the dc conductivity of the material. Thus, the scaling function $\beta(g)$ has the form,

$$\beta(g) = (d-2). \tag{1.12}$$

On the other hand, the eigenstates are localized in nature for the strong disorder limit. As a result, the eigenstate falls off exponentially over space. Therefore, the conductance assumes the form,

$$g = g_0 e^{-L/\xi} \quad ; \quad \mathrm{L} >> \xi \tag{1.13}$$

and subsequently,

$$\beta \sim ln\left(\frac{g}{g_c}\right) \tag{1.14}$$

where the characteristic conductance is defined by g_c. The scaling theory predicts that $\beta(g)$ is monotonic and continuous. Thus a continuous interpolation between the extended and the localized regimes is possible, as shown in Fig [1.3]. Following the figure, positive values of β (i.e. $\beta > 0$) signify the conductance to increase with the system size L, which will eventually diverge in the thermodynamic limit. Thus, the asymptotic behavior of the scaling function will be,

$$\beta(g) = d - 2. \tag{1.15}$$

On the other hand, the negative values of β (i.e. $\beta < 0$) indicate the diminishing conductance with the system size L, which will vanish in the thermodynamic limit. Thus, the function will be of the form,

$$\beta(g) = ln(g/g_0). \tag{1.16}$$

Now, for system dimension $d \leq 2$, it is observed from the graph that β is always negative. Hence, the system will show an insulating behavior for any finite amount of disorder. However, this is not the case for dimension $d > 2$. A crossover between the metallic and insulating regimes occurs at $\beta = 0$. The crossing point acts as the critical transition point of the metal-insulator transition.

1.3 Optical lattice

A brief introduction of the optical lattice is thought as necessary for demonstrating the phenomenon of AL and explaining properties of interacting cold atomic gases. In real materials, the effects of disorder and interactions are unavoidable. Considering all these effects in a theoretical model makes it a difficult problem, and at times impossible to incorporate all the effects. It is rather required to choose a model which concentrates on specific features of the system. On the other hand, this chosen simplified model may not be verified by experiments

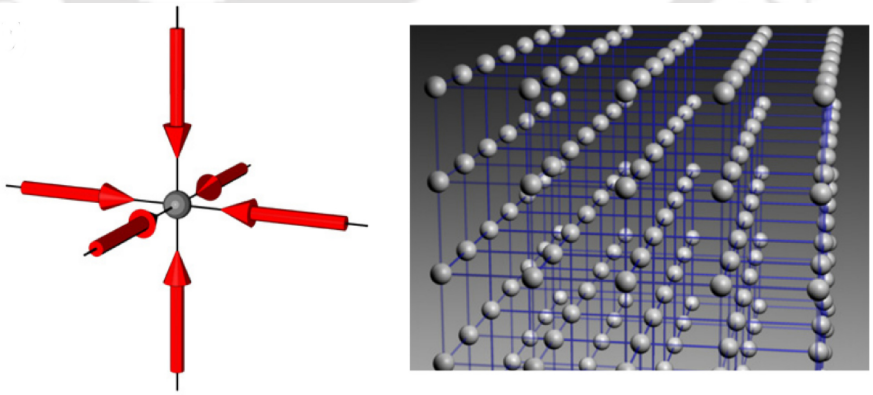

Figure 1.4: A 3D optical lattice can be generated using three orthogonal laser sources. The figure is taken from Ref. [3].

as it possible misses out many key ingredients. For example, realizing a phase transition in a many body system on a crystal lattice in a controlled and tractable manner may never be possible. In these circumstances, the optical lattice opens a new and versatile doorway by tuning the disorder and interaction by external means. As a result, the optical lattice provides a tool to validate many of these theoretical models experimentally.

Optical lattices can be generated by interfering two coherent counter-propagating laser lights. Consequently, an optical standing wave with a periodic pattern is generated. The period of the potential is $\lambda/2$, with λ being the wavelength of the laser light. Mathematically, the periodic potential can be represented as,

$$V(x) = V_0 \sin^2(kx) \tag{1.17}$$

where V_0 is the depth of the potential and k is the wave vector of the laser light. The nature of the potential, such as attractive or repulsive, depends on the intensity of the laser light along its propagating direction. In addition to that, the geometry and the depth of the lattice are tunable with an unprecedented procession. By adjusting the wavelength and the angles of the laser source, it is possible to create various geometries of the potential according to the requirement of the study. Also, the depth of the potential depends on the intensities of the laser light. By allowing more number of laser sources, different dimensional (1D, 2D, and 3D) potentials can be created (see Fig. 1.4). The optical lattice provides a range of potential geometries to trap the atoms. These trapped atoms loose almost all the kinetic energy and hence are at very low temperature. At this temperature, the quantum effect starts to dominate. In order to achieve such lower temperatures, a laser cooling technique is used. This method is developed by Chu, Cohen-Tannudji, and Phillips [94, 95, 96]. Several methods of

laser cooling exist owing to a significant technological development. Doppler cooling is the most popular one. Other methods are polarization gradient cooling [97], Anti-stokes cooling [98], Raman cooling [97], etc. We give a brief introduction of the Doppler cooling technique, and ignore the rest.

In the Doppler cooling method, the laser light frequency is kept at a lower value than the resonance frequency of the atom. As a result, the moving atoms along the direction of laser light absorb more photons due to the Doppler effect. Thus atoms will suffer a scattering of photons in the opposite direction of the laser. During the scattering process, an atom emits a photon and pushes an equal amount of the momentum in a random direction. This process occurs repeatedly, resulting in the lowering of the average speed of the atoms. Subsequently, the kinetic energy of the atom decreases, leading to cooling of the atom.

Ultracold atoms in optical lattices are used in experiments to study several interacting phenomena, such as, quantum phase transition, Bose-Einstein condensation, magnetism, and many more. More significantly, it acts as a quantum simulator [3].

1.3.1 QP potential in optical lattices

Although AL is observed in several systems, direct detection of the eigenstates in real experiments with materials makes it difficult to achieve. However, the controlled tuning of disorder and interaction in ultracold atoms loaded on optical lattices provides a great opportunity to verify this phenomenon of localization. AL is actually observed in the lab using optical potential via two different

methods. In one method, it is studied using the speckle potential [4], and in another one, the potential is quasiperiodic (QP) or incommensurate in nature [1]. The speckle potential is random in nature, which is not the focus of the thesis. Let us emphasize on the QP potential which can be produced by the superposition of two optical potentials, which is given by [Fig 1.5(a)],

$$V_{op} = \frac{V_s}{2}\cos(2kx) + \frac{V_d}{2}\cos(2k\beta x + \theta) \tag{1.18}$$

where the first term represents the primary potential which creates the underlying lattice, and the second term represents the secondary potential which acts as a perturbation. The two potentials are incommensurate that the ratio of their wavelength can not expressed as a rational fraction, namely, p/q (where p and q are coprime integers) with respect to each other, giving rise to an irrational β value. As a result, the effective potential breaks the translational symmetry of the primary lattice, and energy gets arranged quasiperiodically. A paradig-

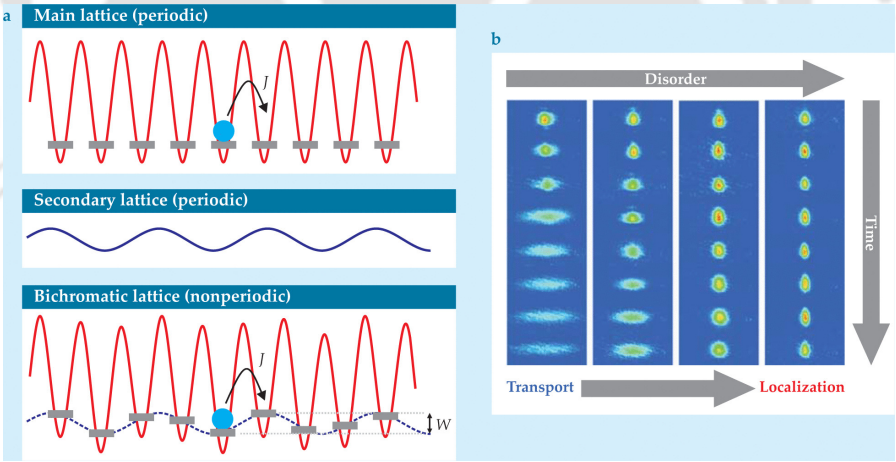

Figure 1.5: The creation of effective quasiperiodic potential using bichoramic optical lattice is shown in (a). The absorption images of BEC as a function of time is shown in (b). The strength of incommensuration of the columns (left to right) are taken as $\Delta/J = 0$, $\Delta/J = 1.8$, $\Delta/J = 4.2$, and $\Delta/J = 7$, respectively. The figure is taken from Ref. [4].

matic, tight-binding model that describes the QP potential in a one-dimensional system is studied by Aubry and André in 1980 [99].

In 2008, Roati et al. first observed the AL transition in matter waves using quasiperiodic potential. One of the key results of them is shown in Fig [1.5(b)]. Their experiment captures the spatial distribution of the atoms using absorption images as time progresses. It is observed that the eigenstates are expanded ballistically and span the entire lattice, signifying the emergence of an extended state when there is no disorder present ($\Delta/t = 0$). In another extreme limit, for large values of Δ, for example, $\Delta/t = 7$, the diffusion vanishes, hence indicating localization of the eigenstates. Therefore, a transition from extended to localized states similar to the AL is observed using QP potential even in one dimension. However, as discussed earlier, AL in presence of random potential necessitates a critical dimension, namely, 3D.

1.4 Aubry-André model

It is observed that, the localization transition is also possible in deterministic potential in contrast to the uncorrelated (Anderson) type. A one-dimensional system in presence of quasiperiodic (QP) potential or in an incommensurate lattice is one of the most studied platforms. The QP potential belongs to an intermediate regime of the periodic and a random potential.

A paradigmatic model to study quantum transport in presence of QP potential is the Aubry-André (AA) model. This tight-binding model shows a one-dimensional periodic lattice in presence of onsite quasiperiodic modulation. We observe the quasiperiodic modulation in Fig. 1.6 as a function of the site index

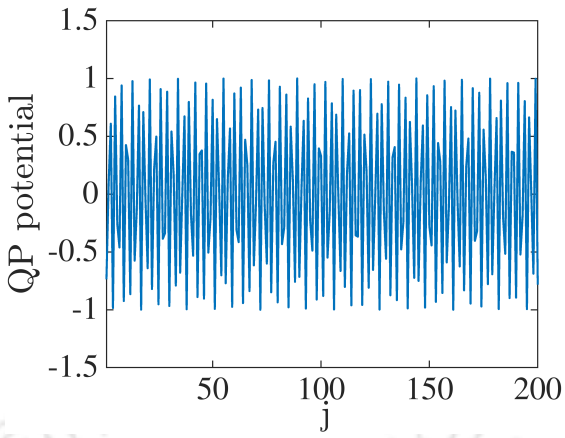

Figure 1.6: A one-dimensional quasiperiodic potential is shown as a function of the site index. In order to plot this potential we choose $\beta = (\sqrt{5}-1)/2$. We observe the distribution of the onsite energies, which are within the the width [-1 : 1].

j. The Hamiltonian of the model is given by,

$$H = t\sum_{j=1}^{L}(c_{j+1}^{\dagger}c_j + h.c.) + \lambda\sum_{j=1}^{L}\cos(2\pi\beta j + \theta)c_j^{\dagger}c_j \tag{1.19}$$

where the nearest-neighbor hopping strength is represented by t. λ is the onsite potential strength. θ denotes the phase of the potential. The periodicity of the potential is given by $1/\beta$. The important aspect of the AA model is the incommensurability of the periodic potential with respect to the underlying lattice (which is periodic) and is guaranteed by choice of an irrational number of β. In numerical and experimental studies, it is generally considered to have a finite lattice with periodic boundary conditions. In this case, the periodic potential is no longer truly incommensurate, and carefulness has to be exercised when enhancing the system size so as to discuss the thermodynamic limit. Thus, the β value is chosen as an approximate value. It is known that any irrational value can be written as a continued fraction expansion. The approximate value of β is taken as a ratio of subsequent Fibonacci numbers $\frac{F_{N-1}}{F_N}$, where F_{N-1} and F_N are the periods of the primary and the secondary lattice, respectively (see Eq. 1.18).

The ratio of two Fibonacci numbers converges to the "golden ratio" in the thermodynamic limit. So here we choose $\beta = (\sqrt{5}-1)/2$ as an inverse of the ' golden mean ' which is also known as a Diophantine number [100].

The model shows that corresponding to the particular values of β, the Hamiltonian undergoes a phase transition from all single-particle extended eigenstates for $\lambda < 2t$ to a scenario comprising of completely localized eigenstates for $\lambda > 2t$, yielding a critical transition point at $\lambda = 2t$. The reason behind the sharp transition is the self-dual property of the Hamiltonian, which we shall discuss later.

1.4.1 Self-dual property

The localization transition in the AA model occurs due to the self-dual symmetry which is unique and inherent to the model. Subsequently, the Hamiltonian exhibits a sharp localization transition at the specific value of λ ($\lambda = 2t$), resulting in no mobility edge. A mobility edge is the critical energy that separates the extended states from the localized ones. If the self-dual symmetry is broken, the localization transition becomes energy-dependent, and the system is said to have a mobility edge. Thus, this is one of the most interesting properties of the AA model. We demonstrate it below.

In the real-space formalism, the Hamiltonian [Eq. 1.19] can be written as,

$$H = t\sum_{n}(|n\rangle\langle n+1| + |n+1\rangle\langle n|) + \lambda\sum_{n}\cos(2\pi\beta n)\,|n\rangle\langle n| \tag{1.20}$$

where the phase term is ignored. Now, introducing a basis transformation,

$$|k\rangle = \frac{1}{\sqrt{L}}\sum_{n} e^{i2\pi k\beta n}\,|n\rangle \tag{1.21}$$

where these momentum states are eigenstates of the momentum operator corresponding to the eigenvalue

$$k' = kF_{l-1} \mathrm{mod} F_l. \tag{1.22}$$

The inverse transformation is obtained by multiplying both side by $e^{-i2\pi k\beta m}$ and sum over k, which is given by,

$$\begin{aligned} \sum_k e^{-i2\pi k\beta m}|k\rangle &= \frac{1}{\sqrt{L}} \sum_{k,n} e^{i2\pi k\beta(n-m)}|n\rangle \\ &= \sqrt{L}|n\rangle. \end{aligned} \tag{1.23}$$

Hence,

$$|n\rangle = \frac{1}{\sqrt{L}} \sum_k e^{-i2\pi k\beta n}\ |k\rangle. \tag{1.24}$$

Similarly, we can also find,

$$|k+1\rangle = \frac{1}{\sqrt{L}} \sum_n e^{i2\pi(k+1)\beta n}|n\rangle. \tag{1.25}$$

Subsequently, the inverse transformation is obtained by multiplying both sides by, $e^{-i2\pi k\beta m}$. Thus we get,

$$\begin{aligned} \sum_k e^{-i2\pi\beta km}|k+1\rangle &= \frac{1}{\sqrt{L}} \sum_k \sum_n e^{i2\pi k\beta n} e^{-i2\pi k\beta m} e^{i2\pi\beta n}|n\rangle \\ &= \frac{1}{\sqrt{L}} \sum_k \sum_n e^{i2\pi k\beta(n-m)} e^{i2\pi\beta n}|n\rangle \\ &= \frac{1}{\sqrt{L}} \sum_n \delta_{nm} e^{i2\pi\beta n}|n\rangle. \end{aligned} \tag{1.26}$$

Hence,

$$|n\rangle = \sum_k e^{-i2\pi k\beta m} e^{-i2\pi\beta n}|k+1\rangle \tag{1.27}$$

By substituting Eq. 1.24 and Eq. 1.27 into the real-space eigenvalue equation Eq. 1.20, we get,

$$
\begin{aligned}
H &= t\sum_n(|n\rangle\langle n+1| + |n+1\rangle\langle n|) + \lambda\sum_n \cos(2\pi\beta n)|n\rangle\langle n| \\
&= \sum_n[\frac{t}{L}\sum_k\sum_{k'} e^{-i2\pi\beta kn}e^{i2\pi\beta k'(n+1)}|k\rangle\langle k'| + \frac{t}{L}\sum_k\sum_{k'} e^{-i2\pi\beta k(n+1)}e^{i2\pi\beta k'n}|k\rangle\langle k'| \\
&+ \lambda\sum_n \cos(2\pi\beta n)\frac{t}{L}\sum_k\sum_{k'} e^{-i2\pi\beta kn}e^{i2\pi\beta k'n}|k\rangle\langle k'|] \\
&= \frac{t}{L}\sum_n\sum_k\sum_{k'}(e^{-i2\pi k\beta n}e^{i2\pi k'\beta(n+1)} + e^{-i2\pi k\beta(n+1)}e^{i2\pi k'\beta n})|k\rangle\langle k'| \\
&+ \frac{\lambda}{2L}\sum_n\sum_k\sum_{k'}(e^{i2\pi\beta n} + e^{-i2\pi\beta n})e^{-i2\pi k\beta n}e^{i2\pi\beta k'n}\,|k\rangle\langle k'| \\
&= \frac{t}{L}(\sum_n\sum_k\sum_{k'} e^{i2\pi\beta n(k'-k)}e^{i2\pi\beta k'}|k\rangle\langle k'| + \sum_n\sum_k\sum_{k'} e^{i2\pi\beta n(k'-k)}e^{-i2\pi\beta k}|k\rangle\langle k'|) \\
&+ \frac{\lambda}{2L}(\sum_n\sum_k\sum_{k'} e^{i2\pi\beta n(k'+1-k)}|k\rangle\langle k'| + \sum_n\sum_k\sum_{k'} e^{i2\pi\beta n(k'-1-k)}|k\rangle\langle k'|) \\
&= 2t\sum_k \cos(2\pi\beta k)|k\rangle\langle k| + \frac{\lambda}{2}\sum_k(|k\rangle\langle k+1| + |k+1\rangle\langle k|).
\end{aligned}
\tag{1.28}
$$

Therefore, the eigenvalue equation in momentum space is given by,

$$
H = \frac{\lambda}{2}\sum_k\Big(|k\rangle\langle k+1| + |k+1\rangle\langle k|\Big) + 2t\sum_k \cos(2\pi\beta k)|k\rangle\langle k|). \tag{1.29}
$$

By comparing Eq. 1.20 and Eq. 1.29, two critical observations can be made. The real-space eigenvalue equation appears the same as the the momentum space eigenvalue equation at $\lambda = 2t$ under the Fourier transformation. In addition to that, the hopping strength (t) and the QP potential strength (λ) get exchanged. In order to satisfy these two conditions, all the single-particle eigenstates should be extended and localized in nature corresponding to $\lambda < 2t$ and $\lambda > 2t$, respectively. As a result, $\lambda = 2t$ acts as the critical transition point. Hence, a QP potential induces a localization transition in one dimension at this critical point.

In order to have a precise understanding of the self-duality in the AA model, we can follow the probability distribution of the eigenstate corresponding to the real and momentum space Hamiltonians Eq. 1.20 and Eq. 1.29 as a function of

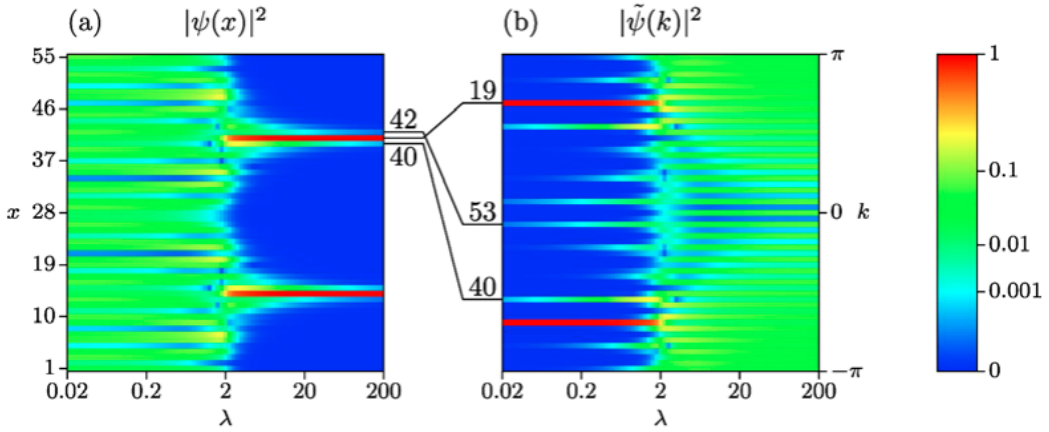

Figure 1.7: Here we show the probability distribution of the eigenstates as a function of potential strength (λ) corresponding to (a) the real space and (b) the momentum space. This Figure is originally taken form the Ref. [5].

the QP potential strength λ in Fig 1.7. The real-space probability distribution plot in Fig 1.7(a) shows a broadening while approaching the critical transition point $\lambda = 2t$ from above, that is from a higher value of λ. As a result, the system hosts a longer range coupling. On the other hand, we observe that no broadening occurs in the momentum space density profile in Fig 1.7(b). It is observed that, instead the coupling occurs between distant momentum values. Therefore, the momentum values rearranged themselves due to the basis transformation. As a result, the localization transition occurs at the self-dual point $\lambda = 2t$.

The self-dual point also coincides with the Harper model. Before introducing the AA model to study the localization phenomena, this Harper model was introduced in a 2D, and the energy spectrum was later studied by Hofstadter.

1.4.2 Harper model

Consider an electron is moving in a 2D square lattice in the $x-y$ plane in the presence of the perpendicular uniform magnetic field, $\vec{B} = B\hat{z}$. In the Landau gauge, we can use for the vector potential $\vec{A} = (0, Bx, 0)$ where $\vec{B} = \bar{\nabla} \times \vec{A}$. Using Peierls substitutions where hopping term in the presence of magnetic field are given by,

$$t_{nm} = t_{nm}^{(0)} exp\left[\frac{ie}{\hbar c}\int \vec{A}.d\vec{l}\right] \tag{1.30}$$

where $d\vec{l}$ represents the link between the sites n and m on the lattice.

A tight-binding model for the single-particle eigenstates $\psi(x, y)$ is given by,

$$t_x[\psi(x+a, y) + \psi(x-a, y)] + t_y[\psi(x+a, y)exp(\frac{ie}{\hbar c}Bxa) + \\ +\psi(x-a, y)exp(\frac{-ie}{\hbar c}Bxa)] = E\psi(x, y) \tag{1.31}$$

where $t_x(t_y)$ is the tunneling strength between neighboring sites along the $x(y)$ axis. The lattice constant is given by a. Here, the y-coordinate is cyclic, so the solution can be taken as,

$$\psi(x, y) = u(x)exp(ik_y y). \tag{1.32}$$

Further simplifying by discretizing the eigenstate via $u_n = u(na)$ where n is an integer. Thus, we have

$$t_x(u_{n+1} + u_{n-1}) + 2t_y \cos(2\pi\beta n + k_y a)u_n = Eu_n \tag{1.33}$$

where $\beta = \frac{Ba^2e}{hc}$, which defines the number of magnetic flux quanta per plaquette in the lattice.

Now, it is noticeable that, the above equation can be mapped into the AA model Hamiltonian [Eq. 1.19] by substituting for $t = t_x$, $\lambda = 2t_y$, and $\phi = k_y a$.

Thus the problem of an electron traversing in a QP potential is analogous to that of an electron traversing a square lattice with a perpendicular magnetic field. Hofstadter later studied the Harper model. In this study, it is observed that the eigenspectrum takes on a self-similar structure when plotted over a range of different rational values of β. The structure is known as the "Hofstadter Butterfly". Using this self-similar structure, Hofstadter was able to show that the spectrum for irrational β formed the so-called Cantor set.

1.4.3 Characterization of localization properties

In order to discern the localization properties of the AA model, we calculate the eigenvalues and the eigenstates of the Hamiltonian Eq. [1.19]. Since the localization phenomenon can be captured via both of these quantities, we will thus employ them one by one. Using the eigenstates of the Hamiltonian, we compute two quantities, which are inverse participation ratio (IPR) and normalized participation ratio (NPR). These are found to be the most used tools in the literature to study the localization properties of the system.

The Schrödinger equation corresponding to the onsite QP potentian will be given by,

$$H|\psi\rangle = E|\psi\rangle \tag{1.34}$$

where E is the energy eigenvalues of the Hamiltonian. Also, any single-particle eigenstate can be expanded in the site basis, which is given by,

$$|\psi\rangle = \sum_j \phi_j |j\rangle \tag{1.35}$$

where ϕ_j is the amplitudes of the eigenvector at the site j. Now, for the given

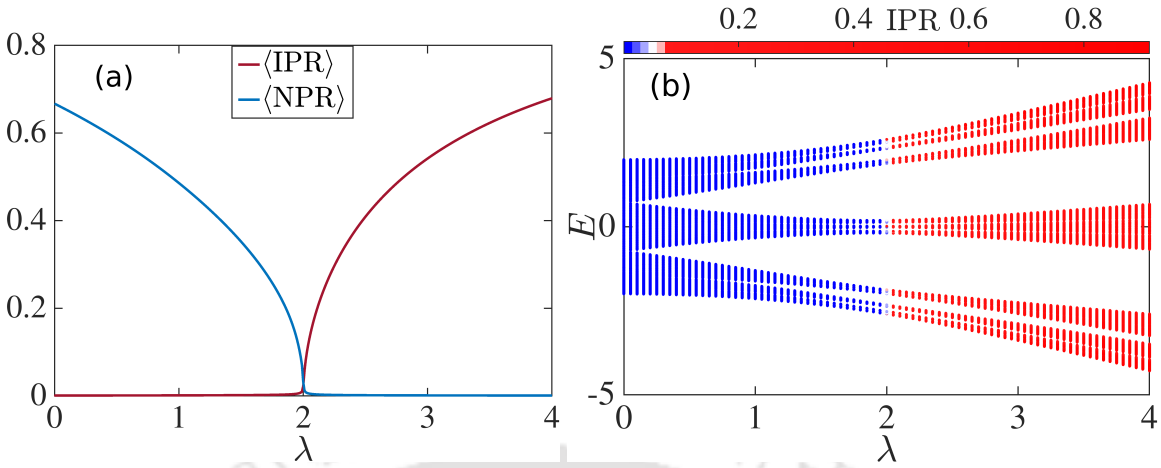

Figure 1.8: (a) The average value of the IPR and the NPR are plotted as a function of λ. (b) The energy spectrum of the AA Hamiltonian is shown as a function of λ. The color bar represents the IPR value associated with the energy eigenvalues.

state $|\psi\rangle$, we define the IPR in the real space as [101, 102],

$$\text{IPR} = \sum_j |\phi_j|^4. \tag{1.36}$$

IPR measures the inverse number of sites occupied by the given states. It is possible to understand the properties of this parameter by considering two limiting

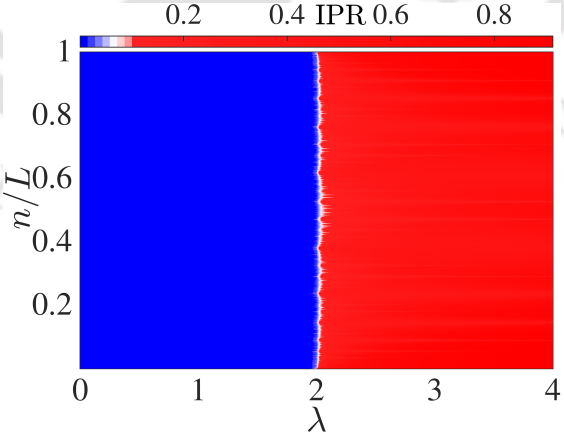

Figure 1.9: The IPR values are shown corresponding to all the eigenstates as a function of λ.

cases. For the uniformly distributed eigenstate over L sites, we have

$$\phi_j = \frac{1}{\sqrt{L}} \tag{1.37}$$

then the IPR parameter will behave as,

$$\text{IPR} = \sum_j \left(\frac{1}{\sqrt{L}}\right)^4 = \frac{1}{L}. \tag{1.38}$$

For the localized eigenstate on a single site, we have,

$$\phi_j = \delta_{i,j} \tag{1.39}$$

hence, the IPR parameter will have a finite value that is $O(1)$.

Further, the properties of the normalized participation ratio (NPR) show an exact opposite behavior compared to the parameter IPR, which is given by,

$$\text{NPR} = \sum_{j=1}^{L} \left[L|\phi_j|^4\right]^{-1}. \tag{1.40}$$

Thus, for a given extended state,

$$\text{NPR} \sim O(1) \tag{1.41}$$

and corresponding to the localized state,

$$\text{NPR} \sim 1/L. \tag{1.42}$$

Moreover, the average value of the IPR and NPR over entire single-particle eigenstates are given by,

$$\begin{aligned} \langle \text{IPR} \rangle &= \sum_{n=1}^{L} \text{IPR}_n \\ \langle \text{NPR} \rangle &= \sum_{n=1}^{L} \text{NPR}_n \end{aligned} \tag{1.43}$$

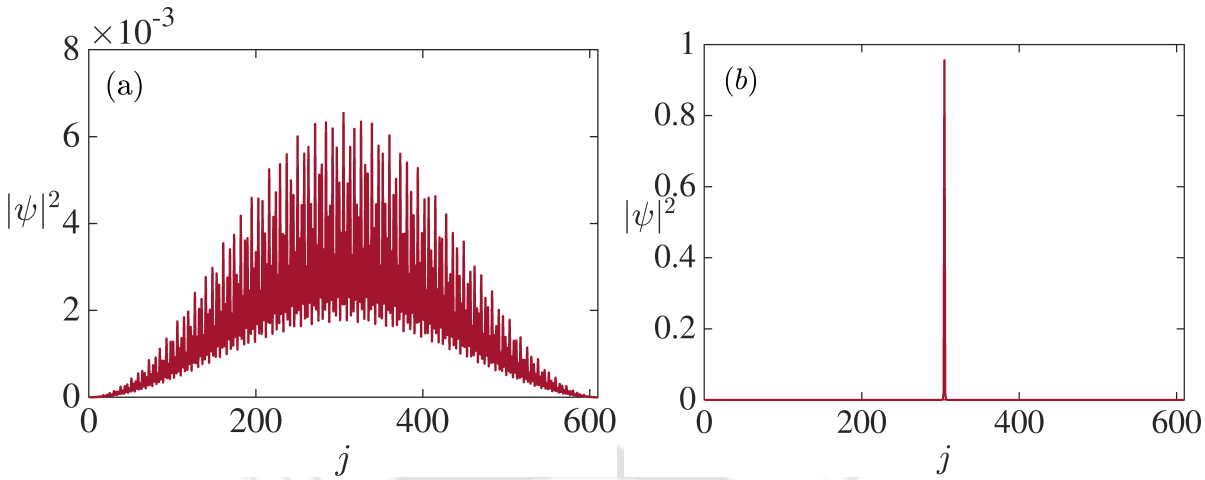

Figure 1.10: Here, we plot the probability distribution of the eigenstate as a function of site index (j) corresponding to (a) $\lambda = 1.0$ (b) $\lambda = 4.0$. In this calculation, the system size is taken as $L = 610$.

where n represents the eigenstate index.

Numerically, we plot the average IPR and the NPR as a function of the QP potential strength λ in Fig. 1.8 (a). The plot shows a sharp transition at the critical transition point $\lambda_c = 2t$ eliminating the possibility of a mobility edges which it should be. Next, the localization transition is followed by observing the energy spectrum. Thus, we show the energy spectrum as a function of λ in Fig. 1.8 (b). The color bar in the plot shows the IPR values of the respective eigenstates. In order to clear our observation, we plot the IPR value corresponding to all the eigenstates as a function of λ in Fig. 1.9. A phase transition is observed from an extended to a localized phase, resulting in a critical nature at the transition point. The eigenstates at the transition point differ from those of the extended and the localized phases; instead, they appear multifractal. Further, we show the probability distribution of the eigenstates as a function of the site index (j) corresponding to the extended and localized nature in Fig. 1.10 (a) and (b) , respectively. For the first case, we chose the lowest energy state at $\lambda = 1.0$ while

for the later case, $\lambda = 4.0$. It is illustrated that, the extended state is uniformly distributed throughout the lattice, yielding a finite probability at each lattice site. On the other hand, the localized state is comprised of some of the lattice sites. We shall discuss the nature of the critical state in the formalism chapter.

1.5 Experiment to theoretical model

The Hamiltonian of the system in presence of optical potential Eq. (1.18) is given by,

$$H = -\frac{\hbar^2}{2m}\frac{d^2}{dx^2} + V_{op}\sin^2(k_{op}x) + V_{os}\sin^2(k_{os}x + \phi) \tag{1.44}$$

where V_{op} and V_{os} are the strengths of primary and secondary potentials, respectively. In addition, k_{op} and k_{os} represent the wave vectors corresponding to primary and secondary potentials. It is convenient to rewritten the Hamiltonian in terms of recoil energy of the primary lattice, which is

$$E_p^r = \frac{\hbar^2 k_{op}^2}{2m} \tag{1.45}$$

with m being the mass of the electron. In addition to that, we choose a dimensionless variable, namely,

$$y = k_{op}x. \tag{1.46}$$

Thus we get,

$$\begin{aligned}\frac{H}{E_p^r} &= -\frac{d^2}{dy^2} + \frac{V_{op}}{E_p^r}\sin^2(y) + \frac{V_{os}}{E_p^r}\sin^2(\beta y + \phi) \\ &= \hat{H_{op}} + \frac{V_{os}}{E_p^r}\sin^2(\beta y + \phi)\end{aligned} \tag{1.47}$$

where $\beta = \frac{k_{os}}{k_{op}} = \frac{\lambda_2}{\lambda_1}$. The secondary potential does not alter the position of the lattice sites. This only acts as a perturbation and shifts the energies with an amplitude $\frac{V_{os}}{E_p^r}$.

The experimental set up can be mapped onto the theoretical AA model. In order to do that, the eigenstate ψ is expanded in the Wannier basis of the lower band of primary lattice, which can be written as,

$$|\psi\rangle = \sum_j \hat{c}_j |w_j\rangle. \tag{1.48}$$

The Wannier state are labeled by $|w_j\rangle$, which are maximally localized around the site index j. Thus the AA Hamiltonian which is expended in the Wannier state basis can be written as,

$$\begin{aligned} H &= \langle\psi|H|\psi\rangle \\ &= \sum_{i,j} \hat{c}_i^\dagger \hat{c}_j \langle w_i|H|w_j\rangle. \end{aligned} \tag{1.49}$$

In the tight-binding limit, assuming the following approximation leads to

$$\langle w_i|H|w_j\rangle \sim \epsilon_0 \delta_{i,j} + t\delta_{i,j+1} + \delta_{i,j} \frac{V_{os}}{E_p^r} \int |w_i(y)|^2 \sin^2(\beta y + \phi) dy \tag{1.50}$$

with

$$\epsilon_o = \int w_i(y) \hat{H}_{op} w_i(y) \tag{1.51}$$

and

$$t = \int w_{i+1}(y) \hat{H}_{op} w_i(y) dy. \tag{1.52}$$

The hopping integral t is sufficient to approximated by the overlap of nearest-neighbor Wannier states with the Hamiltonian $\hat{H}_{op}$ and the energy ϵ_0 is the on-site contribution of $\hat{H}_{op}$. We can drop the constant energy by choosing suitable energy offset. The last term Eq. 1.50 represents the corrections to the nearest-neighbor hopping t due to the secondary lattice.

Using the relation,

$$\sin^2(\beta y + \phi) = \frac{[1 - \cos(2\beta y + 2\phi)]}{2} \tag{1.53}$$

we shall have,

$$\begin{aligned}
&\int |w_i(y)|^2 \sin^2(\beta y + \phi) dy \\
&= \cos(2\pi\beta i + 2\phi) \int |w_i(y)|^2 \cos(2\beta y) dy \\
&= \cos(2\pi\beta i + \theta) \int |w_i(y)|^2 \cos(2\beta y) dy
\end{aligned} \tag{1.54}$$

where $\theta = 2\phi$. By simplifying, we get,

$$\lambda = \frac{V_{os}}{2E_p^r} \int |w_i(y)|^2 \cos(2\beta y) dy. \tag{1.55}$$

Hence,

$$\langle w_i|H|w_j\rangle \sim \epsilon_0 \delta_{i,j} + t\delta_{i,j+1} + \delta_{i,j}\lambda \cos(2\pi\beta i + \theta). \tag{1.56}$$

Therefore, the Hamiltonian of the bicromatic potential can be written as,

$$H = t \sum_j (\hat{c}_{j+1}^\dagger \hat{c}_j + h.c.) + \lambda \sum_j \cos(2\pi\beta i + \theta) \hat{c}_j^\dagger \hat{c}_j \tag{1.57}$$

which is also the form of the Hamiltonian of the AA model [Eq. 1.19].

1.6 Outline of the thesis

In **chapter 1**, we start our discussion by solving a 1D tight-binding model, which acts as a theoretical model to describe the motion of an electron in non-interacting systems. Under the tight-binding approximation, we further study the electronic transport properties in presence of disorder, resulting in the Anderson localization (AL) phenomenon. Having the theoretical and experimental overview of the AL phenomenon, it is concluded that the metal-insulator transition is only achievable for a system dimension greater than two. On the other hand, it is established that AL transition occurs in one-dimensional systems in

the presence of a deterministic potential, namely quasiperiodic (QP) or incommensurate potential. Further, the possibility of creating this potential using optical lattices makes it a suitable platform to explore the physics regarding the AL in experiments. Consequently, we discuss the experimental achievements of this potential and the interesting properties of its theoretical model, namely, the Aubry-André model.

In **Chapter 2**, we mainly focus on the formalism and models, which will be used in the later chapters of the thesis. In the first part of the chapter, we discuss formalism to analyse the properties of eigenstates and eigenspectra corresponding to a Hamiltonian. As a consequence, we explore the multifractal properties in the study of eigenstates. In addition to that, we discuss the theory of the Hausdorff dimension and level spacing as a tool to study the eigenspectra. Further, before explaining the critical state analysis for the localization study in presence of QP potential, we elaborately discuss the theory of phase transition and its critical phenomena. In the later part, we present a detailed explanation of topology in condensed matter systems. This section comprises of topological band theory, symmetries, and classification of topological phases. We also present an extensive discussion on the one-dimensional Su - Schrieffer - Heeger (SSH) and Kitaev chain models as examples of topological insulators and superconductors since these are the representative models in the subsequent chapters. Finally, we also discuss an interacting model, which is the Bose-Hubbard model. We briefly introduce this model, and subsequently, explore different phases and their properties which are emerged in this model.

In **chapter 3**, we study a one-dimensional chain in presence of onsite QP potential, described by the pure AA model. In addition to that, we also study

the generalized version of the model by incorporating off-diagonal QP modulation. Using the critical state analysis, we study the critical behavior in the localization transition, which occurs in the pure AA model. Further, we study the off-diagonal AA model. We observe a phase transition from an extended phase to a multifractal phase as a function of the off-diagonal potential strength in the absence of any onsite potential. We established our results via fractal dimension and finite-size scaling analysis.

In **chapter 4**, we study a one-dimensional dimerized chain, also known as the Su - Schrieffer - Heeger (SSH) model, in the presence of QP potential at the two sublattices in a unit cell. We analyze the localization properties of this model using the participation ratio, eigenenergies, density of states, and finite-size scaling analysis. The result of our analysis shows a reentrant localization transition. In particular, it undergoes a localization transition at a specific critical potential strength through a mobility edge. Further, an intermediate (critical) phase associated with the mobility edge appears in larger disorders. Finally, at strong potential strength, the second localization transition sets in.

In **chapter 5**, as the next step, we want to comprehend the critical behavior corresponding to the reentrant localization transitions in detail in our subsequent research work. Consequently, we observe two localization transitions through two critical phases. As a result, the system hosts four critical points as a function of the potential strength. The critical behavior of these phase transitions is explored using the multifractal and critical state analysis. In addition to that, we explore the critical properties of eigenenergies by calculating the Hausdorff dimension.

In **chapter 6**, we study a one-dimensional dimerized Kitaev chain in pres-

ence of onsite QP potential. The dimerized Kitaev chain is comprised of a one-dimensional SSH chain and a Kitaev chain. Thus the system possesses topological properties. Thus, in this chapter, we study the localization and the topological properties of the system separately. In the context of the localization study, we explore a series of phase transitions using participation ratio, fractal dimension, and level spacing. On the other hand, by computing the real-space winding number and the number of Majorana zero modes, we analyze the topological properties of this model. Moreover, a finite-size scaling analysis is shown for both cases.

In **chapter 7**, we study a two-dimensional interacting system in presence of QP potential. Aided by a site-decoupled mean-field approximation, percolation scenario, and finite-size scaling analysis, we explore the phase diagram of this system and study the critical behavior associated with the phase transitions. In the analysis, we observe a quasiperiodically induced mixed (QM) phase in addition to the BG phase in presence of the QP potential.

In **chapter 8**, we conclude with the main results obtained in various chapters.

CHAPTER 2

FORMALISM AND MODELS

Since one of our primary focus of this thesis lies on the critical state analysis and the spectral properties of the model Hamiltonians, in the first section of this thesis, we outline the details of this approach. In this context, a single-particle state can be written in terms of the superposition of eigenstate $|m\rangle$ corresponding to the eigenspectrum E_m of H as,

$$|\psi\rangle = \sum_{i=1}^{L} \phi_i^{(m)} |m\rangle \tag{2.1}$$

where ϕ_i^m denotes the amplitude corresponding to a lattice site i and m denotes an eigenstate index. Overall understanding of physical properties of the system can be achieved just by studying these eigenstates ($|\psi\rangle$) and eigenspectra (E_m). Here, we study the scaling behavior of the eigenstates via multifractal analysis, and that of the eigenspectra by analyzing the Hausdorff dimension [60] and level-spacing [22]. We shall describe all of these in the following. In addition to that, we shall elaborately illustrate a general discussion on the phase transition and critical phenomena associated with it. Following this general idea, we discuss a critical state analysis method to explore the critical behavior of the localization transition in presence of QP potential, thereby computing the phase transition point, critical exponents, and scaling functions [103].

On the later section, we shall discuss the topological properties in condensed matter system, as topology plays an important role in chapter 4, 5 and 6 in our thesis. The topological phases of matter offer remarkable and intriguing phenomena that aid in understanding of the crucial symmetries and physical properties of systems [65, 104, 105]. In particular, we are interested in two categories, which are the topological insulator (TI) [106] and topological superconductor

(TSc) [107]. As the simplest example of the TI, the Su- Schrieffer-Hegger (SSH) [108] model is well established. This model comprises two sublattices in a unit cell with staggered hopping strength within and between the unit cells. The topological properties of the model are characterized by zero-energy modes, which are localized at the boundary. In addition to this, the topological superconductors (TSCs) have received immense attention due to their relevance to the field of topological quantum computation [107]. The Majorana zero modes (MZMs), thought to be found in the TSCs, are considered flawless candidates for them to be used as qubits [109, 110]. The unique property of the MZMs to have a great deal of importance for their non-local nature with complete localization occurring at the boundaries of the chain, and hence robust to any local perturbations [111, 112]. A prototype theoretical model to study the TSCs and the properties of the MZMs is the Kitaev chain model [113]. The model describes a one-dimensional tight-binding spinless fermions in the presence of p-wave superconducting correlations. The MZMs are quasiparticle excitations that obey non-Abelian statistics. Recently, several theoretical models have been proposed to find the signature of MZMs [114, 115, 116, 117]. From the experimental perspective, the most studied and accepted proposal is the semiconductor-superconductor hybrid systems [118, 119, 120, 121, 122]. Other than that, there are some other realistic models developed as well [123, 124, 125]. Subsequently, we present the formalism for the real and momentum space winding number calculations. Specifically, we have used the real-space formalism.

Finally in the last section, we add interaction and thereby discussing Bose-Hubbard model and its phase properties.

2.1 Eigenstate properties

The localization transition in the AA model signifies a transition from an extended state to a localized state. However, at the transition point, the behavior of the eigenstate is neither extended nor localized. As a result, the properties of the eigenstate at the transition point become significantly interesting and non-trivial. It shows that the eigenstate is self-similar, hence fractal in nature. Later, it was realized that the critical eigenstates are not only fractal, instead, they are multifractal. A spectrum possessing family of fractals implies a multifractal behavior of the eigenstates of the system.

2.1.1 Multifractals analysis

In this thesis, the scaling nature of the eigenstates is done by studying the multifractal analysis. The classification of the eigenstates, such as the localized, extended or the critical states can be performed via computing the inverse participation ratio (IPR). The IPR of the m-th eigenstate is defined as [24, 22, 50],

$$\mathrm{IPR}^{(m)} = \sum_{i=1}^{L} |\phi_i^{(m)}|^4. \tag{2.2}$$

Since an IPR value is not sufficient to describe the underlying physics of an eigenstate associated with the critical nature, the higher moment of the IPR is more fundamental in that case. Therefore, a multifractal nature of the eigenstates can be identified through the generalized IPR and its scaling exponent τ_q using the relation,

$$\mathrm{IPR}_q^{(m)} = \sum_{i=1}^{L} |\phi_i^{(m)}|^{2q} \rightarrow L^{-\tau_q}, \tag{2.3}$$

where τ_q is also known as the mass exponent and q is a real number. The mass exponent vanishes for the localized states, whereas it varies linearly with the system dimension d for the delocalized state as $\tau_q = d(q-1)$. Furthermore, the scaling exponents of the multifractal states can be characterized by a non-linear relation where d (see above) is no longer an integer and further acquire a q dependence, which can be written as,

$$\tau_q = D_q(q-1), \tag{2.4}$$

where D_q denotes the fractal dimension of the eigenstates. Therefore, an extended and a localized state have respectively 1 and 0 as their fractal dimensions while an intermediate value of D_q (between 1 and 0) denotes the fractal nature of the eigenstates. Further, by setting the value for $q = 2$, the fractal dimension (D_2) can be defined as [22, 60],

$$D_2 = -\lim_{L\to\infty} \frac{log(\text{IPR})}{log(L)}. \tag{2.5}$$

Where L denotes the length of the system.

2.2 Eigenspectrum analysis

Generally, the fractal dimension carries the information about the eigenstates of the system. Also, we can complement our analysis via the eigenspectrum corresponding to the Hamiltonian.

2.2.1 Level-spacing

In this thesis, we shall be calculating another quantity, namely, the energy level spacing, which uses the eigenenergies. In this calculation, we use the energies corresponding to the entire spectrum. Suppose, the energy eigenvalues are arranged in ascending order, that is, $E_1 < E_2 < .. < E_L$ where L is the system length. Now, corresponding to a given energy E_n with $n = 1, 2, \ldots L$, the even-odd and the odd-even spacings can be calculated via [22],

$$s_n^{e-o} = E_{2n} - E_{2n-1} \tag{2.6}$$

$$s_n^{o-e} = E_{2n+1} - E_{2n}. \tag{2.7}$$

Due to the presence of doubly degenerate eigenvalues in the extended phase, the value of s_n^{e-o} will be zero, while s_n^{o-e} will not be zero. Thus a gap will occur in the spectrum. On the other hand, there will be no gap in the localized phase. However, a distribution of fluctuations for s_n^{e-o} and s_n^{o-e} will be present corresponding to the critical phase.

2.2.2 Hausdorff dimension

The understanding of the details of the energy spectrum at the critical regime can be computed by the Hausdorff dimension of the system. A direct box-counting method is applied for this analysis. Considering the total number of boxes required to be N_l for a given box length l such that N_l spans over the entire energy spectrum. N_l shows a power-law behaviour with l as [60],

$$N_l \propto l^{-D_H}, \tag{2.8}$$

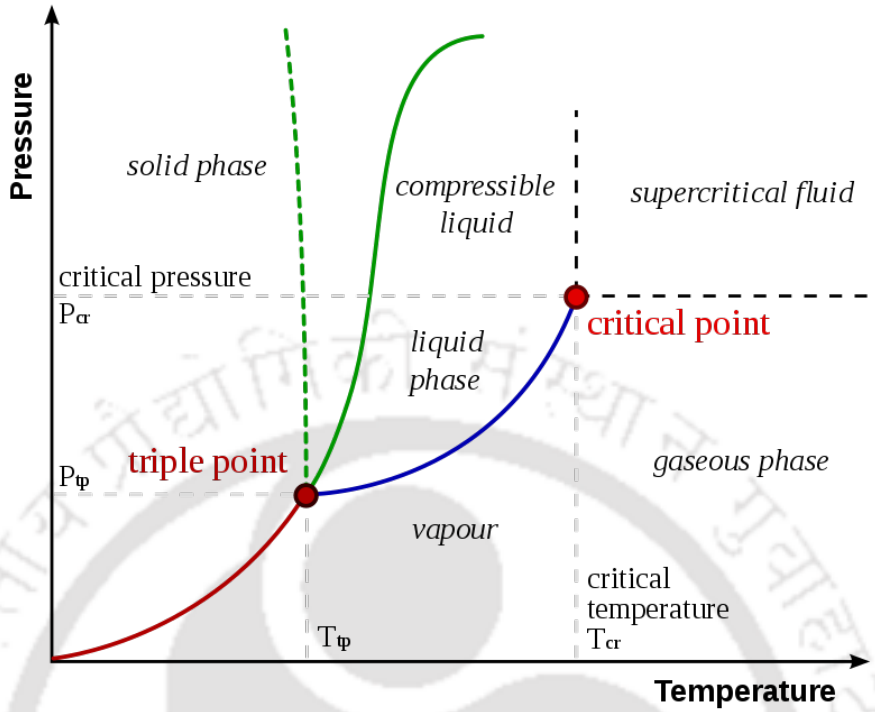

Figure 2.1: A schematic typical phase diagram is shown for fluid in the $T - P$ plane. The figure is taken from https://en.wikipedia.org/wiki/Phase_transition#/media/File:Phase-diag2.svg.

where, D_H denotes the Hausdorff dimension corresponding to the energy spectrum. The non-trivial fractal nature of the spectrum is characterized by the fractional value of D_H, that is, $0 < D_H < 1$.

2.3 Phase transition

To begin with, we wish to comprehend the fundamental concept of phase transition. In order to do that, let us consider a well-known example of phase diagram in fluid systems. It is illustrated in Fig. 2.1 that there are several phases of matter, such as solid, liquid, and gaseous phases, corresponding to the values of the

system parameters namely, pressure (P) and temperature (T). Moreover, each of the coordinates of the boundaries between the distinct phases in the $T - P$ plane are referred to as the equilibrium states. Hence, two or more phases can coexist in each of these equilibrium states. For example, all the three phases coexist at the triple point. Generally, a phase transition can be understood by the singularity in free energy under an external tuning parameter which can either be pressure, temperature, density, magnetic field, etc. Further, for the sake of characterizing different phases, a quantity can be assigned, known as the order parameter vanishing of which (or its divergence) indicates a phase transition. It can be calculated using free energy. A phase transition is strictly defined in the thermodynamic limit, that is, $n \to \infty$ (the number of particles) and $v \to \infty$ (volume of the system), however, $\frac{n}{v}$ (density) remains constant. It is usually categorized into two classes: first and second-order phase transition.

A first-order phase transition can be easily understood via the above-discussed phase diagram Fig. 2.1. Consider a piece of ice at a temperature that is kept at a lower value of temperature than the melting point (0^oC). Now, by heating it up, the temperature slowly increase. Further, we may observe that, upon approaching its melting point, the temperature remains constant despite adding more heat until the complete meltdown of ice occurs. Consequently, a coexistence of solid and liquid phases is found at the phase transition point, and latent heat becomes an essential parameter for a phase transition. In conclusion, phases coexisted at the first-order phase transition, and the latent heat is involved. Moreover, the order parameter and the first derivative of the free energy show discontinuity at the temperature at which the phase transition occurs.

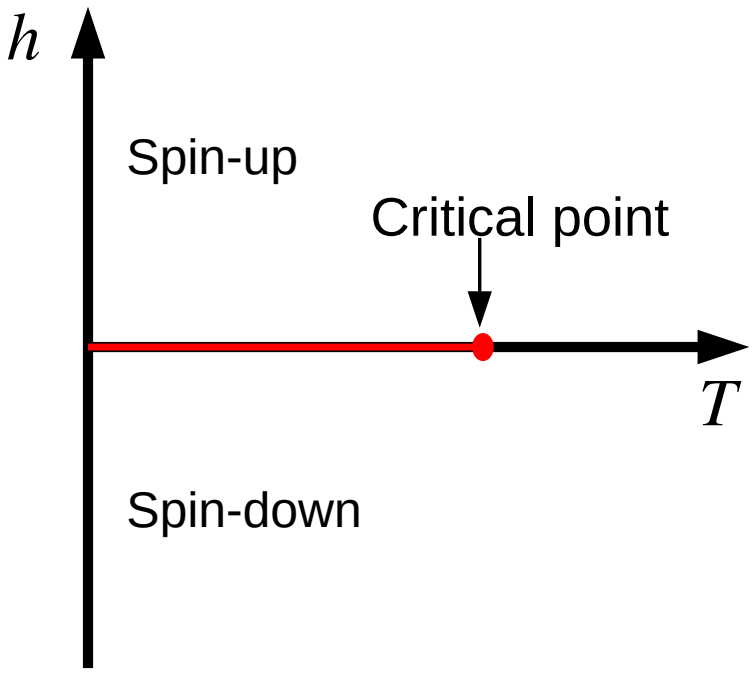

Figure 2.2: A schematic phase diagram is shown for iron in the $h-T$ plane. The red line indicates a first-order phase boundary, while the phase transition is continuous at the critical point.

In order to understand the second-order (also known as the continuous phase transition), we shall focus on the liquid-gas phase boundary in Fig. 2.1. It is noticeable that the phase boundary line ends at a critical point without crossing it, resulting in a continuous phase transition from a liquid to a gas. As a consequence, no coexistence of phases is observed at the transition point, implying no essential distinction between liquid and gaseous phases. Hence, the phenomenon does not involve latent heat. In the phase diagram, all other phase transitions are of first-order categories, while only the transition through the critical point behaves as a second-order transition.

Another popular example of phase transition is observed in magnetic systems and is shown in Fig. 2.2. It is depicted that there are two phases comprising of spin-up and spin-down, separating through a phase boundary at $h = 0$,

where h denotes the magnetic field. At the boundary, two phases appear to coexist, indicating it to be a first-order phase transition. However, magnetization, which acts as an order parameter for the scenario, drops to zero at a finite temperature. Finally, the phase boundary terminates at the critical point resulting in a phase transition from a ferromagnet to a paramagnet. The temperature at which it happens is known as the Curie temperature. Consequently, the order parameter vanishes, and the fundamental distinction between the phases disappears, which distinguishes it from the first-order transition.

2.3.1 Critical phenomena

We are interested in understanding the important features around the critical point. The collective behavior of the critical point which is associated with the continuous phase transition known as critical phenomena. In general, the behavior around the critical point is fascinating and complicated at the same time, thereby offering a huge motivation to study various intricate properties of phase transitions. In 1869, T. Andrews discovered a remarkable manifestation of criticality in an experiment using CO_2 [126]. It was observed that the size of droplets of CO_2 becomes similar to the wavelength of the incident light upon approaching the critical point from above. Consequently, scattered lights are visible with bare eyes. This phenomenon is known as the critical opalescence, implying strong fluctuations occurring at large length scales. The characteristic distance over which fluctuations occur is known as the correlation length denoted by (ξ). It depicts that, while approaching the critical point, it diverges, which is expressed via,

$$\xi \sim |\varepsilon|^{-\nu} \tag{2.9}$$

where $\varepsilon = (T - T_c)/T_c$ denotes the reduced temperature, which refers to a dimensionless measure of distance from the critical point. ν represents the correlation length exponent. Moreover, the fluctuations are slow in nature around criticality, known as critical slowing down. Thus, it is also observed that the correlation time (ξ_τ) also diverges, which is given by,

$$\xi_\tau \sim \xi^z \sim \xi^{-\nu z} \tag{2.10}$$

where z denotes the dynamical critical exponent. In the example of the magnetic phase transition, it is observed that the above-discussed power law singularities of the correlation length (ξ) and time (ξ_τ) scales lead to the power law singularities of other observables, such as, magnetization (m), susceptibility (χ), specific heat (C), which are, respectively written as,

$$m \sim (-\varepsilon)^\beta \tag{2.11}$$

$$\chi \sim (\varepsilon)^{-\gamma} \tag{2.12}$$

$$C \sim (\varepsilon)^{-\alpha}. \tag{2.13}$$

Therefore, a critical point can be characterized by the critical exponents, namely, α, β, γ, ν, and z corresponding to the expressions discussed above in Eq. [2.9-2.13].

2.3.2 Scaling theory

Next, we wish to understand the phenomenological description of critical points via scaling theory. This theory provides a powerful mechanism for analyzing numerical and experimental data. It was first proposed by Widom as a scaling hypothesis [127]. The scaling hypothesis states that the singular part

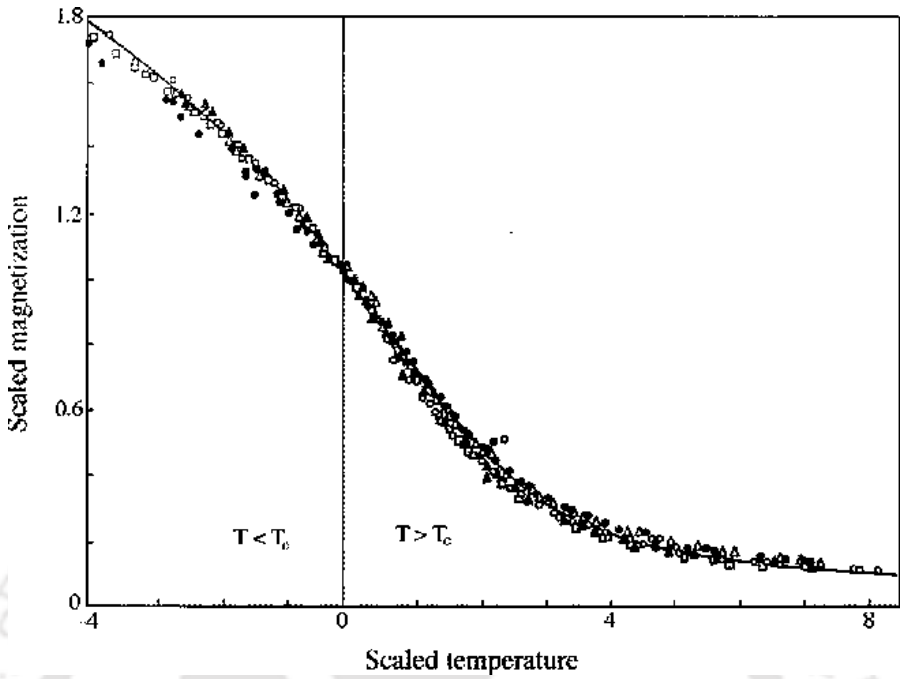

Figure 2.3: Experimental data corresponding to different magnetic materials are shown in scaled magnetization-temperature plane. This plot is taken from Ref. [6].

of the free energy is a generalized homogeneous function [6]. In general, the homogeneous function will satisfy,

$$f(x) = a^b f(ax). \tag{2.14}$$

For example, we consider a function $f(x) = cx^d$, then

$$f(ax) = a^d f(x) \tag{2.15}$$

hence

$$f(x) = a^{-d} f(ax).$$

Therefore, a scale transformation of distance has been done so that the function at a 'distance' x is the same as that at another distance ax when multiplying with a^{-d}. Hence, a generalized homogeneous function will satisfy the following

relation, given by,

$$f(x, y) = af(a^b x, a^c y). \tag{2.16}$$

Similarly, the scaling hypothesis at the critical point can be expressed as,

$$G_s(\Lambda^a H, \Lambda^b \varepsilon) = \Lambda G_s(H, \varepsilon) \tag{2.17}$$

where $G_s(H, \varepsilon)$ is the singular part of the Gibbs potential per spin, $G(H, \varepsilon)$. a and b are the scaling powers of magnetic filed (H) and temperature (T), respectively.

Using these two exponents a and b, it is possible to find expressions among the critical exponents, known as the scaling laws. For example, we already know the critical exponents corresponding to C, m^2 and χ are α, 2β, and γ, respectively. These critical exponents are related via a scaling law, given by

$$\alpha + 2\beta + \gamma = 2. \tag{2.18}$$

In general, there are several relations possible between the critical exponents.

The scaling law is one of the important characteristics of the scaling approach. Another important feature is the data collapse. We shall explore this concept using an example. We consider an equation state of magnetization at the critical point. Hence we take derivative of the Eq. 2.17, with respect to magnetic field (H), given by,

$$m(\Lambda^a H, \Lambda^b \varepsilon) = \Lambda^{1-a} m(H, \varepsilon). \tag{2.19}$$

Since Eq. 2.19 is true for any positive value of Λ, thus we shall make a choice of $\Lambda = H^{-1/a}$. By substituting this in the Eq. 2.19, we get,

$$m_H = m(1, \varepsilon_H) = \mathcal{F}(\varepsilon_H) \tag{2.20}$$

where the magnetization and temperature are scaled via

$$m_H = \frac{m}{H^{1-a}/a} \tag{2.21}$$

and

$$\varepsilon_H = \frac{\varepsilon}{H^{b/a}}. \tag{2.22}$$

The function $\mathcal{F}(x) = m(1, x)$ is known as the scaling function. Fig. 2.3 shows a plot of the scaled magnetization as a function of scaled temperature for different values of H. It is illustrated that, according to the scaling hypothesis, all the curves corresponding to various values of H will collapse onto a single universal curve. The result implies a universal phenomenon satisfied by all of these different systems at the critical point. Therefore, we can conclude that, at the critical point, the system forgets its microscopic details except for the space dimension and the symmetries possessed by the system. Further, depending on the critical exponents and scaling functions, various continuous phase transitions are classified into distinct universality classes. In Fig. 2.3, we observe all the data curves to have the same critical exponents and scaling function, indicating an identical universality class for all of them.

Until now, our study was based on phase transition at non-zero temperatures, where the transition happens due to thermal fluctuations. In addition, there is another kind of phase transition possible at the limit of lower temperature value. At this temperature, the phase transition occurs due to the variation of non-thermal parameters such as, magnetic field, pressure, chemical composition, etc. To make it more concrete, we shall study the phase transitions induced by the variation of the parameters of the Hamiltonian that describes the system. This is known as the quantum phase transition [128]. In condensed matter physics, there are several quantum phase transitions observed, which are metal-insulator transition, superfluid-insulator transition, ferromagnetic to anti-ferromagnetic transition, and many more. We shall be dealing with only quantum phase transition, and ignore thermal effects. However, the above dis-

cussion on the critical properties etc. are equally valid as those we have seen for the 'classical' phase transitions. We shall only discuss the features that are important for our subsequent discussion.

2.3.3 Critical state analysis

In general, localization in a disordered system can also be characterized by using the normalized participation ratio, (NPR) which for the m-th eigenstate is defined as, [following Eq. 2.1]

$$\mathrm{NPR}^{(m)} = \left[L \sum_{i=1}^{L} |\phi_i^{(m)}|^4 \right]^{-1} = \frac{\mathrm{PR}^{(m)}}{L} \tag{2.23}$$

where L is the system size and PR is the participation ratio (PR=1/IPR). In the extended regime, PR grows linearly with system size L, while it vanishes in the localized regime in the thermodynamic limit. For further analysis, we consider the average value of NPR. Following the averaged NPR values; we can identify the order parameter for the localization transition as, [103]

$$\sigma = \sqrt{\frac{\mathrm{PR}}{L}} = \sqrt{\mathrm{NPR}}. \tag{2.24}$$

In the vicinity of the phase transition, the observables show power law behaviour with their critical exponents behaving as,

$$\sigma \sim (-\varepsilon)^{\beta} \;\; ; \qquad \mathrm{PR} \sim \varepsilon^{-\gamma} \;\; ; \qquad \xi \sim |\varepsilon|^{-\nu}. \tag{2.25}$$

Here, $\varepsilon = (\lambda - \lambda_c)/\lambda_c$ is the reduced disorder potential strength with λ_c being the critical disorder strength for the localization transitions and ξ is the correlation (or localization) length. β, γ and ν are the order parameter exponent, participation ratio exponent and the correlation length exponent respectively.

Following Ref. [103] the order parameter σ associated to two different system sizes yields a function $R[L, L']$, which is given by

$$R\,[L, L'] = \frac{log(\sigma_L^2/\sigma_{L'}^2)}{log(L/L')} + 1. \tag{2.26}$$

The critical point for the transition λ_c and the critical exponent ratio γ/ν are determined using the above two system size-variable function $R[L, L']$. The variation of $R[L, L']$ with the strength of the potential in the vicinity of the critical point for several pairs of system of sizes L and L' intersect each other at a common fixed point. The critical potential strength λ_c and the exponent ratio γ/ν are determined from the abscissa and the ordinate of the common crossing point respectively.

In the vicinity of the critical point, a finite-size scaling form of the order parameter σ for finite system is defined by,

$$\sigma = L^{-\beta/\nu} F(\varepsilon L^{1/\nu}) \tag{2.27}$$

where F is a scaling function . Similarly, a finite-size scaling form of PR for a finite sized system is defined by,

$$\text{PR} = L^{\gamma/\nu} G(\varepsilon L^{1/\nu}) \tag{2.28}$$

where G is another scaling function. Using Eq.(2.24), Eq.(2.28) can be re-written as,

$$\sigma^2 L = L^{\gamma/\nu} G(\varepsilon L^{1/\nu}) \tag{2.29}$$

which can be further expressed as,

$$\sigma^2 = L^{\gamma/\nu - 1} G(\varepsilon L^{1/\nu}) \tag{2.30}$$

Hence, a plot of $\sigma^2 L^{1-\gamma/\nu}$ versus $\varepsilon L^{1/\nu}$ for different system sizes L should fall onto a single curve denoted by $G(\varepsilon L^{1/\nu})$ if the critical potential strength λ_c and the

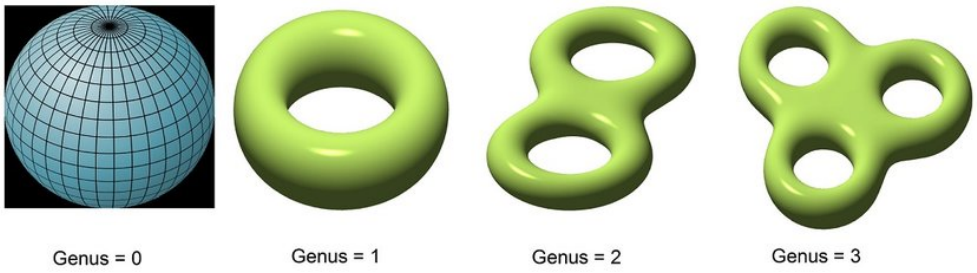

Figure 2.4: The figure shows distinct values of the genus (g) corresponding to different geometrical shapes. The value of the genus is specified by the number of holes. The figure is taken from Ref. [7].

critical exponents are correctly determined. In chapter 3 [Ref. 3] and 5 [Ref. 5], we will utilize the above prescription to study the critical properties for the localization transitions.

2.4 Topology

In our thesis, we shall encounter yet another important concept, namely, topology. Topology is a mathematical concept that categorizes various geometrical objects into classes. Two objects belong to the same topological class if the deformation of their properties (such as shape) is continuous. The deformation rule is restricted to bending or stretching without tearing it apart, or puncturing a hole. This can be easily understood with a simple example in the following. It is illustrated that a sphere can be smoothly deformed into a disk. On the other hand, it can not be deformed into a doughnut. Thus a quantity is assigned to distinguish a sphere and a doughnut based on the number of holes, known as the genus denoted by (g). Therefore, two objects with different g values cannot be deformed into one another, resulting in topologically distinct phases.

Subsequently, same value of g corresponding to two objects implies them to be topologically equivalent.

Introducing Guess-Bonnet theorem, which states that integral of a Gaussian curvature K over the surface of an object S, resulting in an integer topological invariant, which is given by,

$$\chi = \frac{1}{2\pi} \int_S K dA \tag{2.31}$$

where $\chi = 2 - 2g$. In Fig 2.4, we depict various values of g corresponding to distinct geometrical objects, which belong to different topological classes.

Including this concept in the solid state band theory is one of the most exciting advancements in condensed matter physics. Here, the Hamiltonians of the system play the role of geometrical objects. Subsequently, topology studies the properties of the Hamiltonians, which possess an energy gap under smooth deformations. In the current scenario, smooth deformations suggest transformations of the Hamiltonians via changing any of the associated parameter, provided the energy spectrum remains gapped. Thus, two Hamiltonians when continuously transformed into one another without closing the energy gap, they are topologically equivalent, and, hence belong to the same topological class. The classification of topological classes is determined based on certain symmetries, such as, time-reversal symmetry (TRS), particle-hole symmetry (PHS), and chiral symmetry (CS). We will discuss them in the following.

2.4.1 Symmetries

In quantum mechanics, symmetry operations signify a transformation that conserves all the probabilities of possible measurements made in the system. Sup-

pose $|\psi\rangle$ and $|\phi\rangle$ are two states in the Hilbert space. Thus the preservation of probabilities of measurements under symmetry transformation suggests that,

$$|\langle\hat{O}\psi|\hat{O}\phi\rangle| = |\langle\psi|\phi\rangle| \tag{2.32}$$

where $\hat{O}$ denotes a symmetry operator. Now, suppose the symmetry operator is linear and unitary ($\hat{O_1}^{\dagger}\hat{O}_1 = I$), which satisfy,

$$\hat{O}_1(a|\psi\rangle + b|\phi\rangle) = a\hat{O}_1|\psi\rangle + b\hat{O}_1|\psi\rangle \tag{2.33}$$

and

$$\langle\hat{O}_1\psi|\hat{O}_1\phi\rangle = \langle\psi|\hat{O}_1^{\dagger}\hat{O}_1|\phi\rangle = \langle\psi|\phi\rangle \tag{2.34}$$

where a and b are complex coefficients. On the other hand, if the symmetry is anti-unitary, which satisfies,

$$\hat{O}_2(a|\psi\rangle + b|\phi\rangle) = a^*\hat{O}_2|\psi\rangle + b^*\hat{O}_2|\psi\rangle \tag{2.35}$$

and

$$\langle\hat{O}_2\psi|\hat{O}_2\phi\rangle = \langle\psi|\hat{O}_2^{\dagger}\hat{O}_2|\phi\rangle^* = \langle\psi|\phi\rangle^*. \tag{2.36}$$

Any anti-unitary operator can be represented by a product of a unitary operator ($\hat{O}_1$) and a complex conjugate ($\mathcal{K}$), given by

$$\hat{O}_2 = \hat{O}_1\mathcal{K}. \tag{2.37}$$

Time-reversal symmetry

In the time-reversal symmetry operator, the time variable t transforms into $-t$, thereby reversing the direction of time or equivalently, we wish to examine whether the physical properties remain invariant if the velocity of the particle is reversed. It is denoted as τ. In order to understand the properties of τ, we need

to consider an infinitesimal time evolution of a given state $|\psi\rangle$. Subsequently, $\tau|\psi\rangle$ is the time-reversal partner of $|\psi\rangle$. Now, we consider two situations following the condition that $|\psi\rangle$ remains invariant under the time-reversal operation. In the first situation, we act the time-reversal operator (τ) on the state $|\psi\rangle$ and subsequently move forward in time by δt, which is given by,

$$\left(1 - i\frac{H}{\hbar}\delta t\right)\tau|\psi\rangle. \tag{2.38}$$

In another situation, the state $|\psi\rangle$ moves backward in time δt first and then acts the time reversal operator on it, which is given by,

$$\tau\left(1 + i\frac{H}{\hbar}\delta t\right)|\psi\rangle. \tag{2.39}$$

By equating Eq.2.38 and Eq.2.39, we have,

$$\left(1 - i\frac{H}{\hbar}\delta t\right)\tau|\psi\rangle = \tau\left(1 + i\frac{H}{\hbar}\delta t\right)|\psi\rangle \tag{2.40}$$

which yields,

$$-iH\tau = \tau iH. \tag{2.41}$$

Now, if we assume τ is a linear and unitary operator, then the relation in Eq.2.41 suggests,

$$H\tau = -\tau H. \tag{2.42}$$

This result implies that for our given state $|\psi\rangle$ and corresponding energy E, the time-reversal partner $\tau|\psi\rangle$ would be a state corresponding to an energy $-E$, which is absurd. Hence, it can be concluded that τ is an anti-linear and anti-unitary operator, which also suggests,

$$[\tau, H] = 0 \tag{2.43}$$

or

$$\tau H\tau^{-1} = H. \tag{2.44}$$

Particle-hole symmetry

In particle-hole symmetry (PHS) operation, the operator ($\mathcal{P}$) changes the sign of both energy and momentum. PHS operator is also an anti-unitary operator. As a consequence, the Hamiltonian is invariant under the PHS if it follows

$$\mathcal{P}H(\vec{k})\mathcal{P}^{-1} = -H(-\vec{k}). \tag{2.45}$$

Hence, it satisfies an anti-commutation relation. PHS signifies that, if the eigenstate and the eigenvalue of the Hamiltonian $H(\vec{k})$ at momentum $\vec{k}$, are given by ψ and E, respectively. Then we have,

$$H(\vec{k})\mathcal{P}\psi = -\mathcal{P}H(k)\mathcal{P} = -E\mathcal{P}\psi. \tag{2.46}$$

Hence, the result implies that $\mathcal{P}\psi$ is also an eigenstate of the Hamiltonian corresponding to opposite energy and momentum. In general, this symmetry is inherent in superconductors.

Chiral symmetry

In the chiral symmetry (CS) operation, the operator (C) changes the sign of energy only while the momentum remains unchanged. Unlike the time-reversal and particle-hole symmetry, C is a unitary operator. The Hamiltonian is invariant under CS if it follows,

$$CH(\vec{k})C^{-1} = -H(\vec{k}). \tag{2.47}$$

Hence, it satisfies an anti-commutation like PHS. Subsequently, it implies that, if ψ and E are the eigenstate and the eigenvalue of a Hamiltonian at momentum ($\vec{k}$), then $C\psi$ will also be an eigenstate of the Hamiltonian corresponding to an energy $-E$.

Classification of Topological insulator/Topological superconductors			
	CLASSES	SYMMETRY TRS PHS CS	DIMENSION D=1 D=2 D=3
Standard	A (unitary)	0 0 0	0 Z 0
	AI (orthogonal)	+1 0 0	0 0 0
	AII (symplectic)	-1 0 0	0 Z_2 Z_2
Chiral	AIII (chiral unitary)	0 0 +1	Z 0 Z
	BDI (chiral orthogonal)	+1 +1 +1	Z 0 0
	CII (chiral symplectic)	-1 -1 +1	Z 0 Z_2
BdG	D (p-wave)	0 +1 0	Z_2 Z 0
	C (d-wave)	0 -1 0	0 Z 0
	DIII (p-wave TRS SC)	-1 +1 +1	Z_2 Z_2 Z
	CI (d-wave TRS SC)	+1 -1 +1	0 0 Z

Table 2.1: Topological classification table is present here.

2.4.2 Classification of Topological Phases of Matter

Depending on the above-discussed fundamental discrete symmetries, various topological phases of Hamiltonians can be classified. Generally, there are ten combinations possible by these 3 symmetries where each of the combinations implies a symmetry class. This classification scheme is known as the tenfold way, which is shown in Table. 2.1. A symmetry class satisfied by a topological phase is termed as non-trivial. On the other hand, in the absence of any topological phase, the symmetry class is known as trivial. There are five non-trivial and five trivial symmetry classes exist in the Table. In addition, non-trivial symmetry classes are labeled by Z or Z_2, known as the topological invariant. A topological invariant characterizes distinct topological phases. For example, Z_2 invariant can have two values, such as, 1 and 0, corresponding to non-trivial and trivial phases, respectively. In addition, Z invariant can have any integer values which are corresponding to the non-trivial phase, while 0 denotes the trivial phase.

Finally, the classification of topological phases can be extended by including spatial symmetries, such as, translational or rotational symmetries. The extension of these symmetries results in a more involved table, which we skip discussing here.

In this thesis, we shall focus on the SSH and Kitaev chain models as examples of topological insulators and topological superconductors (in a restricted sense). Therefore, we shall discuss these two models in the following.

2.4.3 Topological band theory

Before moving forward, we start our discussion on topological classification of insulators. Following the band theory of solids, an insulator can be characterized by an energy gap between the ground state and excited states. It has been discussed that, the Hamiltonians corresponding to topologically equivalent insulators under a adiabatic transformation of parameters does not close the energy gap. While, topologically nonequivalent insulators suffer a phase transition through a gap closing point. Therefore, topological band theory aims to classify topologically distinct Hamiltonians. In addition, it characterizes the gapless states, which also contribute to the understanding of topological properties. Further, Berry phase is also a key concept in the topological band theory.

In crystalline materials, the electronic wave function is defined by the Bloch's theorem, which is given by,

$$\psi(\vec{r}) = e^{i\vec{k}.\vec{r}} u_{\vec{k}}(\vec{r}). \tag{2.48}$$

The amplitude function $u_{\vec{k}}(\vec{r})$ is periodic with the periodicity of the underlying lattice, that is,

$$u_{\vec{k}}(\vec{r} + \vec{R}) = u_{\vec{k}}(\vec{r}) \tag{2.49}$$

where $\vec{k}$ denotes the crystal momentum, which lies in the Brillouin zone (BZ) [129]. This BZ acts as a surface over which the integral of the Gaussian curvature is taken. To understand the analogue of the '(Gaussian) curvature' for a quantum system, we need to explore Berry phase and Berry connection [130].

Berry phase

Consider, a physical system corresponding to a Hamiltonian $H(\vec{S})$ where $\vec{S}$ is a parameter. The solutions of the time-independent Schrödinger equation is given by,

$$H(\vec{S})|n(\vec{S})\rangle = E_n(\vec{S})|n(\vec{S})\rangle \tag{2.50}$$

where states $|n(\vec{S})\rangle$ are normalized. Suppose, the initial state of the system is given by $|n(\vec{S}(t=0))\rangle$. Now, if we vary the parameter $\vec{S}$ slowly along a path C, how do the state varies? According to the *adiabatic theorem*, if we slowly vary the Hamiltonian, in that case, the system initially in the nth eigenstate, will reach at nth instantaneous eigenstate of $H(\vec{S}(t))$ at later time t. Thus, the system will start to evolve from $|n(S(0))\rangle$ to $|n(\vec{S}(t))\rangle$. At time t, the evolved state is given by,

$$|\psi(t)\rangle = e^{-i\theta(t)}|n(\vec{S}(t))\rangle. \tag{2.51}$$

Following Schrödinger equation, we can write

$$H(\vec{S}(t))\,|\psi(t)\rangle = i\hbar\frac{d}{dt}|\psi\rangle. \tag{2.52}$$

Thus,

$$E_n(\vec{S}(t))|n(S(t))\rangle = \hbar\left(\frac{d}{dt}\theta(t)\right)|n(\vec{S}(t))\rangle + i\hbar\frac{d}{dt}|n(\vec{S}(t))\rangle. \tag{2.53}$$

Now, multiplying both sides with $\langle n(\vec{S}(t))|$, we find,

$$E_n(\vec{S}(t)) - i\hbar\langle n(\vec{S}(t))|\frac{d}{dt}|n(\vec{S}(t))\rangle = \hbar\left(\frac{d}{dt}\theta(t)\right). \tag{2.54}$$

Subsequently,

$$\theta(t) = \frac{1}{\hbar}\int_0^t E_n(\vec{S}(t'))dt' - i\int_0^t \langle n(\vec{S}(t'))|\frac{d}{dt'}|n(\vec{S}(t'))\rangle dt' \tag{2.55}$$

where the first term represents the familiar dynamical phase corresponding to the time evolution of the Hamiltonian. The second term is known as the Berry

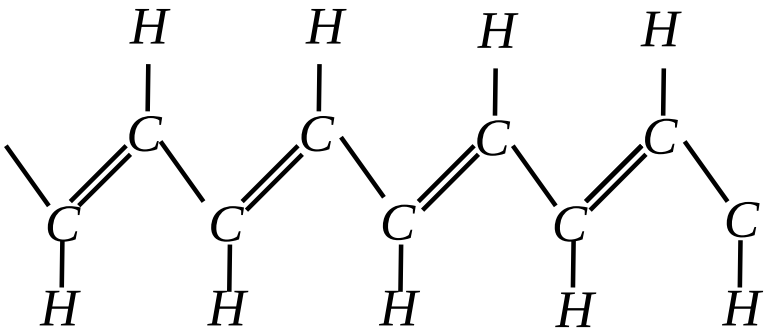

Figure 2.5: A schematic diagram of polyacetylene is shown here.

phase or the geometric phase. It is irreducible, unlike the dynamical phase. The Berry phase is given by,

$$\gamma_n = i \int_0^t \langle n(\vec{S}(t'))| \frac{d}{dt} |n(\vec{S}(t'))\rangle dt'. \tag{2.56}$$

Hence, the Berry connection or the Berry vector potential can be written as,

$$\gamma_n = i \int_0^t \langle n(\vec{S}(t'))| \nabla_{\vec{S}} |n(\vec{S}(t'))\rangle . \frac{d\vec{S}}{dt'} dt' \tag{2.57}$$

$$= i \int_{S_0}^{S_t} \langle n(\vec{S})| \nabla_{\vec{S}} |n(\vec{S}\rangle . d\vec{S} \tag{2.58}$$

$$= \int_{S_0}^{S_t} \vec{A}_n(\vec{S}) . d\vec{S} \tag{2.59}$$

where

$$\vec{A}_n(\vec{S}) = i\langle n(\vec{S})| \nabla_{\vec{S}} |n(\vec{S}\rangle \tag{2.60}$$

Further, the Berry curvature can be computed via,

$$\vec{\mathcal{F}} = \nabla \times \vec{A}. \tag{2.61}$$

We are interested in 1D quantum system for which the above discussion leaves loose ends which will be stitched later when we discuss the topological invariant, namely, the winding number.

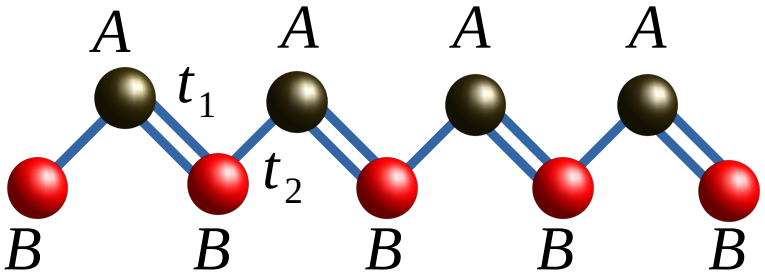

Figure 2.6: A schematic diagram of the SSH model comprising of two sublattices A and B in a unit cell. The intra-cell and the inter-cell hoping strengths are given by t_1 and t_2, respectively. Dimerization strength is denoted by $\delta = t_2/t_1$.

2.5 Topological insulator: SSH model

2.5.1 Model

The simplest example of a one-dimensional topological insulator is the Su-Shriffer-Hegger (SSH) model [108]. In 1979, this model was introduced to study an organic molecule, "polyacetylene". The molecule comprising of a chain of carbon atoms, which is shown in Fig. 2.5. It is observed that, due to Peierls's instability, consecutive carbon atoms are connected by strong and weak bonds. Thus, the tunneling strength alters between them, resulting in two carbon atoms in a unit cell. In the tight-binding limit, the Hamiltonian of the model, which is shown in Fig. 2.6, given by,

$$H = t_1 \sum_{n=1}^{N} \left(\hat{c}^{\dagger}_{n,B} \hat{c}_{n,A} + h.c. \right) + t_2 \sum_{n=1}^{N-1} \left(\hat{c}^{\dagger}_{n+1,A} \hat{c}_{n,B} + h.c. \right) \tag{2.62}$$

where the unit cell index is represented by n with $n = 1, 2, \ldots, N$. In each unit cell, there are two sublattices, which are labeled as A and B, respectively. Thus the length of the system is denoted as $L = 2N$. $\hat{c}^{\dagger}_{n,A}$ ($\hat{c}_{n,A}$) and $\hat{c}^{\dagger}_{n,B}$ ($\hat{c}_{n,B}$) are the creation (annihilation) operators of an electron at site (n, A) and (n, B),

respectively. The intra-cell hopping strength between two sublattices within a unit cell is given by t_1. Subsequently, the inter-cell hopping strength between two sublattices from consecutive unit cells is given by t_2. $\delta = t_2/t_1$ denotes the dimerization strength, which acts as a dimensionless variable to tune the bond strength of the model.

Our aim is to incorporate QP potential in this dimer model and subsequently, study the interplay of dimerization and potential. We shall report our observations in chapter 4 and 5.

2.5.2 Bulk properties

Under the periodic boundary condition, the Hamiltonian Eq. 2.62 can be diagonalized using the Fourier transformations are given by,

$$\hat{c}_{n,A} = \frac{1}{\sqrt{L}} \sum_k e^{ikn} \hat{c}_{k,A} \tag{2.63}$$

$$\hat{c}_{n,B} = \frac{1}{\sqrt{L}} \sum_k e^{ikn} \hat{c}_{k,B}. \tag{2.64}$$

where the lattice constant is taken to be unity. Note that k is a scalar here. Now, substituting Eq. 2.63 and Eq. 2.64 in the real-space Hamiltonian Eq. 2.62, we get,

$$H = \sum_k \hat{c}^\dagger_{\alpha_1,k} \mathcal{H}_{\alpha_1,\alpha_2}(k) \hat{c}_{\alpha_2,k} \tag{2.65}$$

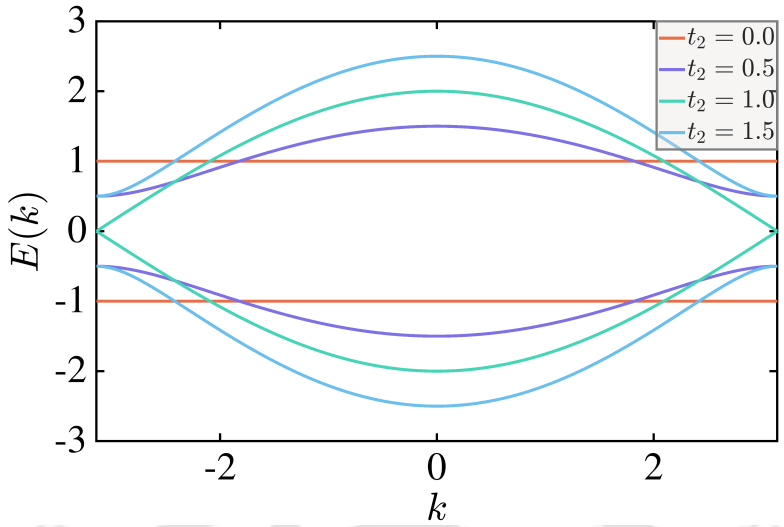

Figure 2.7: Here, we show the dispersion relation corresponding to various values of the inter-cell hopping strength (t_2). In this calculation, the intra-cell hopping strength (t_1) is taken as $t_1 = 1.0$.

where $\mathcal{H}_{\alpha_1,\alpha_2}(k)$ is the bulk-Hamiltonian corresponding to the expression written as,

$$\mathcal{H}_{\alpha_1,\alpha_2}(k) = \begin{pmatrix} 0 & t_1 + t_2 e^{-ik} \\ t_1 + t_2 e^{ik} & 0 \end{pmatrix} \tag{2.66}$$

$$= (t_1 + t_2 \cos(k))\sigma_x + t_2 \sin(k)\sigma_y \tag{2.67}$$

$$= \vec{d}(k).\vec{\sigma} \tag{2.68}$$

where k lies within the first BZ, that is, $-\pi < k < \pi$ and $\vec{\sigma} = (\sigma_x, \sigma_y, \sigma_z)$ denotes the Pauli matrices.

Therefore, the components of the vector $\vec{d(k)}$ are given by,

$$d_x = t_1 + t_2 \cos(k) \tag{2.69}$$

$$d_y = t_2 \sin(k) \tag{2.70}$$

$$d_z = 0. \tag{2.71}$$

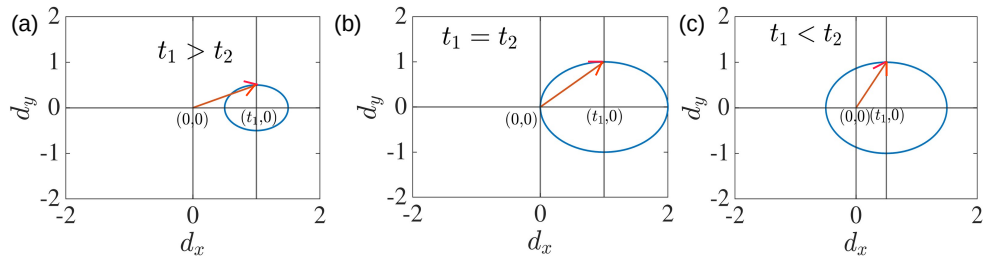

Figure 2.8: Here we have shown the magnitude of the $\vec{d}(k)$ vector for trivial and topological cases. The trajectories of the tip of the vector $\vec{d}(k)$ (k belongs to the first BZ) are shown in the $d_x - d_y$ plane corresponding to the conditions, which are (a) $t_1 > t_2$ (trivial), (b) $t_1 = t_2$ (gap closing point), and (c) $t_1 < t_2$ (topological).

The eigenstates of the bulk-Hamiltonian are given by

$$E(k) = \pm|\vec{d}(k)| = \pm\sqrt{(t_1^2 + t_2^2 + 2t_1t_2\cos(k))} \tag{2.72}$$

which yields the dispersion relation corresponding to various values of t_2) in Fig 2.7, while $t_1 = 1$. Here, the results indicate a flat band corresponding to $t_2 = 0$. Moreover, an energy gap ($\mathcal{E}_{SSH}$) between the filled (lower) and empty (upper) bands corresponding to $t_1 \neq t_2$ (i.e., for $t_2 = 0.5$ and 1.5) and $k = \pm\pi$, is given by,

$$\mathcal{E}_{SSH} = |t_1 - t_2|. \tag{2.73}$$

Therefore, it is depicted that, both the conditions for $t_2 < t_1$ and $t_2 > t_1$ are implying a band gap with an insulating nature. However, we shall see later that, the first case corresponding to $t_1 > t_2$ satisfies a trivial, while the other one with $t_1 < t_2$ is topological in nature. Subsequently, these insulating phases can be distinguished depending on the topological invariant, which is the bulk winding number. Finally, the band gap vanishes at a point $t_1 = t_2$, demonstrating the conducting nature of the model. Further, we study the properties of the vector $\vec{d}(k)$ in the $d_x - d_y$ plane within the BZ in Fig. 2.8 (a-c). In general, the tip of the vector $\vec{d}(k)$ traces out in a closed circle, which is represented by the radius t_2 and center

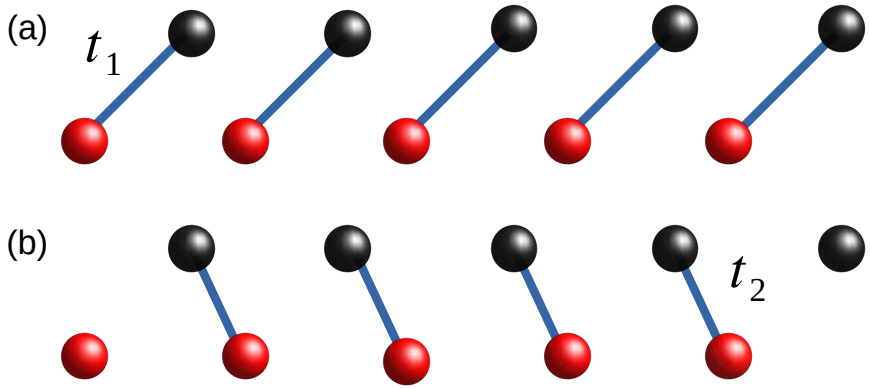

Figure 2.9: We show a schematic diagram of the trivial phase in (a) and the topological phase in (b) corresponding to no isolated site and one isolated site per edge, respectively.

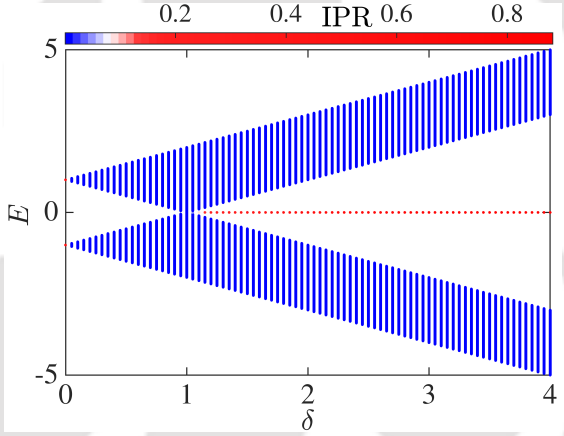

Figure 2.10: The energy spectrum E is plotted as a function of δ. The color bar represents the IPR values corresponding to each of the eigenstates.

point $(t_1, 0)$. Consequently, the bulk winding number denotes the total number of times the vector $\vec{d}(k)$ winds the origin. Therefore, the dispersion relation in addition to $\vec{d}(k)$ vector performs the computation of the winding number. As a result, gapped insulating phases corresponding to $t_1 > t_2$ and $t_1 < t_2$ are distinguished by trivial and topological nature, respectively. Mathematically,

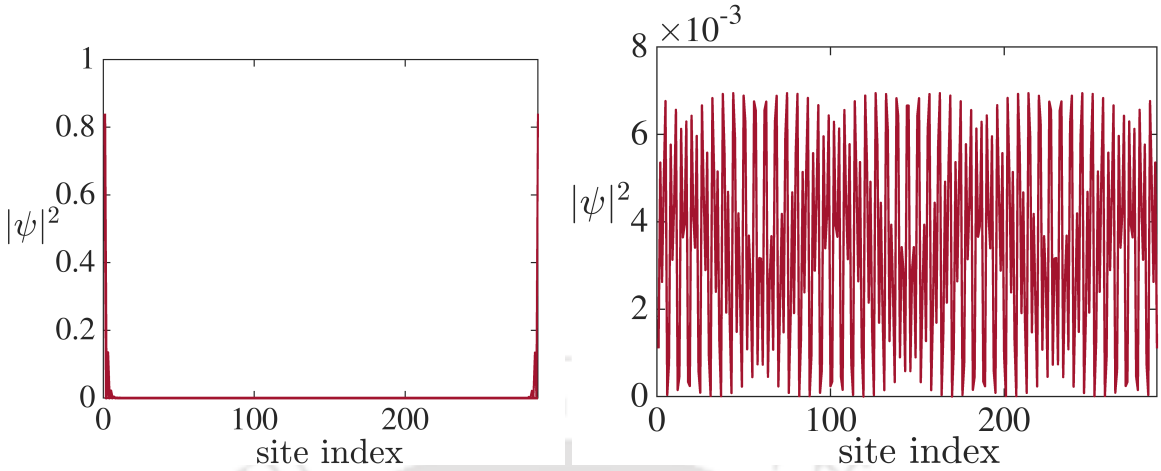

Figure 2.11: Probability distributions of the eigenstates as a function of site index is shown for zero energy in (a) and non-zero energy in (b). The system size is taken as $L = 300$.

winding number can be computed via,

$$\nu = \frac{1}{2\pi i}\int_{-\pi}^{\pi} dk \frac{d}{dk}\log(h(k)) \tag{2.74}$$

where $h(k) = t_1 + t_2 e^{-ik}$. Hence, $\nu = 0$ or 1 signify the trivial and topological phases, respectively.

2.5.3 Finite-size properties

Now we are interested in studying the SSH model with a finite length, which provides another way of understanding the topological properties. Thus, we consider open boundary conditions for the analysis. To begin with, we shall discuss two limiting cases (also known as fully dimerized limit), which are given by

- Case I: when $t_1 \neq 0$ but $t_2 = 0$ (trivial)
- Case II: when $t_1 = 0$ but $t_2 \neq 0$ (topological).

Here, we present these fully dimerized conditions of the SSH model in Fig. 2.9 corresponding to both cases (I and II). In the first case [see Fig. 2.9 (a)], it is observed that, the entire chain breaks into N number of disconnected dimers. On the other hand, in the second case [see Fig. 2.9 (b)], there is $N-1$ number of dimers, in addition to two single sites at both ends of the chain. Since no potential energy is associated with the Hanimtonian, thus these two sites carry zero energy. Therefore, we can infer that, zero-energy modes are present when the intra-cell hopping is absent in this model. Further, examining what will happen at the intermediate values or away from the extreme limits is essential. To do that, we calculate the energy eigenvalues of the Hamiltonian corresponding to the dimerization strength δ. Fig 2.10 shows the energy spectrum as a function of δ where the color bar represents the IPR (see Eq. 1.36) values corresponding to each eigenstate. The observation shows that the system hosts a bulk gap for $\delta < 1$. Subsequently, all the bulk states (non-zero energy states) are extended in nature (IPR $\sim 1/L$). On the other hand, by increasing the dimerization strength δ, zero modes appear in the spectrum. Further, we study these zero-energy states intuitively, we plot the probability distribution of the eigenstates corresponding to these zero and non-zero-modes [Fig 2.11 (a,b)] demonstrates a completely localized at the boundaries and extended throughout the lattice, respectively. Thus, the zero energy edge modes localized at the system boundaries characterize the topological properties of the model. Consequently, topological difference is understandable through these zero energy edge modes, implying a topological phase transition occurring at $\delta = 1$.

Finally, we infer that the topological properties of the SSH model can be characterized by the bulk winding number and the localized zero edge modes. The connection between these two refers to the bulk-boundary correspondence,

well known in the literature. The bulk-boundary correspondence identifies as one of the crucial features of topological insulators. According to this theory, the topological invariants corresponding to the bulk properties can be characterized by the edge modes at the boundaries of the system.

2.6 Topological superconductor: Kitaev chain

Kitaev chain is a paradigmatic model to study a one-dimensional spinless p-wave superconductor [113]. The tight-binding Hamiltonian of the system is given by,

$$H = -t \sum_{j} (\hat{c}_j^{\dagger} \hat{c}_{j+1} + \hat{c}_{j+1}^{\dagger} \hat{c}_j) + \Delta(\hat{c}_j \hat{c}_{j+1} + \hat{c}_{j+1}^{\dagger} \hat{c}_j^{\dagger}) - \mu \sum_{i} (\hat{c}_j^{\dagger} \hat{c}_j - \frac{1}{2}) \tag{2.75}$$

where t denotes the nearest-neighbor hopping strength. $\hat{c}_j^{\dagger}(\hat{c}_j)$ represents the fermionic creation(annihilation) operators at site j. The onsite chemical potential is given by μ. The p-wave superconductor correlation is denoted by Δ. We choose $t = 1$ and Δ to be a real parameter.

In chapter 6, we shall add QP potential in this model. Subsequently, we shall report our finding in the context of localization properties and topological features of this model.

2.6.1 Bulk properties

Since the system is translationally invariant, thus we can apply the Fourier transformation to diagonalize the Hamiltonian in the momentum basis. Thus,

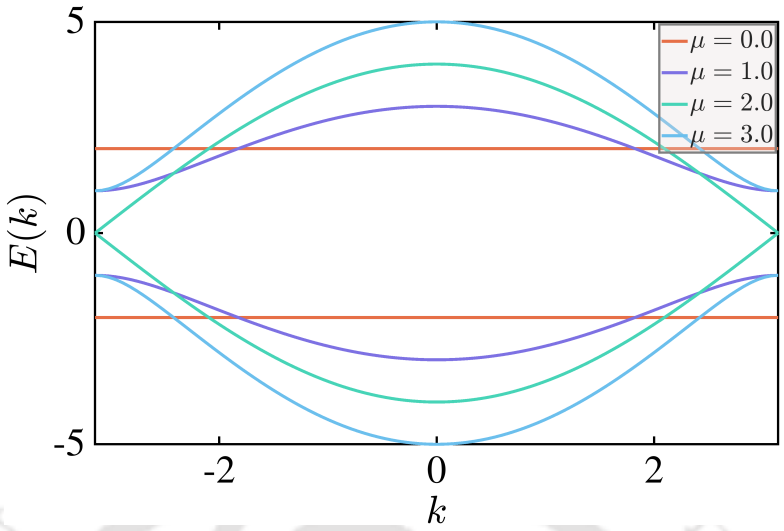

Figure 2.12: Dispersion relation is shown corresponding to different values of chemical potential μ. In this calculation, we have taken $t = \Delta = 1$.

we introduce a particle/hole or Nambu spinor, which is given by,

$$\psi_k^\dagger = (\hat{c}_k^\dagger, \hat{c}_k) \tag{2.76}$$

where

$$\hat{c}_k = \sum_j e^{-ikj} \hat{c}_j \tag{2.77}$$

and k lies in the first BZ. Accordingly, the Hamiltonian can be written as,

$$H = \frac{1}{2} \sum_k \psi_k^\dagger \mathcal{H}(k) \psi_k \tag{2.78}$$

corresponding to 2×2 BdG Hamiltonian $\mathcal{H}(k)$, can be written as,

$$\mathcal{H}(k) = \begin{pmatrix} -2t\cos(k) - \mu & -2i\Delta\sin(k) \\ 2i\Delta\sin(k) & 2t\cos(k) + \mu \end{pmatrix}. \tag{2.79}$$

The energy eigenvalues of the Hamiltonian is given by,

$$E_\pm(k) = \pm\Big[(2t\cos(k) + \mu)^2 + 4\Delta^2 \sin^2(k)\Big]^{1/2}. \tag{2.80}$$

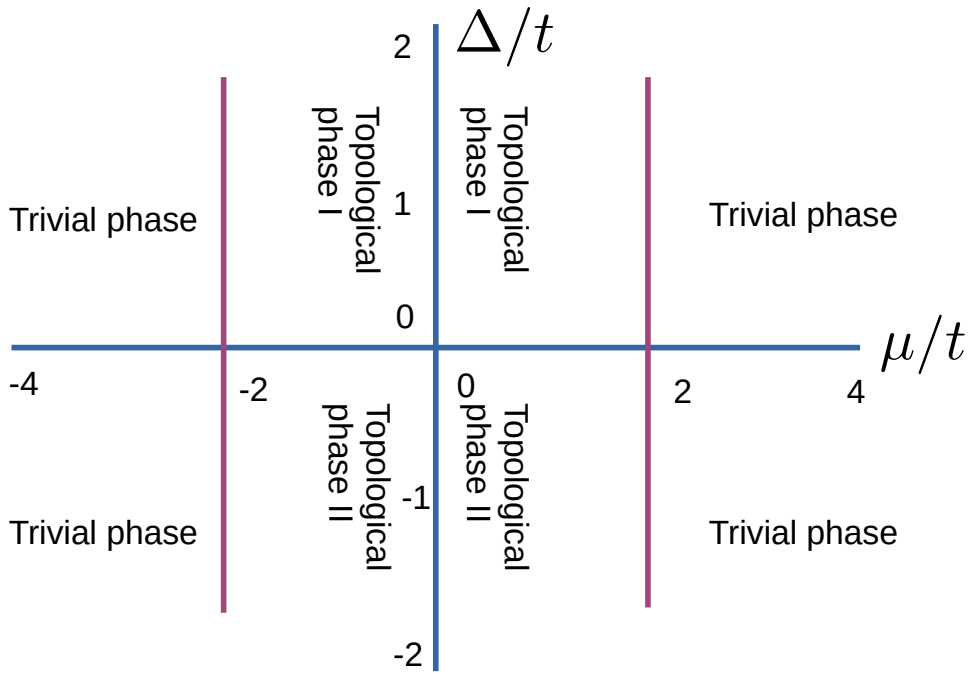

Figure 2.13: Topological phase diagram is shown in the $\Delta/t - \mu/t$ plane.

In Fig. 2.12, we show the dispersion relation corresponding to various values of the chemical potential (μ), namely, $\mu = 0.0,\ 1.0,\ 2.0$, and 3.0 in unit of the hopping t. In this calculation, we have chosen $t = \Delta = 1$. It is illustrated that, the energy gap $\mathcal{E}_{Kitaev} = E_+ - E_-$ depends on momentum k. In addition to that, the system becomes gapless at $\mu = 2$. In the first BZ, the gap closing point occurs at $k = \pm\pi$.

2.6.2 Topological phase diagram

The BdG Hamiltonian [Eq. 2.79] by construction respects the PHS. Consequently, for each eigenstate $|\psi\rangle$ corresponding to an energy $+E$, there has to be another eigenstate $\mathcal{P}|\psi\rangle$ corresponding to energy $-E$. In addition to that, time-reversal symmetry is present, which is given by $\mathcal{T} = I\mathcal{K}$. The product of the

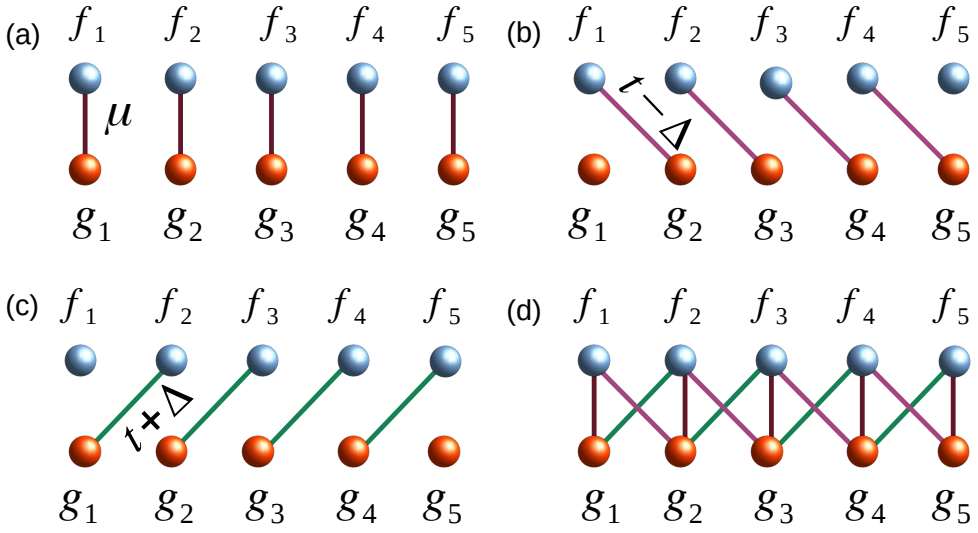

Figure 2.14: Schematic presentations of coupling between Majorana fermions are shown here. The topologically trivial case is presented in (a), while the topologically non-trivial cases are shown in (b) and (c), possessing isolated Majorana fermions are the boundaries. A general pictorial representation comprising all the couplings is shown in (d).

above symmetries yields the chiral symmetry, which is given by $C = \mathcal{T}\mathcal{P}$. Thus, the Kitaev chain belongs to the BDI symmetry class allowing the winding number as the topological invariant. Hence, the winding number is given by,

$$\nu = \frac{1}{2\pi}\int_{-\pi}^{\pi} \partial_k w(k) dk \tag{2.81}$$

where $w(k) = arg\,[2\Delta \sin(k) + i(2t\cos(k) + \mu)]$. The topological phase is characterized by $\nu = \pm 1$, while it is 0 corresponding to the trivial phase. Finally, we in Fig. 2.13 we show the phase diagram in the $\Delta/t - \mu/t$ plane. It is depicted that the topological phase emerges corresponding to $|\mu/t| < 2$ for $\Delta \neq 0$. A phase transition from the topological to the trivial phase occurs at $\mu/t = \pm 2$.

2.6.3 Majorana zero modes

Topological phases are also distinguished by the presence of Majorana zero modes (MZMs). Any Dirac fermion can be written in terms of Majorana fermions, which are given by,

$$c_j = -\frac{1}{2i}(f_j - ig_j) \tag{2.82}$$

$$c_j^\dagger = \frac{1}{2i}(f_j + ig_j). \tag{2.83}$$

Similarly, each of the Majorana fermions can be written in terms of the Dirac fermions, given by,

$$f_j = i(c_j^\dagger - c_j) \tag{2.84}$$

$$g_j = (c_j^\dagger + c_j) \tag{2.85}$$

By substituting Eq. 2.82 and Eq. 2.83 in the Hamiltonian [Eq. 2.75], we will get the Hamiltonian in the Majorana basis. The nearest-neighbor hopping terms of the Hamiltonian Eq. 2.75, can be transformed as,

$$\begin{aligned} c_j^\dagger c_{j+1} &= (-\frac{1}{2i})(\frac{1}{2i})(f_j + ig_j)(f_j - ig_j) \\ &= \frac{1}{4}[f_j f_{j+1} - if_j g_{j+1} + ig_j f_{j+1} + g_j g_{j+1}] \end{aligned} \tag{2.86}$$

and

$$\begin{aligned} c_{j+1}^\dagger c_j &= (c_{j+1}^\dagger c_j)^\dagger \\ &= \frac{1}{4}[f_{j+1} f_j + ig_{j+1} f_j - if_{j+1} g_j + g_{j+1} g_j] \end{aligned} \tag{2.87}$$

Thus, we get,

$$-t(c_j^\dagger c_{j+1} + c_{j+1}^\dagger c_j) = -\frac{it}{2}[g_j f_{j+1} - f_j g_{j+1}]. \tag{2.88}$$

The superconducting correlation terms are transformed as,

$$\begin{aligned} c_j c_{j+1} &= (-\frac{1}{2i})(-\frac{1}{2i})(f_j - ig_j)(f_{j+1} - ig_{j+1}) \\ &= -\frac{1}{4}[f_j f_{j+1} - if_j g_{j+1} - ig_j f_{j+1} - g_j g_{j+1}] \end{aligned} \tag{2.89}$$

and

$$\begin{aligned} c_{j+1}^{\dagger}c_{j}^{\dagger} &= (c_j c_{j+1})^{\dagger} \\ &= -\frac{1}{4}[f_{j+1}f_j + ig_{j+1}f_j + if_{j+1}g_j - g_{j+1}g_j] \end{aligned} \tag{2.90}$$

which yields,

$$\Delta(c_j c_{j+1} + c_{j+1}^{\dagger}c_j^{\dagger}) = \frac{\Delta i}{2}[f_j g_{j+1} + g_j f_{j+1}]. \tag{2.91}$$

In addition, the onsite term can be written as,

$$\begin{aligned} c_j^{\dagger}c_j &= (-\frac{1}{2i})(\frac{1}{2i})(f_j + ig_j)(f_j - ig_j) \\ &= \frac{1}{2}[1 + ig_j f_j]. \end{aligned} \tag{2.92}$$

Finally, the Hamiltonian, in terms of Majorana fermions, is written as,

$$\begin{aligned} H &= -t\sum_i (c_j^{\dagger}c_{j+1} + c_{j+1}^{\dagger}c_j) + \Delta(c_j c_{j+1} + c_{j+1}^{\dagger}c_j^{\dagger}) - \mu\sum_i (c_j^{\dagger}c_j - \frac{1}{2}) \\ &= \frac{i}{2}\sum_i [(t+\Delta)f_j g_{j+1} + (t-\Delta)f_{j+1}g_j + \mu f_j g_j]. \end{aligned} \tag{2.93}$$

Now we discuss two special cases in the following.

- **Topologically trivial case ($\Delta = t = 0$ and $\mu < 0$)**

  In this case, the Hamiltonian becomes,

  $$H = -\frac{i\mu}{2}\sum_j g_j f_j \tag{2.94}$$

  which can be seen in Fig. 2.14 (a). Here, all the Majorana fermions at the same site are connected pairwise, resulting in no isolated at the edges.

- **Topologically non-trivial case ($\Delta = t > 0$ and $\mu = 0$)**

  In this case, the Hamiltonian becomes,

  $$H = it\sum_j f_j g_{j+1} \tag{2.95}$$

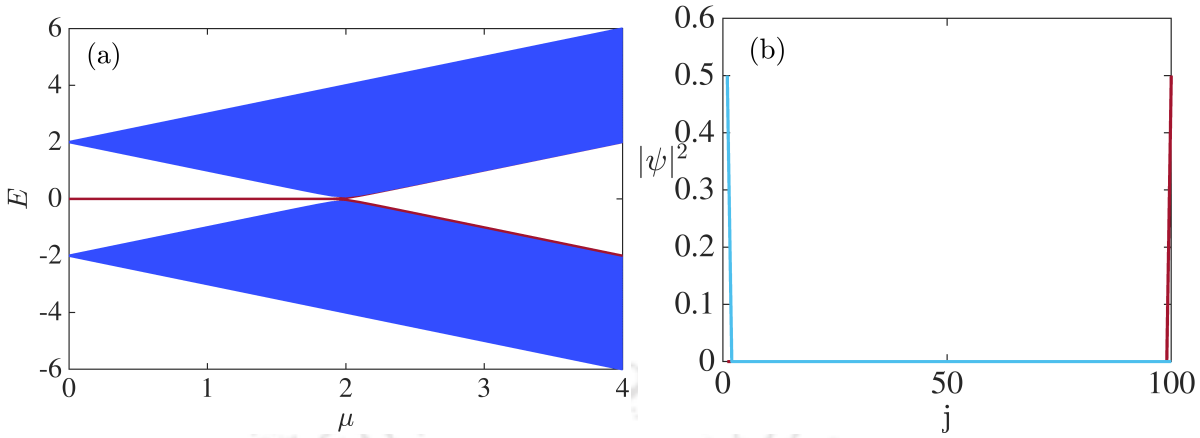

Figure 2.15: (a) Energy spectrum is plotted as a function of chemical potential μ corresponding to $t = \Delta = 1$. (b) The probability distribution of the zero-energy mode as a function of site index j is shown. In this calculation, the system length is taken as $L = 100$.

subsequently, the Majorana fermions coupled in a fashion which are shown in Fig. 2.14 (b-c) It is observed that by the combination of the hopping strength (t) and superconducting pairing term (Δ), a Dirac fermion split into two Majorana components which can be found at each end of the chain. These two Majorana modes do not appear in the Hamiltonian because of their zero energy. As a result, these zero-energy Majorana modes are robust against perturbation. This situation exists up to a parameter range $|\mu| < 2t$. Beyond this limit, the edge modes gain energy and hybridize with the bulk band.

2.6.4 Finite-size properties

Here, we study the real-space properties of the Kitaev chain. In order to do that, we solve the Hamiltonian under the open boundary condition. Fig. 2.15 (a)

shows the energy spectrum as a function of μ corresponding to $t = \Delta = 1$. We observe a phase transition from topologically non-trivial to trivial phase through a gap closing point at $\mu = 2$. The topological(trivial) phase is characterized by the presence(absence) of the zero-energy states. Further, we also plot the probability distribution of the zero-energy states as a function of site index (j) in Fig. 2.15 (b) corresponding to two distinct points of $\mu = 0.5$ and 2.5, which belong to the topologically non-trivial and trivial phases, respectively. We observe a localized behavior by the zero-energy states, while the bulk state shows an extended nature.

2.6.5 Real-space winding number

Until now, our understanding has been based on the system without any external potential. However, in presence of a potential the scenario would be different. it is well established that the system remains topologically non-trivial for weaker potential strength as long as the relevant symmetries protecting the topology remain unbroken. However, a strong potential strength undergoes a phase transition from a non-trivial to a trivial phase. Since any disorder breaks the translational symmetry of the a Hamiltonian, we shall use the real-space winding number as the topological invariant [131, 132]. The real-space winding number is defined as,

$$\nu = \frac{1}{L'} Tr\Big(\Gamma Q[Q, X]\Big) \tag{2.96}$$

where Γ and X are the chiral symmetry and the position operator, respectively. The operator, Q can be calculated as,

$$Q = \sum_{j=1}^{L} (|j\rangle\langle j| - |j'\rangle\langle j'|) \tag{2.97}$$

where $|j'\rangle = \Gamma^{-1}|j\rangle$ and $|j\rangle$ denotes the eigenstates of the Hamiltonian. Tr represents the trace of the sites with the given length $L' = \frac{L}{2}$, where L represents the system length.

2.7 Bose-Hubbard model

In an effect to study the critical properties for an interacting system, we have explored the physics of the Bose-Hubbard model in presence of a QP potential using mean-field theory.

In 1963, the Hubbard model was first introduced by J. Hubbard, describing the electronic configuration in strongly correlated systems [133]. Consequently, this model was invented to study the fermionic system. Later, in 1989, the idea got extended to the bosonic systems by Fisher et al., yielding the Bose-Hubbard model (BHM) [134]. In 1998, Jaksh et al. proposed an experiment using the ultracold bosonic atoms in optical lattices, which was realized by M. Greiner et al. in 2002 [135].

The Bose-Hubbard model Hamiltonian can be written as [135],

$$H = -t \sum_{<i,j>} \hat{b}_i^\dagger \hat{b}_j + \frac{U_0}{2} \sum_j \hat{n}_j(\hat{n}_j - 1) + \sum_j (\mu - \varepsilon_j)\hat{n}_j \tag{2.98}$$

where t denotes the nearest-neighbor hopping strength. $\hat{b}_j^\dagger$ ($\hat{b}_j$) represents the bosonic creation (annihilation) operator and $\hat{n}_j = \hat{b}_j^\dagger \hat{b}_j$ is the number operator at site j which follows the usual bosonic relation $[\hat{b}_j, \hat{b}_j^\dagger] = \delta_{i,j}$. The onsite interaction potential strength is given by U_0. μ and ε_j represent the chemical potential that maintains the particle number and onsite external potential, respectively.

Since this model has been well studied through the years, an extensive study

of this topic has been reported in the literature. Here we only present concise known results in the context of the properties of the BHM, which are relevant to our study in the chapter. 7.

2.7.1 Phases of the BHM

In this discussion, we ignore the third term of the Hamiltonian for simplification. Thus, the Hamiltonian becomes,

$$H = -t \sum_{<i,j>} \hat{b}_i^\dagger \hat{b}_j + \frac{U_0}{2} \sum_j \hat{n}_j(\hat{n}_j - 1). \tag{2.99}$$

Depending on the system parameters, such as, hopping strength (t), on-site interaction potential strength (U_0) and the occupation density $\rho = \frac{N}{L}$ (where N and L represent the number of atoms and lattice sites), there are several phases emerge in the system. Lets now explore them in the following.

- **The perfect superfluid limit ($\frac{U_0}{t} \to 0$)**

  In this limit the kinetic energy is excessively larger than the interaction potential strength, that is $t >> U_0$. As a result, the atoms are tending to extend throughout the entire lattice, hence called the superfluid phase. All the atoms occupy the superfluid ground state corresponding to zero momentum ($\boldsymbol{k} = 0$), which is given by [136],

  $$|\Psi_{SF}\rangle \propto \left(\sum_{j=1}^{L} \hat{b}_j^\dagger \right)^N |0\rangle \tag{2.100}$$

  average density of bosons is a fraction for the superfluid case.

- **The perfect Mott insulator limit ($\frac{U_0}{t} \to \infty$)**

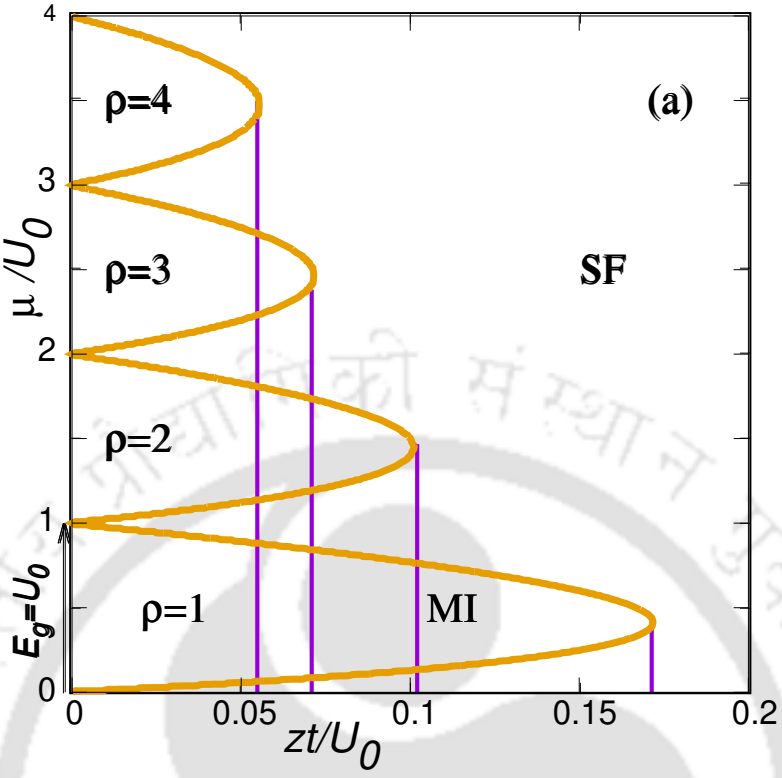

Figure 2.16: A phase diagram of a homogeneous BHM is shown here. The lobe shapes from the phase diagram represent the MI phase, while the rest belong to the SF phase. The vertical line indicates the critical transition points. The figure is taken from Ref. [8].

In this limit, the onsite interaction potential strength (U_0) dominates over the hopping strength (t), that is, $t << U_0$. As a results, the atoms are localized at the lattice sites, hence called Mott insulating phase. The many-body ground state can be written as [136],

$$|\Psi_{MI}\rangle \propto \left(\prod_{j=1}^{L} \hat{b}_j^{\dagger}\right)^{n_j} |0\rangle \tag{2.101}$$

where n_j denotes the number of atoms in each lattice site j, which is as integer here.

2.7.2 Phase diagram

In Fig. 2.16, we show the phase diagram in the parameter space $\mu/U_0 - zt/U_0$ plane. z denotes the coordination number which depends on the system dimension d via $z = 2d$. Here, we observe the MI phase with a lobe shape corresponding to an integer occupation densities per site, that is, $\rho = 1, 2, \ldots$ It is illustrated that, at $t = 0$, the energy gap (E_g) in the particle-hole excitation spectrum is equal to the onsite interaction strength U_0. With increasing the hopping strength, the MI phase remains constant until the critical hopping strength $\eta_c = zt_c/U_0$. Further, increasing the hopping strength beyond the η_c, the system exhibits a phase transition to the SF phase. In the SF phase occupation density does not remain integer due to the extended nature of the atoms. Following the mean-field approximation, the boundary between SF and MI phases can be analytically calculated, which is given by [137],

$$\frac{t}{U_0} = \frac{1}{z}\frac{(1-\rho+\mu/U_0)(\rho-\mu/U_o)}{(1+\mu/U_0)}. \tag{2.102}$$

We induce a QP potential in the Hamiltonian given in Eq. 2.98 and study the resulting phase diagram in chapter.7.

CHAPTER 3

PROPERTIES OF A TIGHT BINDING CHAIN IN PRESENCE OF ONSITE AND HOPPING QUASIPERIODIC POTENTIAL

In this chapter, our motivation is twofold. It has been realized that, quantum systems with a quasiperiodically modulated hopping/off-diagonal term or an onsite potential, or both of them exhibit distinct physical characteristics [59, 67, 66]. Thus, it will be interesting to explore them one by one. In addition, in the last chapter, we have studied the formalism of the critical state analysis in sec. 2.3.3. Before applying it to more complicated systems, we aim to employ that formalism for the pure AA model (onsite QP modulation) [18], and its generalized version (off-diagonal and onsite, both being quasiperiodically modulated). In the first part, we shall apply the critical state analysis on the pure AA model, and hence computing the critical potential strength and the corresponding critical exponents. At the end, we shall comment on the universality class based on the data collapse plot and establish a scaling law between these critical exponents. In the second part, we shall modulate the hopping strength quasiperiodically on a one-dimensional tight-binding chain together with an onsite quasiperiodic term. Such a model will allow us to compare the results for the pure AA model. We shall obtain the phase diagram, fractal dimension, and finite-size scaling analysis, and conclude our results at the end of the chapter.

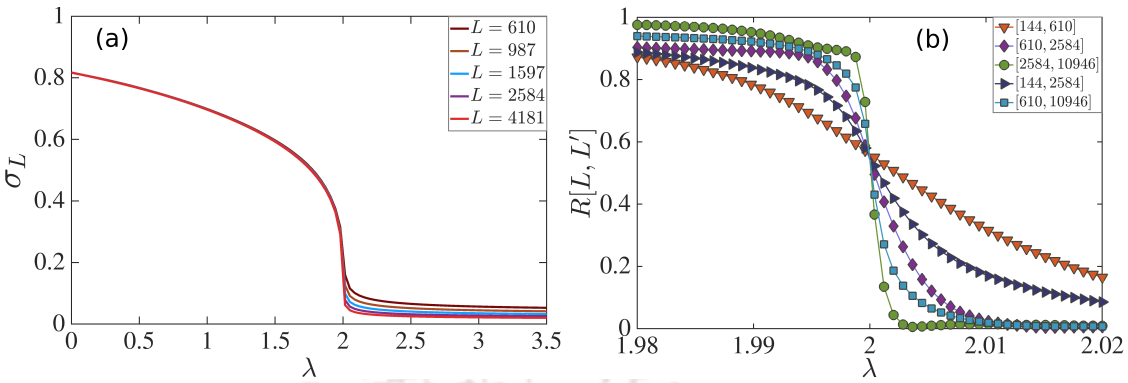

Figure 3.1: (a)The order parameter σ_L corresponding to various system sizes are plotted. In this calculation, the system sizes are taken as $L = 610, 987, 1597, 2584, 4181$. (b) The two system sizes variable $R[L, L']$ in the vicinity of the critical point λ_c is shown corresponding to sets of $[L, L']$, which are written in the legend of the figure.

3.1 Critical-state analysis of the pure AA model

The Hamiltonian of the AA model in presence of onsite QP potential is shown in Eq. 1.19 to be self contained, we write it again here. The pure AA Hamiltonian is given by,

$$H = t \sum_{j=1}^{L} (c_{j+1}^{\dagger} c_j + h.c.) + \lambda \sum_{j=1}^{L} \cos(2\pi\beta j + \theta) c_j^{\dagger} c_j. \tag{3.1}$$

It is known that the Hamiltonian undergoes a phase transition from a completely extended phase to a localized phase through a critical transition point $\lambda_c = 2t$ [138, 18]. Here, in our calculation, without any loss of generality we set $t = 1$. Using the critical state analysis, discussed in the second chapter (sec. 2.3.3), we can validate the phase transition scenario, and the critical point of the AA model [18].

Here, we start our discussion by calculating NPR values corresponding to each of the eigenstates for the Hamiltonian written in Eq. 3.1. These computed

NPR values yield the order parameter, which we denote by σ. In the calculation of σ, we take an average value of the NPR over all the eigenstates corresponding to the AA Hamiltonian. We want to observe how the order parameter behaves under the influence of the onsite QP potential present in the system. Thus, we plot σ for different lengths, that is, σ_L as a function of λ in Fig. 3.1 (a) corresponding to various system sizes, namely L = 610, 987, 1597, 2584, 4181. There is a subtle point that deserves special mention here. The sizes chosen are all members of the Fibonacci sequence, and the ratio of two successive number obey a golden ratio, such as, $\beta = (\sqrt{5} - 1)/2$.

We notice that the response of σ_L as a function of λ is significantly different while approaching towards the critical point from above or below the critical potential strength (λ_c). Subsequently, σ_L becomes system size independent for $\lambda < \lambda_c$, while it scales as $\frac{1}{\sqrt{L}}$ corresponding to $\lambda > \lambda_c$. Thus, it is clear that there is phase separation occurs around $\lambda \simeq 2$. Further, this observation leads us to compute the two system sizes variable, namely $R[L, L']$ in the vicinity of λ_c. Hence, in Fig. 3.1 (b) we plot $R[L, L']$ as a function of λ corresponding to several sets of L and L'], which is shown in the legend of the figure. It is observed that, curves corresponding to distinct L and L' cross each other at a specific point. The abscissa and the ordinate of the crossing point supply information of the critical transition point (λ_c) and the critical exponents or a ratio of two of them namely, (γ/ν) , respectively. Subsequently, the crossing point from our calculation yields $\lambda_c \sim 2.00$ and $\gamma/\nu \sim 0.55$.

Moreover, the correlation length exponent (ν) can be computed using the data collapse method. Here, we plot $\sigma_L^2 L^{1-\frac{\gamma}{\nu}}$ versus $|\varepsilon|L^{1/\nu}$ (see Eq. 2.30) corresponding to several system sizes, L = 2584, 4181, 6765, and 10946 which again

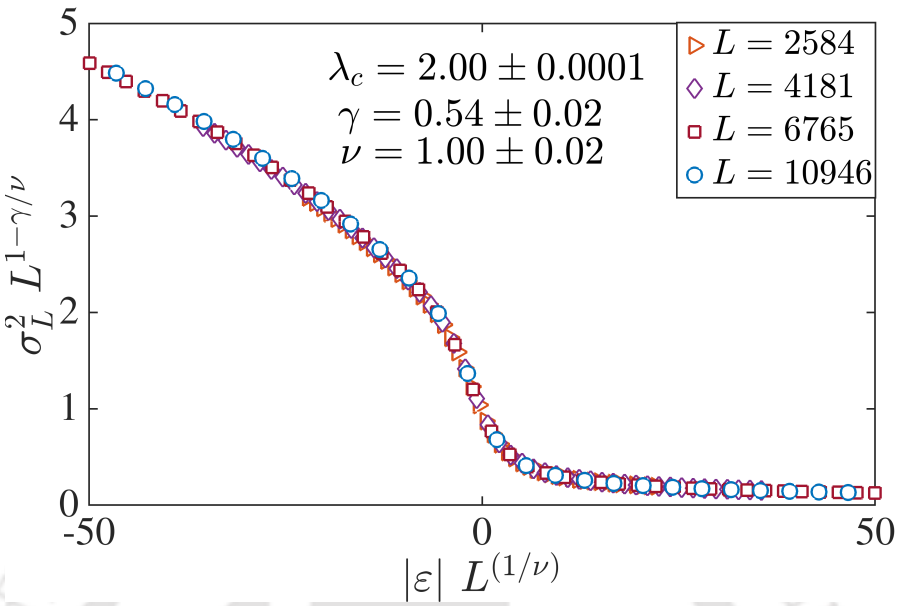

Figure 3.2: A data collapse with the σ_L^2 data in the vicinity of the transition point corresponding to various system sizes are shown here. In this calculation the system sizes are taken as L = 2584, 4181, 6765, and 10946.

are members of the Fibonnacci family in Fig. 3.2. We expect that, corresponding to the correct values of the critical transition point (λ_c) and the critical exponents, all the data curves will collapse onto each other, yielding a single universal curve. Therefore, this plot satisfies the scaling hypothesis by following Eq. 2.30, where $G(\varepsilon L^{1/\nu})$ denotes the single curve. In our analysis, we observe a nice data collapse by yielding λ_c = 2.00±0.0001, ν = 1.00±0.02, and γ = 0.54±0.02. Therefore, the calculated critical transition point by the method we used here exactly matches with the known results available in the literature. In addition to that, the choices that satisfy the data collapse method can also be checked from the plot Fig. 3.1 (b). Furthermore, we can validate all the computed critical exponents, which satisfy a hyper-scaling relation [103], given by,

$$\frac{2\beta}{\nu} + \frac{\gamma}{\nu} = 1. \tag{3.2}$$

The order parameter σ_L and participation ratio PR_L=1/IPR_L, scales with L via

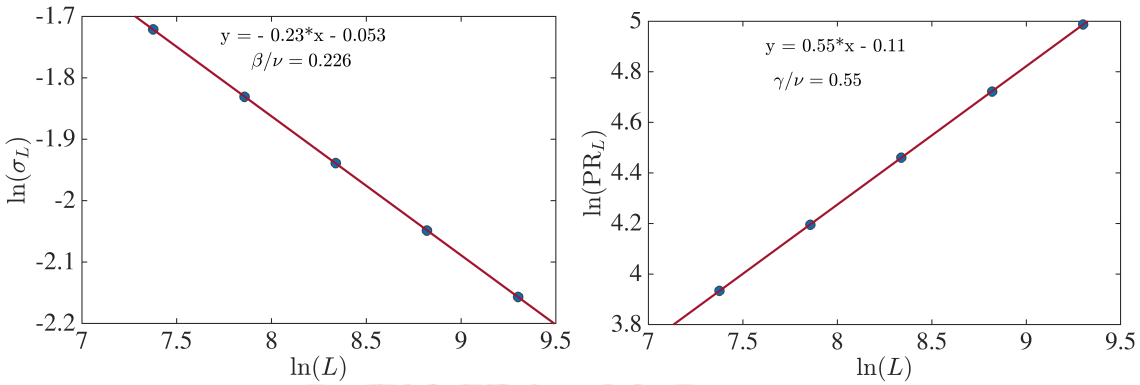

Figure 3.3: Here we calculate the exponent ratio, γ/ν and β/ν by plotting $\ln(\sigma_L)$ and $\ln(\mathrm{PR}_L)$ as a function of $\ln(L)$ in (a) and (b), respectively. In this calculation the system sizes are taken as $L = 1597,\ 2584,\ 4181,\ 6765$, and 10946.

the relations given by,

$$\sigma_L \sim L^{-\beta/\nu} \quad ; \quad \mathrm{PR_L} \sim L^{\gamma/\nu} \tag{3.3}$$

which are obtained from Eq. 2.25. Thus, the log-log plots of the observables (σ_L and PR_L) with the system sizes, L result in a linear straight line corresponding to slopes, β/ν and γ/ν, respectively. Thus, we plot $\ln(\sigma_L)$ and $\ln(\mathrm{PR}_L)$ as a function of $\ln(L)$ for different sizes $L = 1597,\ 2584,\ 4181,\ 6765$, and 10946 in Fig. 3.3. The critical exponents obtained from these plots are given by $\beta/\nu \approx 0.226$ and $\gamma/\nu \approx 0.54$. Therefore, using the value of β/ν and γ/ν, we can clearly satisfy the hyper-scaling relation in Eq. 3.2 at $\lambda_c \approx 2.00$.

Finally, we calculate the fractal dimension (D_2) [see Eq. 2.5 for definition] corresponding to all the eigenstates as a function of λ in Fig. 3.4 (a). A sharp localization transition is observed at $\lambda = 2$ where the values of D_2 turn out to be fractions. As expected, the result also matches with the ratio of critical exponent $\gamma/\nu \approx 0.54$ from the above calculation, which is an average study over all the eigenstates. Thus, we can conclude that all the eigenstates are multifractal in nature at the transition point. In order to understand this scenario intuitively,

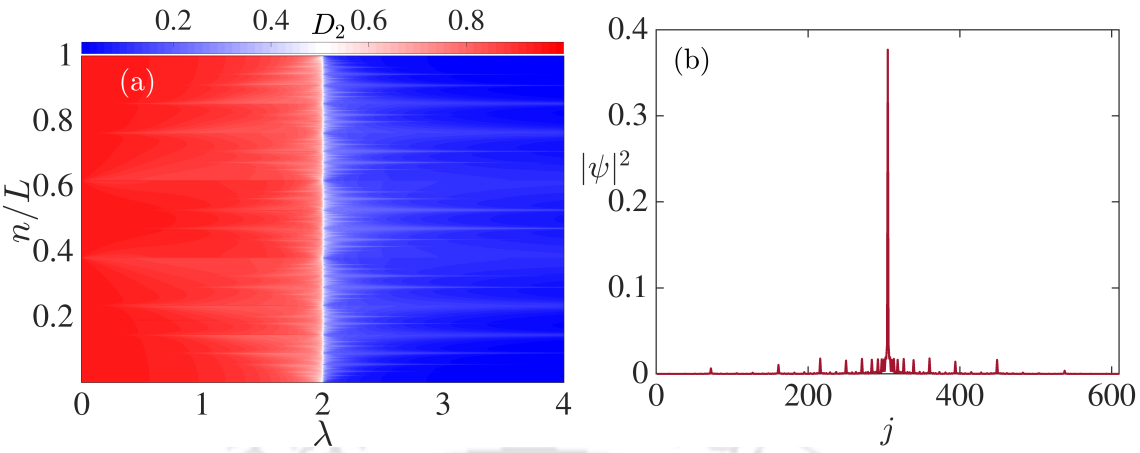

Figure 3.4: (a) The fractal dimension (D_2) is shown for all the eigenstates as a function of the potential strength λ. (b) The probability distribution of the ground state as a function of site index (j) corresponding to $\lambda = 2$ is shown. In this calculation, the system size is taken as $L = 610$.

we plot the probability distribution of the ground state as a function of site index (j) for the system size $L = 610$ in Fig. 3.4 (b). We clearly observe a fractal nature of the eigenstate.

3.2 Generalized AA model: case of modulated hopping

In this section, we wish to extend our study by exploring a more generalized version of the pure AA model. We chose a one-dimensional chain in presence of onsite QP potential, which is already known as the AA model. Moreover, we include a quasiperiodically modulated hopping in addition to the uniform nearest-neighbor hopping strength. In the tight-binding limit, the Hamiltonian of the system is given by [139],

$$H = \sum_j (t + V_1)\,(\hat{c}^\dagger_{j+1}\hat{c}_j + h.c.) + \lambda_2 \sum_j \cos(2\pi\beta j)\,\hat{c}^\dagger_j\hat{c}_j \tag{3.4}$$

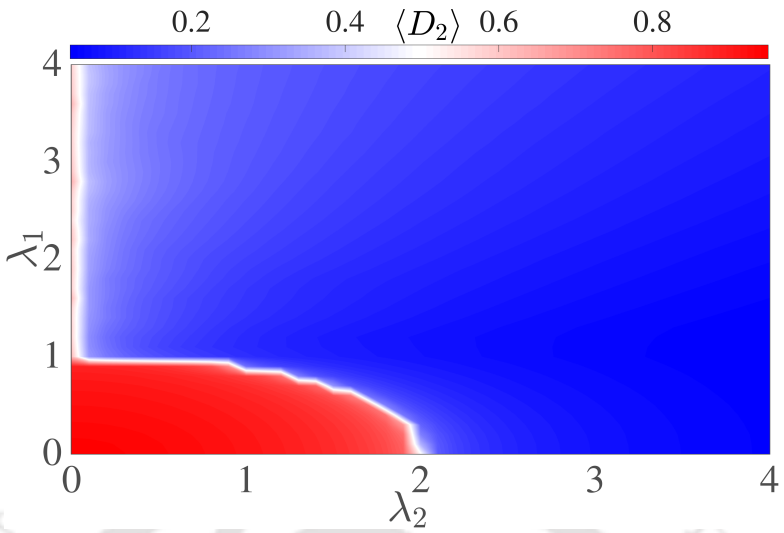

Figure 3.5: (a) The phase diagram is shown via average of fractal dimenison $\langle D_2 \rangle$ as function of λ_1 and λ_2. In this calculation, the system size we consider is $L = 4181$.

where t denotes the nearest neighbor uniform hopping strength. Following the AA model, the onsite potential varies quasiperiodically, corresponding to potential strength λ_2. Further, we incorporate an inhomogeneity in the hopping strength via cosine modulations, which is given by,

$$V_1 = \lambda_1 \cos(2\pi\beta j). \tag{3.5}$$

where λ_1 represents the QP modulation strength of the hopping term. $\hat{c}_j^\dagger(\hat{c}_j)$ is the creation(annihilation) operator at the site j. The periodicity of both modulations (hopping and onsite QP potentials) are denoted by $1/\beta$. As usual, we choose β to be an irrational number, in particular a golden value, which is $\beta = \frac{\sqrt{5}-1}{2}$. Here, all the energies are taken as a unit of t, that is, $t = 1$.

3.2.1 Phase diagram

Now, we intend to understand how the localization properties are affected under the competition between λ_1 and λ_2. In order to do that, we start our analysis by calculating the fractal dimension (D_2) [see Eq. 2.5] corresponding to all the eigenstates of the Hamiltonian. In Fig. 3.5, we plot a phase diagram from the information obtained via the average value of D_2 ($\langle D_2 \rangle$) over all the eigenstates as a function of λ_1 and λ_2. Different phases, such as extended, localized, and critical phases, are separated by a color bar. Specifically, red (blue) in the color bar denotes the extended (localized) phase, while the intermediate color represents a critical phase comprising of eigenstates that are critical in nature. By recalling the known results corresponding to $\lambda_1 = 0$, the Hamiltonian can be mapped onto the pure AA model Hamiltonian [[18]]. Consequently, a complete localization transition occurs at $\lambda_2 = 2$ from a completely extended phase to a localized phase.

On the other limit, corresponding to $\lambda_2 = 0$ the system undergoes a phase transition from an extended to a critical/multifractal phase at $\lambda_1 = 1$. Thus, a conventional localization transition is absent in this scenario. In order to understand the nature of the eigenstates that belong to the critical phase needs more attention. We shall explore them in the following paragraph. Further, the localization transition is observed with increasing the value of λ_2 till $\lambda_1 \leq 1$. Beyond this limit of λ_1, the system suffers a complete localization for any strength of the onsite QP potential strength.

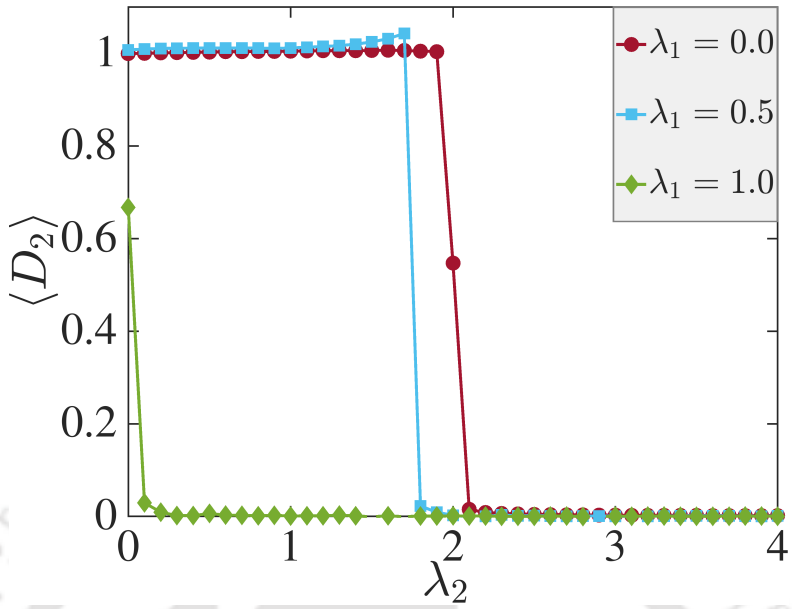

Figure 3.6: (a) We show the $\langle D_2 \rangle$ as function of λ_2 corresponding to various values of λ_1. For the finite-size scaling analysis, we choose the system sizes, which are $L = 6765,\ 4181,\ 2584,\ 1597$,and 987.

3.2.2 Finite-size scaling analysis

Next, a finite-size analysis is required for a concrete understanding of the phase transitions, that are clearly observed in the phase diagram. Thus, we plot D_2 averaged over all the eigenstates as a function of the onsite potential strength λ_2 for various values of $\lambda_1 = 0.0,\ 0.5,\ 1.0$ in Fig. 3.6. In this calculation, the fractal dimension is calculated by choosing the system sizes, such as, $L = 6765,\ 4181,\ 2584,\ 1597$,and 987. We observe that, $\langle D_2 \rangle$ varies from 1 to 0 by changing λ_2 corresponding to $\lambda_1 = 0$. Also, it is interesting to check that, at $\lambda_2 = 2$, the value of $\langle D_2 \rangle$ is 0.5, which we have found in the pure AA case. Furthermore, we observe the onset of localization transitions starts early corresponding to $\lambda_1 = 0.5$ and 1.0 compare to the pure AA condition, that is $\lambda_1 = 0.0$,

.

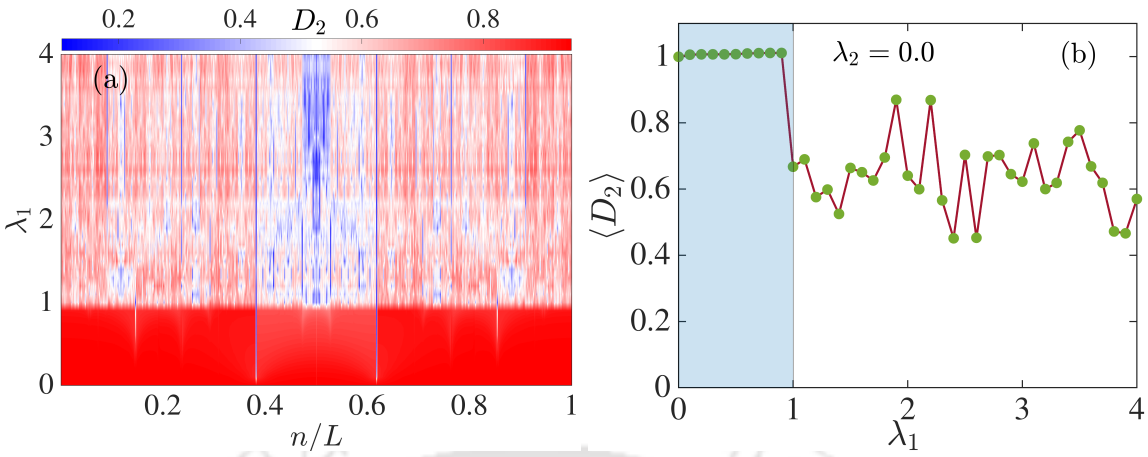

Figure 3.7: Here, we plot D_2 as a function of λ_1 and eigenstate indices in (a) corresponding to $\lambda_2 = 0.0$. The system size for this calculation is taken as $L = 987$. Next, in (b) we show the $\langle D_2 \rangle$ as function of λ_1 corresponding to $\lambda_2 = 0.0$. For the finite-size scaling analysis, we choose the system sizes, which are $L = 6765,\ 4181,\ 2584,\ 1597$,and 987.

Now we only focus on the off-diagonal part of the Hamiltonian. Thus, we plot the fractal dimension D_2 for all the eigenstates as a function of λ_1 corresponding to $\lambda_2 = 0.0$ in Fig. 3.7 (a). All the eigenstates exhibit a phase transition from an extended to a multifractal states at $\lambda_1 \sim 1$, resulting in an absence of a mobility edge. In Fig. 3.7 (b), we also plot the $\langle D_2 \rangle$ as a function of λ_1 corresponding to $\lambda_2 = 0.0$. It clearly reveals that, beyond $\lambda_1 \approx 1$, the eigenstates are multifractal in nature, yielding fractional value of $\langle D_2 \rangle$.

3.3 Conclusions

We consider a one-dimensional non-interacting chain in presence of QP potential, which is studied by the pure AA model. In addition, we choose a gen-

eralized version of the AA model by modulating the hopping term quasiperiodically in addition to its uniform nearest-neighbor strength. In the pure AA model, a metal-insulator phase transition under the competition between the kinetic and potential energy is well established. As an exercise, using the critical state analysis, we have computed the critical transition point, which exactly matches with the known result ($\lambda = 2t$). Moreover, we have calculated the critical exponents and established the scaling law between them. Also, we have added the QP modulation hopping term in this model. By computing the fractal dimension, we have found that the system hosts a phase transition from an extended phase to a multifractal phase in the absence of the onsite QP potential. We have verified our results via finite-size scaling analysis. Finally, we observe that at a higher value of the hopping modulation strength, the system behaves as the Anderson model in 1D, thereby causing localization of all the eigenstates for any finite value of the onsite potential strength.

CHAPTER 4

REENTRANT LOCALIZATION TRANSITION IN PRESENCE OF A QUASIPERIODIC POTENTIAL

4.1 Introduction

So far it has been well established that after the system undergoes a localization transition, all the states remain localized forever with increasing disorder strength. In this chapter we show that this is not always true. This is indeed the case for a tight-binding chain with two atoms per unit cell, or equivalently a dimerized hopping. By dimerized hopping we mean that the inter-cell hopping is different than the inter-cell one. The model is known as the SSH Model [108]. We shall show that in such a one dimensional dimerized lattice with staggered quasiperiodic disorder, the competition between dimerization and quasiperiodic disorder leads to a '*reentrant localization*' transition. This means, some of the localized states become once again conducting for a range of the quasiperiodic potential. Further increase in the disorder strength leads to a second localization transition where all the states become eventually localized. The corresponding Hamiltonian thus contains elements of both the AA and the SSH models, and the reentrant localization transition is a competition between the dimerization and the quasiperiodic potential. This re-entrant localization transition is also associated with separate critical regions hosting the mobility edges (MEs) in the spectrum.

Here, we start the analysis by presenting a model Hamiltonian corresponding to two special cases, such as the uniform and the staggered disorder cases. This two scenarios correspond to the onsite QP potential distribution at the lat-

tice sites in a unit cell. In the uniform disorder case, the strengths of the potential at the two sublattices are the same, while they are equal and opposite in magnitude for the staggered disorder case. In particular, we study the localization properties of this system by analyzing the phase diagram. In addition, the presence of the onsite potential in the dimer model (SSH model) breaks the chiral symmetry, thereby making the resultant system to loose the topological properties. Consequently, no zero energy edge mode is expected to be observed. However, we are still interested in studying the QP potential effects on the edge modes which were otherwise there when there was no quasiperiodic potential. Finally, we support our observations by using a finite-size scaling analysis and conclude our results.

4.2 Model

We consider a one dimensional dimerized lattice with onsite quasiperiodic potential which is given by the Hamiltonian; [140]

$$H = -t_1 \sum_{i=1}^{N} (\hat{c}_{i,B}^{\dagger} \hat{c}_{i,A} + h.c.) - t_2 \sum_{i=1}^{N-1} (\hat{c}_{i+1,A}^{\dagger} \hat{c}_{i,B} + h.c.) + \sum_{i=1}^{N} \lambda_A \hat{n}_{i,A} \cos[2\pi\beta(2i-1)] + \sum_{i=1}^{N} \lambda_B \hat{n}_{i,B} \cos[2\pi\beta(2i)]. \quad (4.1)$$

This is a chain of N unit cells comprising of two sublattice sites A and B. i represents the unit cell index and $L = 2N$ is the length of the chain. $\hat{c}_{i,A}^{\dagger}$ ($\hat{c}_{i,A}$) and $\hat{c}_{i,B}^{\dagger}$ ($\hat{c}_{i,B}$) are the creation (annihilation) operators corresponding to sites in the A and B sublattices which we denote by (i, A) and (i, B) and the site number operators are denoted as $\hat{n}_{i,A}$ and $\hat{n}_{i,B}$. The intra- and inter-cell hopping strengths are represented by t_1 and t_2 respectively and $h.c.$ stands of the hermitian conjugate.

The strength of the onsite potential at the sublattice site A (B) is represented by λ_A (λ_B) and β determines the period of quasiperiodic potential. The uniform and staggered disorder are introduced by assuming $\lambda_A = \lambda_B = \lambda$ and $\lambda_A = -\lambda_B = \lambda$ in Eq. 4.1, respectively.

The model Eq. 4.1 in the limit of vanishing disorder i.e. $\lambda = 0$, is the paradigmatic Su-Schrieffer-Heeger (SSH) model [108] which exhibits a trivial (when $t_1 > t_2$) to topological (when $t_1 < t_2$) phase transition through a gap closing point at $t_1 = t_2$. An extension study on the topological aspects of this model is written in Sec. 2.5. This phase transition is protected by the chiral symmetry of the system, which we have discussed elaborately in subsec. 2.4.1. Note that in presence of finite onsite disorder this symmetry is explicitly broken. A variety of studies are focused on investigating the effect of disorder on the topological properties of the SSH model, where both the diagonal (onsite) and the off-diagonal (hopping) disorder are considered separately [141, 142, 143]. In particular, while the chiral symmetry of the SSH model is preserved in the case of finite hopping disorder, it is explicitly broken at any finite value of the onsite disorder strength. Therefore, in the latter case, the zero-energy edge modes of the clean system become energetic in the presence of any finite disorder. Efforts have been made to understand such interesting scenarios in the context of the nature of chirality [144], the interplay between long-range hopping and disorder [145], and also the possible existence of the mobility edge [146]. In Ref. [146] it is shown that the SSH model superimposed with a QP hopping disorder may yield a mobility edge in the spectrum.

We show that for both types of disorder, the system undergoes a localization transition as a function of λ exhibiting the SPME when $t_1 \neq t_2$. However, an

interesting scenario happens in the case of staggered disorder where the system returns back to a critical regime after the first localization transition hosting a second SPME at higher values of λ. This interesting and counter-intuitive result reveals the re-entrant behaviour of the localization transition and the SPME which we shall elaborately discuss in the following.

4.3 Results

We choose $\beta = (\sqrt{5} - 1)/2$, a Diophantine number [100] in our work and fix the intra-cell hopping, $t_1 = 1$ as the energy scale. For convenience, we define a quantity, namely δ defined by $\delta = t_2/t_1$ which controls the hopping dimerization in Eq. 4.1. The system size considered in our simulations is up to $L = 13530$, that is, $N = 6765$ unit cells. We explore the effects of uniform and staggered disorder in both the limits of dimerization in Eq. 4.1 such as $\delta < 1$ and $\delta > 1$. To analyze the physics of the model shown in Eq. 4.1, we rely on the inverse participation ratio (IPR) (see Eq. 1.36) and the normalized participation ratio (NPR) (see Eq. 1.40), which are the two most significant diagnostic tools to characterize the localization transition. Before proceeding with the staggered λ case we first highlight the physics associated with the case of uniform λ for comparison.

4.3.1 Uniform disorder

Here, we consider the system with a uniform disorder which is incorporated by choosing $\lambda_A = \lambda_B = \lambda$ in Eq. 4.1. In the limit of $\delta = 1$, Eq. 4.1 corresponds to the pure AA model which exhibits a localization transition without any SPME.

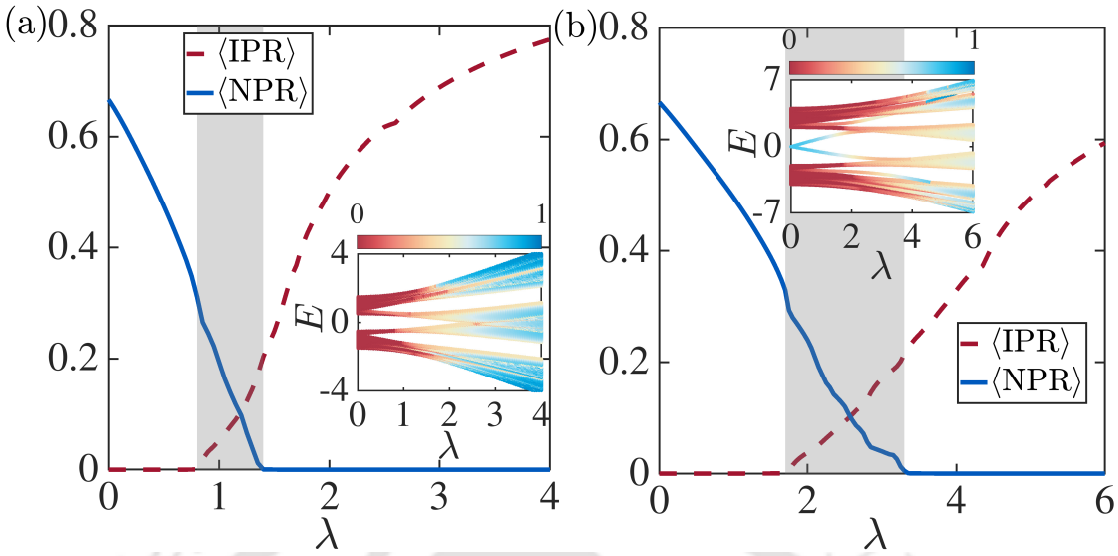

Figure 4.1: Figure shows the ⟨IPR⟩ (magenta) and ⟨NPR⟩ (black) are plotted as a function of λ for (a) $\delta = 0.5$ and (b) $\delta = 3$ for a system of size $L = 13530$. The shaded regions indicate the critical or the intermediate regimes. The color maps in the insets show the corresponding plots of IPR associated to all eigenmodes E with respect to λ and the color bars represent the values of IPR.

However, moving away from this limit, we show that the localization transition occurs through a critical regime hosting the SPME for both $\delta < 1$ and $\delta > 1$. To identify the localization transitions we plot the ⟨IPR⟩ and the ⟨NPR⟩ as a function of λ for the two exemplary points, namely, $\delta = 0.5$ and $\delta = 3$ in Fig. 4.1(a) and (b) respectively. Following Eq. 1.43, ⟨IPR⟩ and ⟨NPR⟩ denote the averages of the IPR and NPR computed by considering all the eigenstates for a particular value of λ. It can be seen that contrary to the simple AA model ($\delta = 1$), the plots for the ⟨IPR⟩ and the ⟨NPR⟩ do not sharply cross each other at the duality point $\lambda = 2$ [17] for both the values of δ. Rather they cross each other at very different values of λ and also exhibit a coexisting region where both the ⟨IPR⟩ and the ⟨NPR⟩ are finite (shaded regions). This signifies the presence of both the localized and the extended states for a range of λ ($0.7 < \lambda < 1.4$ when $\delta = 0.5$ and $1.6 < \lambda < 3.4$

when $\delta = 3$) which are the critical phases exhibiting the SPMEs. Clearly after the localization transition all the states remain localized as a function of λ.

The localization transition and the existence of the SPME can be easily inferred from the energy spectrum and the associated IPR of the individual states. We plot the IPR associated to the energy spectra, E corresponding to the Hamiltonian in Eq. 4.1 for $\delta = 0.5$ and 3 in the insets in Figs. 4.1(a) and (b) respectively. Here, the eigenenergies are color coded with the corresponding IPRs. Due to the dimerized nature of the model (Eq. 4.1), we get two distinct energy bands at $\lambda = 0$ and in this limit the energy levels are completely extended for both the trivial (Fig. 4.1(a)) and the topological (Fig. 4.1(b)) cases. As the value of λ increases, the gaps between the bands in both the dimerized limits tend to vanish beyond a critical λ. Clearly, in both the cases, the fully extended (blue) and the localized regions (red) are separated by a critical phase where both extended and localized states coexist for a range of values of λ which host a SPME. Quite expectedly, in Fig. 4.1(b), the appearance of the localized states at $\lambda = 0$ are the topological edge modes present in the middle of the gap. We shall discuss the fate of these edge modes later. Note that other minibands with some states in the gaps between them appear in the energy spectrum due to the quasiperiodic disorder which are irrelevant for the present analysis.

4.3.2 Staggered disorder

Now, we consider the system with a staggered disorder which is introduced by choosing $\lambda_A = -\lambda_B = \lambda$ in Eq. 4.1. Further, we discuss the role of staggered disorder on the localization transition. Following the analysis similar to the case

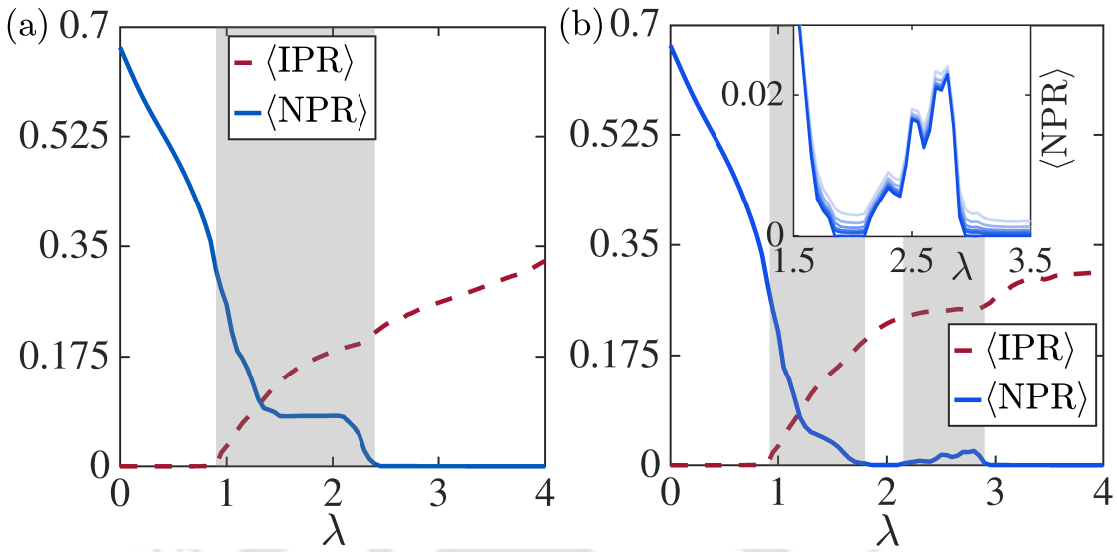

Figure 4.2: (a) and (b) show the ⟨IPR⟩ and the ⟨NPR⟩ for $\delta = 1.5$ and 2.2 respectively for the case of staggered disorder and $L = 13530$. The shaded regions represent the critical phases. (Inset) shows the ⟨NPR⟩ for $L = 1974,\ 3194,\ 5168,\ 8362,\ 13530$ and ∞ (light to deep blue).

of uniform disorder we compute the ⟨IPR⟩ and the ⟨NPR⟩ by moving away from the AA limit, i.e. $\delta = 1$. In this case also one expects a qualitatively similar localization transition as in the uniform disorder case with some quantitative difference. This is confirmed in our analysis which shows the extended to localization transition through a critical phase where both ⟨IPR⟩ and ⟨NPR⟩ are finite for a range of values of δ. As it is well known and already mentioned before, in quasiperiodic lattices exhibiting localization hosting the SPME, for the values of λ prior to (beyond) the critical phase, all the states of the system are extended (localized).

Once the system is in the localized phase, it remains localized as a function of the strength of the quasiperiodic potential, λ. As a result, one gets ⟨IPR⟩ $\neq 0$ and ⟨NPR⟩ $= 0$ for all values of λ after the critical regime. However, surprisingly in

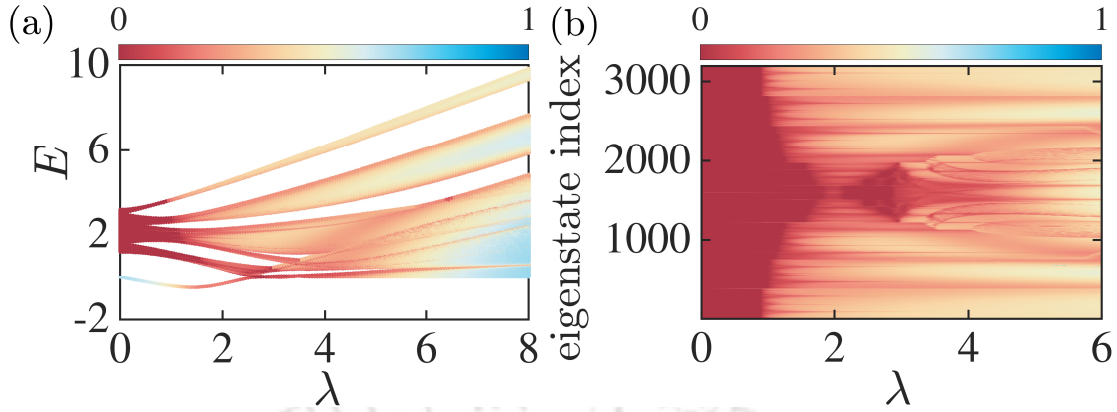

Figure 4.3: (a) The upper half of the energy eigenvalue spectrum superimposed with their respective IPR shows the extended, critical and localized states. (b)The IPR associated to the eigenstate indices as a function λ for $\delta = 2.2$ for a system of size $L = 3194$.

presence of the staggered disorder, we find that for some intermediate values of δ, the system undergoes two localization transitions through two critical phases as a function of λ. This re-entrant localization behaviour can be very well discerned by together analyzing $\langle$IPR$\rangle$ and $\langle$NPR$\rangle$. In Figs. 4.2(a) and (b) we show $\langle$IPR$\rangle$ and $\langle$NPR$\rangle$ corresponding to two different values of dimerization such as $\delta = 1.5$ and 2.2 respectively for $L = 13530$. Clearly for $\delta = 1.5$ (Fig. 4.2(a)), there is a transition to the localized phase through a critical region for the range of λ between $0.9 < \lambda < 2.5$. After the localization transition i.e. for $\lambda > 2.5$, all the states are localized. On the other hand, for $\delta = 2.2$ (Fig. 4.2(b)), there exists two critical regions in the range $0.9 < \lambda < 1.8$ and $2.3 < \lambda < 2.9$ where both $\langle$IPR$\rangle$ and $\langle$NPR$\rangle$ are finite. In the region between the two critical phases and again beyond the second critical phase, the system is fully localized. This indicates that the system also hosts two SPMEs as a function of λ. Note that the extent of the second critical region occurs for a small range of λ . In order to rule out any finite size effects, we perform finite size extrapolation of the $\langle$IPR$\rangle$ and $\langle$NPR$\rangle$ considering

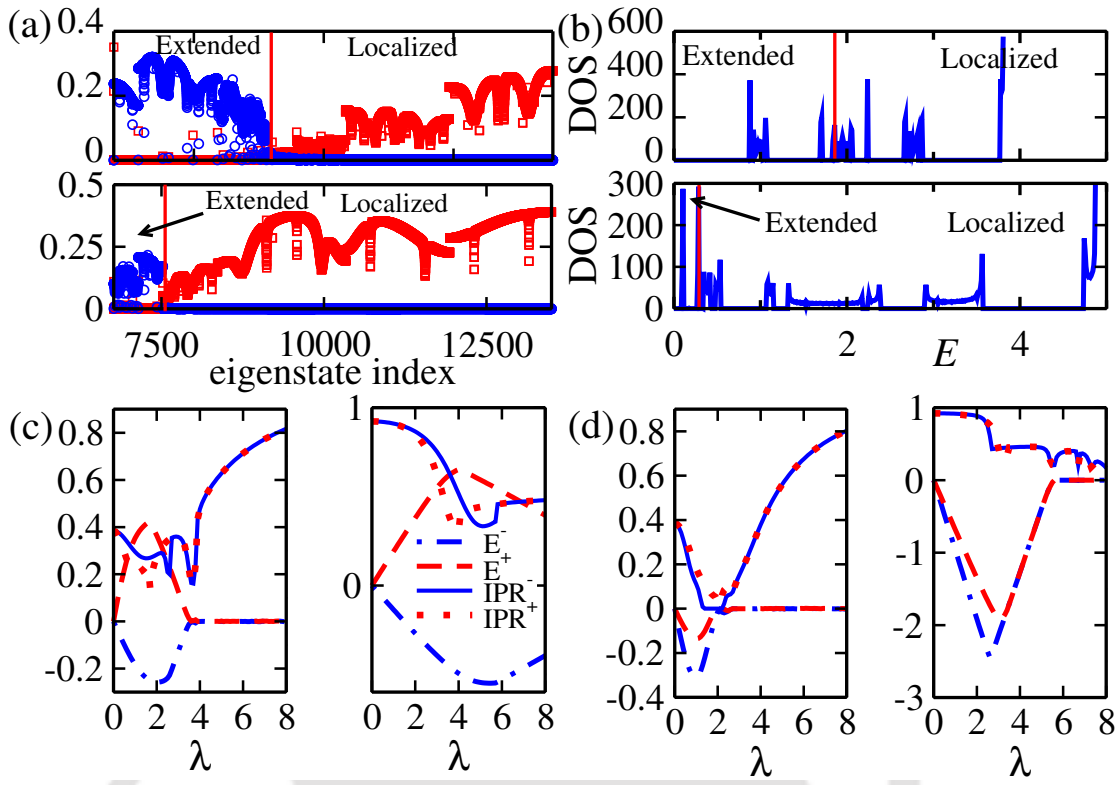

Figure 4.4: (a)Shows the IPR (red squares) and NPR (blue circles) of different eigenstates for $\delta = 2.2$ and $\lambda = 1.2$ (upper panel) and $\lambda = 2.7$ (lower panel). The states with finite IPR in the extended regime are the emerging edge modes in the fractal gaps. (b) Shows the DOS for $\delta = 2.2$ and $\lambda = 1.2$ (upper panel) and $\lambda = 2.7$ (lower panel). The vertical lines separate the extended and localized regions. (c) and (d) show the edge states and the corresponding IPRs for uniform and staggered disorder respectively for $\delta = 1.5$ (left panel) and $\delta = 5$ (right panel). E^- (blue dot-dashed) and E^+ (red dashed) corresponding to the two edge states along with their IPR i.e. IPR$^-$(blue solid) and IPR$^+$ (red dotted).

data for different system sizes such as $L = 1974, 3194, 5168, 8362, 13530$. The inset of Fig. 4.2(b) shows the $\langle$NPR$\rangle$ data for various system sizes including the one at $L \to \infty$ for $\delta = 2.2$, which we shall discuss in details in the later section. This clearly indicates the stability of the second critical region.

This re-entrant localization feature is clearly visible in the energy spectrum

encoded with the corresponding IPR as shown in the Fig. 4.3(a). For clarity we depict only the upper band of the spectrum which shows a series of the extended-critical-localized-critical-localized regions as a function of λ. This feature is also seen by plotting the IPR of the individual eigenstates as shown in Fig. 4.3(b). The deep-red patches appearing in Fig. 4.3(a) and (b) for $2.2 < \lambda < 2.9$ are due to the presence of the second critical region and the second SPME. We further confirm the existence of the SPME by plotting the IPR and the NPR for the individual eigenstates of the system in the critical regime. Fig. 4.4(a), shows the IPR and NPR for all the eigenmodes for $\delta = 2.2$ at $\lambda = 1.2$ and 2.7 in the upper and lower panels respectively. The plots show a clear distinction between the extended states (finite NPR) from the localized states (finite IPR) of the spectrum. Similar signature is also seen in the density of states (DOS) by analyzing it with the IPR of the individual states indicating the existence of the mobility edge as shown in Fig. 4.4(b) (see figure caption for detail). We also find that the re-entrant physics is also seen in the $\delta < 1$ limit.

4.3.3 Phase diagram

Finally, we present the key results in the form of a phase diagram as displayed in Fig. 4.5(b) for the case of staggered disorder in the δ - λ plane. To this end, we calculate a quantity, η which is introduced in [102, 41], given by,

$$\eta = \log_{10}[\langle \text{IPR} \rangle \times \langle \text{NPR} \rangle] \tag{4.2}$$

which helps us to distinguish between the critical phase from the extended and the localized phases. In order to understand better, we start with a limiting case. If the system hosts any of the phases, for example, an extended or a localized

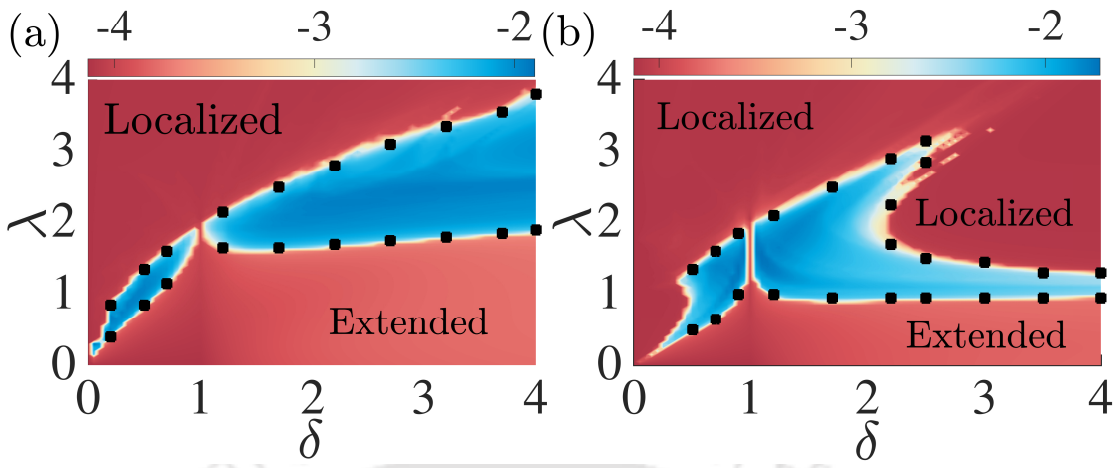

Figure 4.5: Phase diagrams in δ and λ plane for (a) uniform disorder and (b) staggered disordered cases. The filled black squares are the data points obtained by examining the IPR and NPR plots. (See text for details). The color bar on the top stands for the values of η.

phase, then η value survives due to either of the average values of IPR or NPR, resulting in the condition $\eta < -\log_{10}(L)$. Subsequently, the critical phase starts with the mixture of eigenstates for $\eta \geq -\log_{10}(L)$. On the other hand, since IPR and NPR are inversely related, thus, the system will exhibit its other limit for the critical phase when there are an equal number of the extended and the localized states present in the spectrum, that is, $\langle \text{IPR} \rangle = \langle \text{NPR} \rangle$.

The phase diagrams is obtained by computing the quantity η. The presence of the critical region (blue region bounded by the symbols) is clearly distinguished from the fully extended or the fully localized regions (red regions) in the phase diagram. Note that the critical regions are separated by the a narrow passage at $\delta = 1$ (AA model), where a sharp localization transition occurs. It can be seen that for a range of δ one encounters two critical regimes with increase in λ which is the key finding of our analysis. However, this re-entrant feature does

not appear in the case of uniform disorder (compare Fig. 4.5(a)). We complement the above findings by directly locating the boundaries (filled squares) of the critical region by examining the values of ⟨IPR⟩ and ⟨NPR⟩ in the theormodynamic limit. This non-trivial feature of the re-entrant localization transition and the SPME can be attributed to the competition between the hopping dimerization and the staggered disorder that renders extended nature to some of the low energy localized states. The detailed analysis the above requires further investigation.

It is worth mentioning that the re-entrant localization phenomena and the mobility edge occurs in both the limits of the dimerization (see Fig. 4.5(b)). Hence, an important conclusion can be drawn at this point is that the underlying topological properties has no role in establishing the re-entrant localization transition.

4.3.4 Edge modes

Having analyzed the physics of the bulk spectrum, we discuss about the fate of the topological zero energy edge modes as a function of the disorder strength. We note that the initially localized zero modes (at $\lambda = 0$) become energetic and finally hybridize into the bulk bands with increase in λ for both uniform and staggered disorder cases as already shown in Fig. 4.1(b) and Fig. 4.3(a) respectively. To explicitly understand the behavior of these modes, we separately plot the edge modes as a function of λ in Fig. 4.4 along with their IPR. We consider two different values of δ, namely, $\delta = 1.5$ and $\delta = 5$ which represent weak and strong dimerization limits pertaining to the topological regime. As mentioned

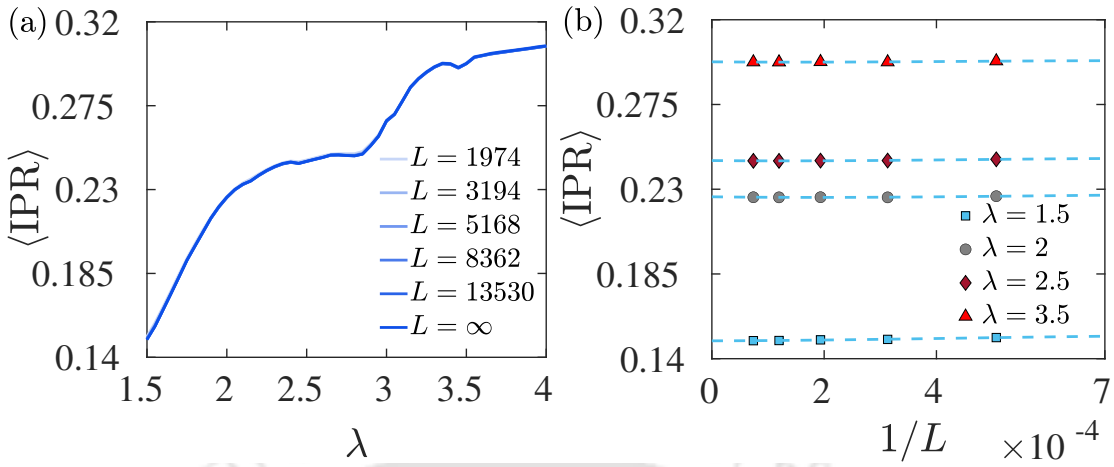

Figure 4.6: (a) The ⟨IPR⟩ for all the lengths including the one at the thermodynamic limit are shown which show negligible finite size effects. (b) Finite size extrapolation of the ⟨IPR⟩ is shown for some selected values of λ. It can be seen that the ⟨IPR⟩ remains finite throughout the region of interest.

earlier, owing to the breaking of the chiral symmetry induced by the quasiperiodic potential, both the edge modes, namely, the particle mode (E^+ shown by a dashed red line) and the hole mode (E^- shown by a dot-dashed blue line) asymmetrically separate out from each other towards the opposite bands as λ increases (Fig. 4.4(c)) for the case of uniform potential. However, in the case of the staggered disorder, both the edge modes move differently towards the lower band (Figs. 4.4(d)) [147]. Eventually for all the cases, beyond certain critical values of λ, E^+ and E^- tend to merge with each other. We also plot the corresponding IPR for both the modes as IPR^+ (dotted red) and IPR^- (solid blue). It can be seen that in all the four cases the IPR initially decrease and then increase as a function of λ. In the case of weak dimerization ($\delta = 1.5$), initially the states are not fully localized. As the value of λ increases, the states tend to become delocalized and then become fully localized. On the other hand, in the case of strong dimerization, the states which are fully localized (IPR $\sim$ 1) at the begin-

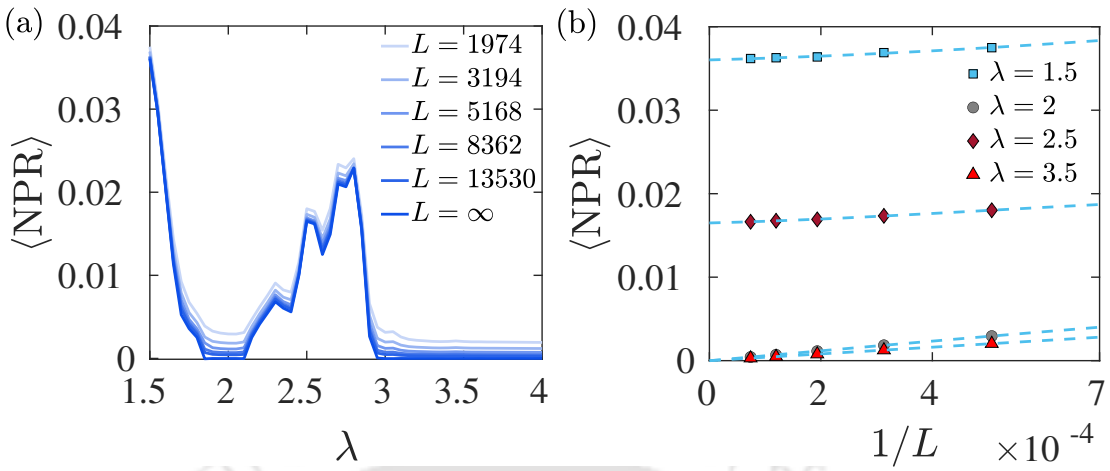

Figure 4.7: (a) The ⟨NPR⟩ for all the lengths including the one at the thermodynamic limit clearly shows the re-entrant behaviour. (b) Finite size extrapolation of the ⟨NPR⟩ is shown for some selected values of λ.

ning (small λ) tend to be delocalized and then become localized again. This re-entrant localization of the edge states is slow as a function of λ in the case for larger δ.

4.3.5 Finite-size scaling

Here we perform a finite-size scaling analysis to establish our observations gained from the above section. In order to do that, we plot the values of ⟨IPR⟩ and ⟨NPR⟩ as a function of the potential strength λ for various system sizes such as $L = 1974, 3194, 5168, 8362$ and 13530 corresponding to $\delta = 2.2$ (reentrant localization regime) in Fig. 4.6 (a) and Fig. 4.7 (a), respectively. In addition, we compute the behavior of them in the thermodynamic limit, that is $L \to \infty$. Consequently, we observe the finite-size effects by light blue curves to the deep blue curves corresponding to ⟨NPR⟩ plot in Fig. 4.7 (a). Thus it clearly indicates the

existence of a second critical region even in the large L limit, and hence signal a re-entrant behavior of the localization transition. However, the average IPR, namely $\langle \text{IPR} \rangle$ tells a different story. It is depicted that all the curves corresponding to different sizes merge into one another for $\langle \text{IPR} \rangle$ in Fig. 4.6 (a).

Further, in order to compute the nature of $\langle \text{IPR} \rangle$ and $\langle \text{NPR} \rangle$ in the thermodynamic limit, we study the scaling analysis in Fig. 4.6 (b) and Fig. 4.7 (b). Thus we plot both the $\langle \text{IPR} \rangle$ and $\langle \text{NPR} \rangle$ as a function of $1/L$ for some representative values of λ, such as $\lambda = 1.5,\ 2,\ 2.5$, and 3.5. While Fig. 4.6 (b) illustrates finite values corresponding to all the four values of λ, Fig. 4.7 (b) depicts the re-entrant behavior. Thus $\langle \text{NPR} \rangle$ is used as an appropriate observable to identify the re-entrant behavior. Further, it is interesting to notice that at $\lambda = 1.5$, the $\langle \text{NPR} \rangle$ value is finite, thereby indicating an extended nature of the eigenstates. By increasing the value of λ, that is $\lambda = 2$, $\langle \text{NPR} \rangle \to 0$ at $L \to \infty$, exhibiting the first localization transition. The finite-size extrapolation is done via fitting a cubic polynomial to the data points. Further, at $\lambda = 2.5$, $\langle \text{NPR} \rangle$ again yields a finite value, thereby undergoing a transition from the localized to the extended phase. Finally, we observe another localization transition by approaching $\langle \text{NPR} \rangle \to 0$ at $\lambda = 3.5$ and $L \to \infty$.

4.4 Conclusions

We have studied the localization transition in a dimerized lattice with staggered quasiperiodic disorder. We show that the system undergoes a re-entrant localization transition as a function of disorder strength for a range of values of dimerization. The re-entrant localization occurs in both the regimes of dimer-

ization and each localization transition is associated with the SPME. We confirm this finding by examining the participation ratios, the single particle spectrum and the behavior of the individual eigenstates and present a phase diagram depicting all the above findings. For completeness we also analyse the phase diagram in the case of uniform disorder which shows the usual localization transition and the SPME. Further we discuss the fate of the zero energy edge modes as a function of disorder strength which were initially localized in the absence of any disorder due to the topological nature of the model. At the end, a finite-size scaling analysis is done in order to support our observations.

The re-entrant feature may reveal interesting physics in transport and dynamical properties of quantum particles. An immediate extension could be to study the stability of this re-entrant phenomenon in the context of many-body localization. Due to the phenomenal experimental progress in systems of ultracold atoms in optical lattices to simulate dimerized latticed [148, 149], quasiperiodic systems [150, 45] and the recent experiment on disorder induced topological phase transition using ^{171}Yb [151], our findings can in principle be simulated in the state-of-the art quantum gas experiments.

CHAPTER 5

CRITICAL STATE PROPERTIES OF THE REENTRANT LOCALIZATION TRANSITION

5.1 Introduction

In the last chapter, we have observed a striking manifestation of a re-entrant localization transition in a dimerized tight-binding chain in presence of a quasiperiodic potential. It was shown such a system undergoes two localization transitions at the single particle level. In other words, for some specific dimerization strengths and as a function of the onsite potential, the system first demonstrates a localization transition where all the single particle states get localized. Further increase in the potential strength turns some of the localized states extended, and eventually the system undergoes another localization transition at a larger potential strength where all the single particle states get localized for the second time. Both these localization transitions are found to occur through two intermediate regions hosting the mobility edges (MEs) resulting in four critical points as a function of the quasiperiodic potential strength. While the detailed phase diagram depicting the re-entrant localization transition associated to this model has been discussed in sec. 4.3.3, a thorough understanding of the phase transitions can be unveiled via a quantitative analysis of the critical properties which is relevant and of topical interest.

In this chapter, we study the critical properties of the re-entrant localization transition described above. By using appropriate critical state analysis, which is explained in sec. 2.3.3, we explore the critical points associated to different transitions, that is, extended → intermediate → localized → intermediate → lo-

calized transition as a function of the strength of the quasiperiodic potential. While from our analysis as detailed in this chapter, we are able to obtain the critical points, critical exponents, and scaling behaviour associated with the first localization transition, that is the extended → intermediate → localized → intermediate transitions, however, at the second localization transition, the scaling behaviour is not well captured. We further analyse the eigenspectra near the localization transitions and find the existence of multifractal states and identify the critical regimes.

In the following, we describe the model Hamiltonian sec. 5.2 to make the subsequent discussion self contained. Hence we describe our results on the phase diagram in sec. 5.3.1, followed by the multifractal analysis (sec. 5.3.2), critical state analysis (sec. 5.3.3) and compute the Hausdorff dimension (sec. 5.3.4). Finally we conclude our results in (sec. 5.4).

5.2 Model

The Hamiltonian with hopping dimerization and staggered quasiperiodic potential on a one-dimensional chain is written as [Follow Eq. 4.1],

$$\begin{aligned} H_{\mathrm{DIM}} = & -t_1 \sum_{n=1}^{N} (\hat{c}^{\dagger}_{n,B} \hat{c}_{n,A} + \mathrm{H.c.}) \\ & -t_2 \sum_{n=1}^{N-1} (\hat{c}^{\dagger}_{n+1,A} \hat{c}_{n,B} + \mathrm{H.c.}) \\ & + \sum_{n=1}^{N} \lambda_A \hat{n}_{n,A} \cos[2\pi\beta(2n-1) + \phi] \\ & + \sum_{n=1}^{N} \lambda_B \hat{n}_{n,B} \cos[2\pi\beta(2n) + \phi] \end{aligned} \tag{5.1}$$

where $L = 2N$ with N being the number of unit cells that are denoted by the index n and L is the total system size. Here, a unit cell comprises of two sublattice sites, namely, A and B where the corresponding creation (annihilation) operators are denoted by $\hat{c}^{\dagger}_{n,A}$ ($\hat{c}_{n,A}$) and $\hat{c}^{\dagger}_{n,B}$ ($\hat{c}_{n,B}$) respectively. $\hat{n}_{n,A}$ and $\hat{n}_{n,B}$ are the number operators at the two sublattice sites. The inter-cell hopping between the two sublattices is denoted by t_2 and t_1 refers to the intra-cell hopping. The hopping dimerization is introduced by defining $\delta = t_2/t_1$ and making $\delta \neq 1$. We have taken t_1 as the unit of energy throughout the study. The on-site quasiperiodic potential at the sublattice site A (B) is given by λ_A (λ_B). The quasiperiodicity is achieved by considering an irrational β. In particular, we take it as the inverse of the golden mean, namely $\beta = \frac{(\sqrt{5}-1)}{2}$ [23]. ϕ denotes the phase difference between the lattices that form the quasiperiodic lattice. In our studies, we consider very large system sizes L up to a maximum of 35422 sites for which ϕ can be set to zero without any loss of generality.

5.3 Results

5.3.1 Phase diagram

The localization properties of the model shown in Eq. 5.1 has been discussed in detail in chapter. 4 [140]. It has been observed that the system exhibits a re-entrant localization transition in the limit of staggered disorder i.e. $\lambda_A = -\lambda_B = \lambda$, which has been depicted as a phase diagram in the δ - λ plane in Fig. 5.1 (see Ref. 4.3.3 for details). Note that the phase diagram shown in Fig. 5.1(a) has been obtained by utilizing the behaviour of the average participation ratios, such as

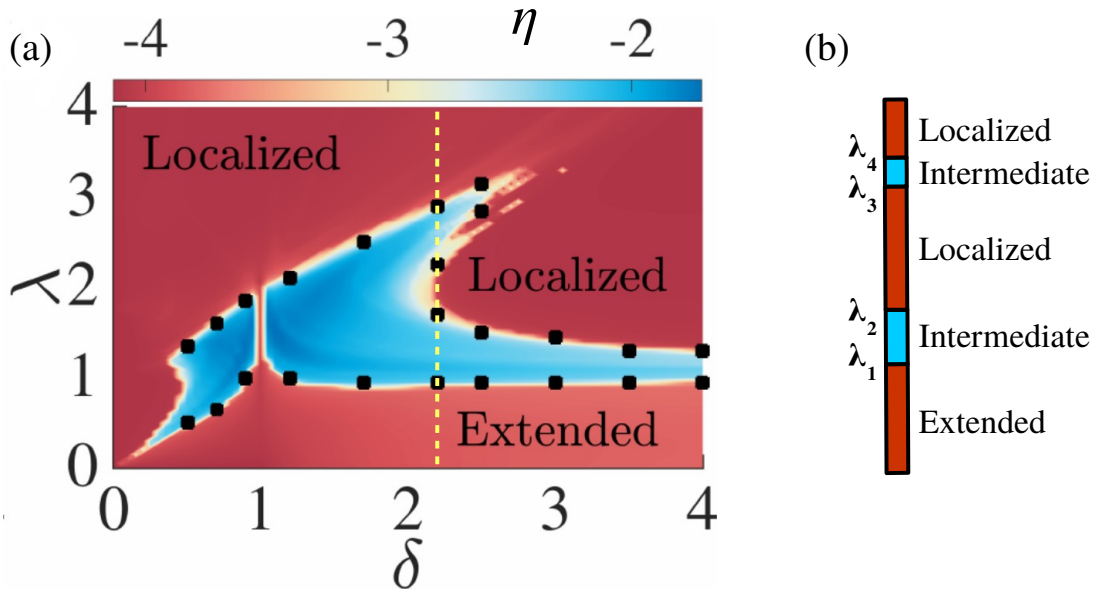

Figure 5.1: Phase diagram is plotted as a function of hopping dimerization δ and disorder strength λ in (a). In (b), a schematic picture of the series of transitions is shown for $\delta = 2.2$ (mark by the dashed line in (a)).

the average inverse participation ratios ⟨IPR⟩ and the normalized participation ratio ⟨NPR⟩ (see Eq. 1.43), respectively as a function of λ. Here, ⟨IPR⟩ and ⟨NPR⟩ are calculated by taking the average over all the eigenstates corresponding to the Hamiltonian shown in Eq. 5.1. The different phases in the phase diagram are computed by using a quantity η, which is described in Eq. 4.2 in chapter. 4 [41].

In the phase diagram of Fig. 5.1(a), the red regions correspond to the extended or localized phases and the central blue region bounded by the dark symbols is the intermediate phase. It can be seen from the phase diagram that for a range of values of δ, the system undergoes two localization transitions as a function of λ indicating the re-entrant localization transition. Although, the re-entrant localization is feasible in both the regimes of hopping dimerization

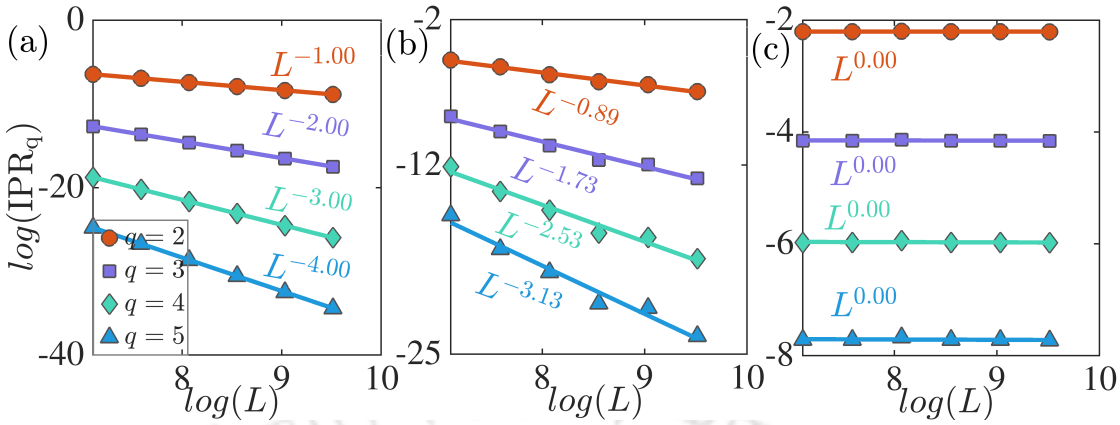

Figure 5.2: The generalized IPR is plotted as a function of different system sizes L and corresponding to different moments of the intensity q. The slope of the curves are characterized by the mass exponent τ_q. We have shown three distinguishing behavior of τ_q by considering the potential strength λ in the extended, multifractal and localized regions in (a), (b) and (c) respectively. We have considered $\lambda = 0.5$ and eigenstate index $(m/L) = 0.5$ in (a) , $\lambda = 0.903$ (first critical point) and eigenstate index $(m/L) = 0.1$ in (b), and $\lambda = 4$ and eigenstate index $(m/L) = 0.5$ in (c). For all the cases, we have taken $\delta = 2.2$.

corresponding to $\delta < 1$ and $\delta > 1$, for our discussion we restrict ourselves in the regime of $\delta > 1$ for concreteness. For our analysis, we explore the critical properties for a cut through the phase diagram along the $y-$ axis at $\delta = 2.2$ (dashed yellow line in Fig. 5.1(a)). As λ is increased, the system as a whole undergoes two localization transitions through two intermediate phases exhibiting a series of transitions from extended - intermediate - localized - intermediate - localized phases occurring at four critical points, λ_1, λ_2, λ_3 and λ_4 respectively as schematically depicted in Fig. 5.1(b) [152]. In the following our focus is to study the fractal nature of the eigenstates and eigenspectra across these transitions and determine the transition points through a finite-size scaling analysis.

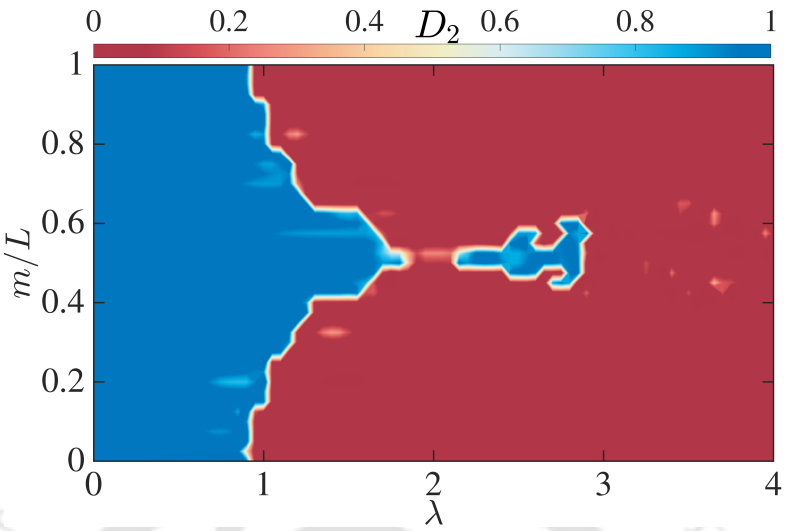

Figure 5.3: The values of D_2 as a function of λ and eigenstate index (m/L) are plotted for $\delta = 2.2$.

5.3.2 Multifractal analysis

As already discussed in the previous section, the two localization transitions in this case occur through two intermediate regions. In analogy with the direct localization transition in the case of the AA model and other models where the localization transition occurs through an intermediate region, we expect existence of multifractal eigenstates in the intermediate phases. Thus, to explore deeper into the nature of the states in different regions we perform a multifractal analysis [24, 22] of the eigenstates and calculate the associated fractal dimensions to arrive at an intuitive picture for the critical regions.

In our analysis, by following Eq. (2.5), we first obtain the correlation dimension, denoted by D_2. Hence, it can be calculated as the slope of the $log(\text{IPR}_2)$ versus $log(L)$ plot corresponding to different states as shown in Fig. 5.2 (red circles). Furthermore, in order to gain insights about the variation of D_2 over the entire spectrum, we plot D_2 as a function of eigenstate index and λ at $\delta = 2.2$ in Fig. 5.3

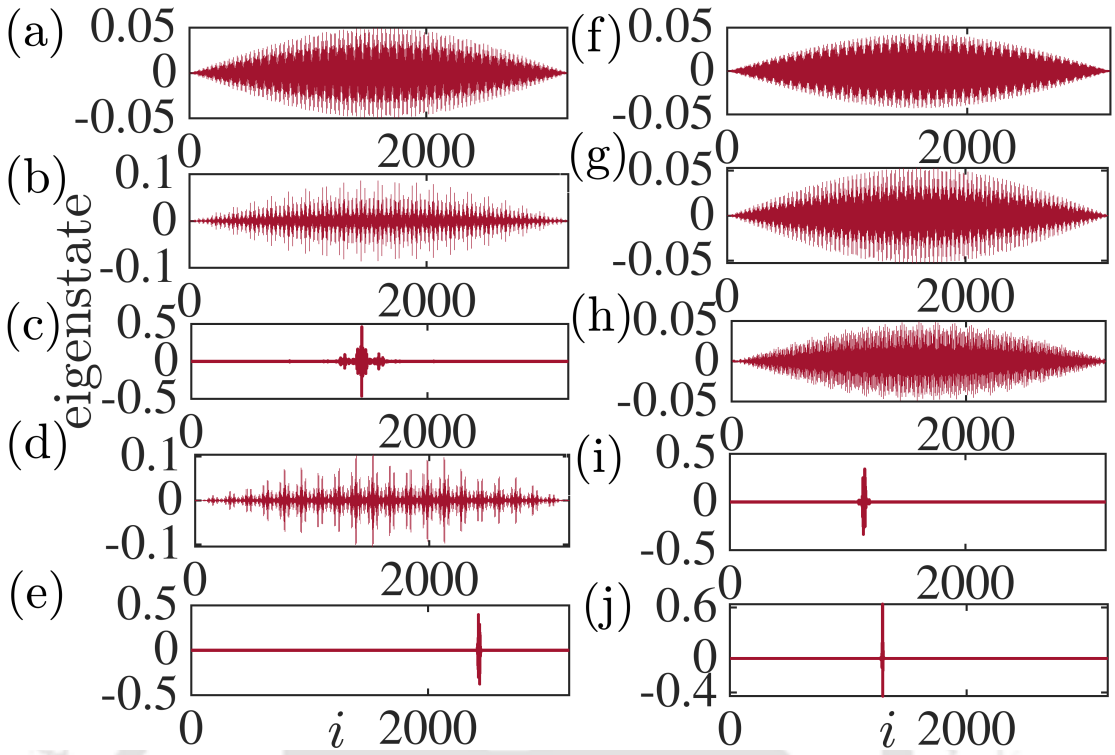

Figure 5.4: (a-e) of the figure show the eigenstates as a function of site index i corresponding to $\lambda = 1.0,\ 1.5,\ 2.0,\ 2.5,$ and 3.5 for the eigenstate index ($m/L = 0.5$) and $\delta = 2.2$. As a comparison, (f-j) of the figure represent the eigenstates behaviour corresponding to $\delta = 1.5$ and $m/L = 0.5$. The system size taken for the calculation is $L = 3194$.

which clearly shows the existence of the extended, the localized and the multifractal states. While the expected re-entrant feature can be seen from Fig. 5.3, a clear understanding of this can be achieved from the structure of the eigenstates. In this regard, we plot the eigenstates for different values of λ, namely, $\lambda = 1.0,\ 1.5,\ 2.0,\ 2.5,$ and 3.5 for a particular eigenstate with index $m/L = 0.5$ as a function of the site index i in Fig. 5.4 (a-e). It is observed that the wavefunction at $\lambda = 1.0$ spreads over the entire lattice uniformly, indicating its extended nature. At $\lambda = 1.5$, the behavior is more like a fractal state, where a large fluctuation in the probability amplitude can be seen. A localized state is observed following

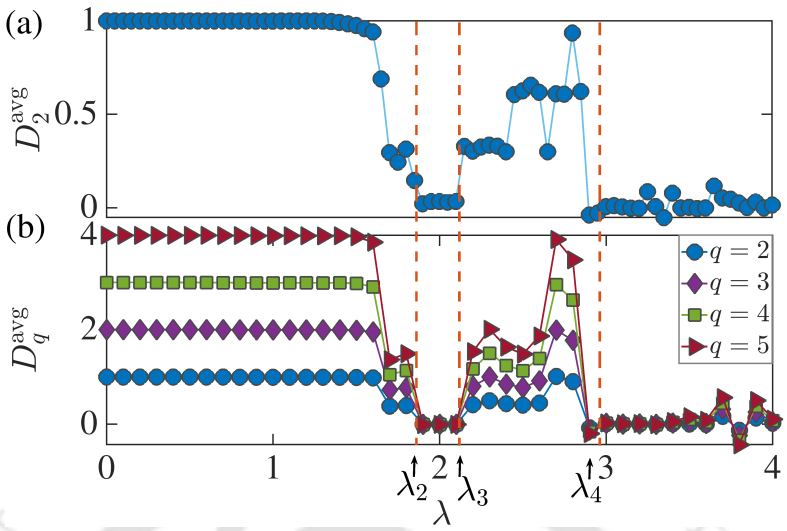

Figure 5.5: D_2^{avg} and D_q^{avg} are plotted as a function of λ in (a) and (b) respectively for $\delta = 2.2$.

the system characteristics at $\lambda = 2.0$. At $\lambda = 2.5$, the fractal nature reappears, and finally as expected, the wavefunction becomes completely localized at $\lambda = 3.5$. As a further check, we have plotted the eigenstates corresponding to the identical values of λ which are $\lambda = 1.0,\ 1.5,\ 2.0,\ 2.5,$ and 3.5 for another dimerization strength $\delta = 1.5$ as function of site index i in Fig. 5.4 (f-j) where the re-entrant behaviour is absent.

To complement the above analysis to distinguish the nature of the states, we compute the average values of D_2 over the eigenstates. In Fig. 5.5(a), we plot D_2^{avg} as a function of λ, where the extended and localized phases are characterized by $D_2^{avg} = 1$ and 0 respectively. Whereas, $0 < D_2^{avg} < 1$ implies the presence of the states that are multifractal in nature. The average value of D_2 is calculated by considering some of the states from the middle of the spectrum. In addition to that, we also examine the variation of the exponents by considering different values of $q > 2$ ($q = 3,\ 4,\ 5$) that correspond to the higher moments of the eigenstates. We obtain signatures which exactly match with the nature of the

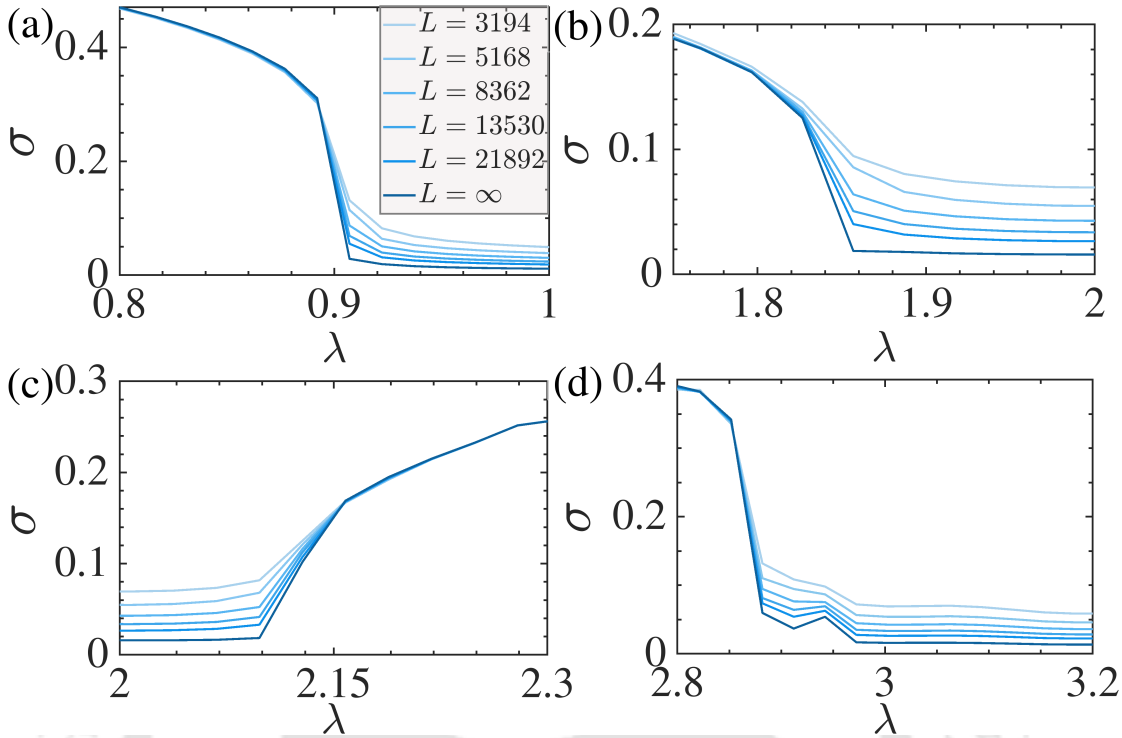

Figure 5.6: The order parameter σ is plotted as a function of λ corresponding to four different critical transition points λ_1, λ_2, λ_3, and λ_4. We consider the states within a narrow band with indices (m/L) = [0 to 0.05], [0.45 to 0.5], [0.45 to 0.5] and [0.45 to 0.5] for the calculation of σ in (a), (b), (c), and (d) respectively. The color gradient in increasing order indicate different system sizes from small to large. The curve with deep blue color is obtained by using finite-size extrapolation.

extended, the multifractal, and the localized states of the spectrum as shown in Fig. 5.2(a-c) respectively. A clear understanding of these features can also be achieved by plotting D_q^{avg} for the entire range of λ. In Fig. 5.5(b), we plot D_q^{avg} as a function of λ for $q = 2,\ 3,\ 4$ and 5. The q dependence of D_q^{avg} indicates the presence of multifractal states. In Fig. 5.5, different transitions are marked by the vertical dashed lines.

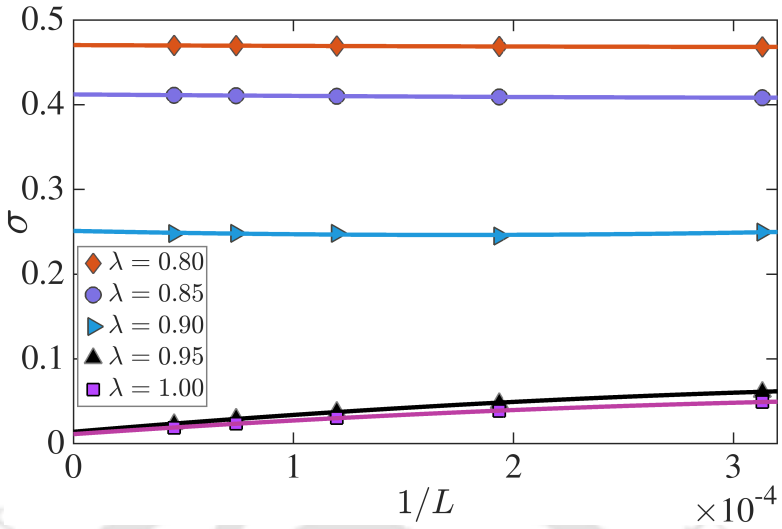

Figure 5.7: Figure shows the finite-size scaling analysis for several values of λ. The system sizes are L = 3194, 5168, 8362, 13530, and 21892..

5.3.3 Critical state analysis

In this section, we follow the critical state analysis formalism discussed in sec. 2.3.3. Subsequently, we establish the transition points by analysing the behaviour of the order parameter σ which is directly related to the NPR of the eigenstates corresponding to the Hamiltonian Eq. 5.1. From the definition, σ for different lengths should approach zero at the localization transition. Therefore, it will be possible to estimate all the critical points by using the finite-size extrapolation of σ. For this purpose, we compute σ by considering the eigenstates in a narrow band near the approximate transition boundaries. The choice of a narrow band is due to the presence of the ME for which the transition occurs at different critical λ for different states. We plot σ for different system sizes, namely, L = 3194, 5168, 8362, 13530 and 21892 as a function of λ in Fig. 5.6(a-d) across the transition points λ_1, λ_2, λ_3 and λ_4 respectively. A finite-size extrapolation reveals that for all the cases, σ in the limit of $L \to \infty$ falls to a minimum after

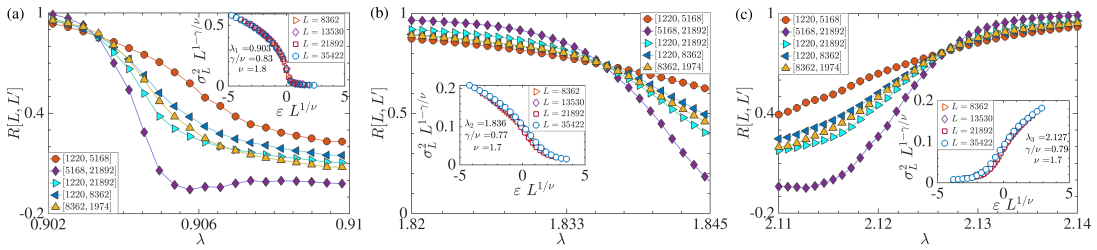

Figure 5.8: Figure shows the plot of $R\,[L, L']$ in the vicinity of the first critical quasiperiodic potential strength λ_1 in (a), the second critical quasiperiodic potential strength λ_2 in (b) , and third critical quasiperiodic potential strength λ_3 in (c) corresponding to $\delta = 2.2$. The insets show the data collapse with the σ^2 data in the vicinity of the first, second and third critical points. Good data collapse is observed for all the transition points. The existence of single universal scaling functions can easily be inferred from the data collapse. We have done the calculations by taking an average over the states in the band with indices $m/L =$ [0 to 0.05] for the first critical point and the states in the band with indices $m/L =$ [0.45 to 0.5] for the second and third critical points of the energy spectrum for the study.

a critical λ for different transitions. As an example we have shown a finite-size scaling analysis of σ corresponding to several values of $\lambda = 0.8,\ 0.85,\ 0.9,\ 0.95,$ and 1.0 across the first critical point in Fig. 5.7. The extrapolated values of σ tending to zero for larger values of λ clearly indicate a localization transition. This analysis defines the relevant range of λ for our exploration of the critical properties. Once the limits of λ around the critical transition points are identified we use them to calculate the function $R\,[L, L']$ (see Eq. (2.26)).

We first focus on the first localization transition which involves two critical points, such as λ_1 and λ_2 corresponding to the extended-intermediate and intermediate - localized transitions. Similar to the case of σ, for our analysis, to compute the function $R\,[L, L']$ we use the eigenstates corresponding to a narrow band of the spectrum. We plot $R\,[L, L']$ as a function of λ for both the transitions around λ_1 and λ_2 in Figs. 5.8(a) and (b) respectively. The crossing of all

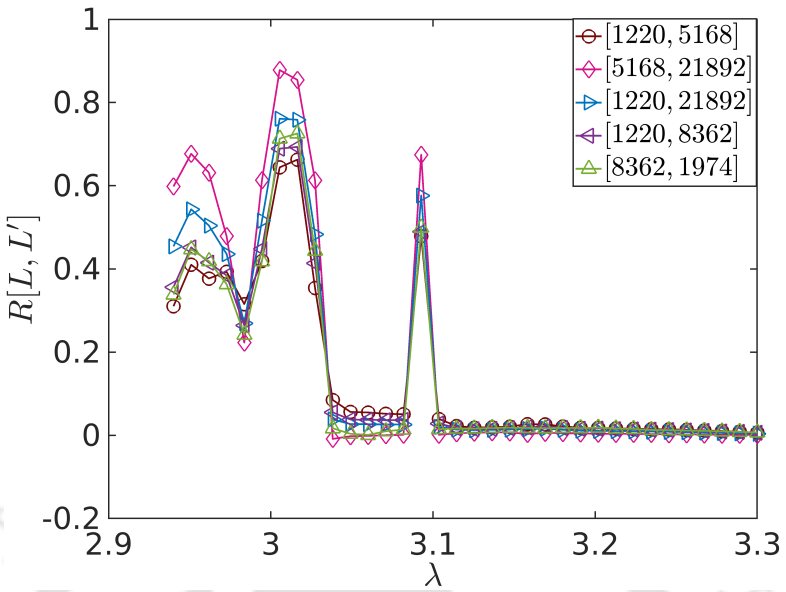

Figure 5.9: The functions $R\,[L, L']$ are plotted as a function of λ in the vicinity of the fourth critical point λ_4 at $\delta = 2.2$. We have done the calculations by taking an average over the states in the band with indices m/L = [0.45 to 0.5] of the energy spectrum for the study.

the curves at a single point in both the figures (Fig. 5.8(a) and (b)) allows to obtain the critical points as $\lambda_1 = 0.903$ and $\lambda_2 = 1.836$. As already mentioned in Sec. 2.3.3, following Eq. 2.30, curves of $\sigma^2 L^{1-\gamma/\nu}$ versus $\varepsilon L^{1/\nu}$ for different system sizes, $L = 8362,\ 13530,\ 21892$ and 35422 collapse with the estimated critical strength $\lambda_1 = 0.903$. A perfect data collapse is obtained by considering $\gamma/\nu = 0.83 \pm 0.05$ and $\nu = 1.8$ for $\lambda_1 = 0.903$ as shown in the inset of Fig. 5.8(a). Similarly, for the second critical point ($\lambda_2 = 1.836$), a perfect data collapse is obtained by setting $\gamma/\nu = 0.77 \pm 0.04$ and $\nu = 1.7$ (inset of Fig. 5.8(b)). Note that the γ/ν considered for the data collapse matches fairly well with the ordinate corresponding to the points of intersection of $R\,[L, L']$ as a function of λ in Figs. 5.8(a) and (b).

We now turn our focus on to the second localization transition through the

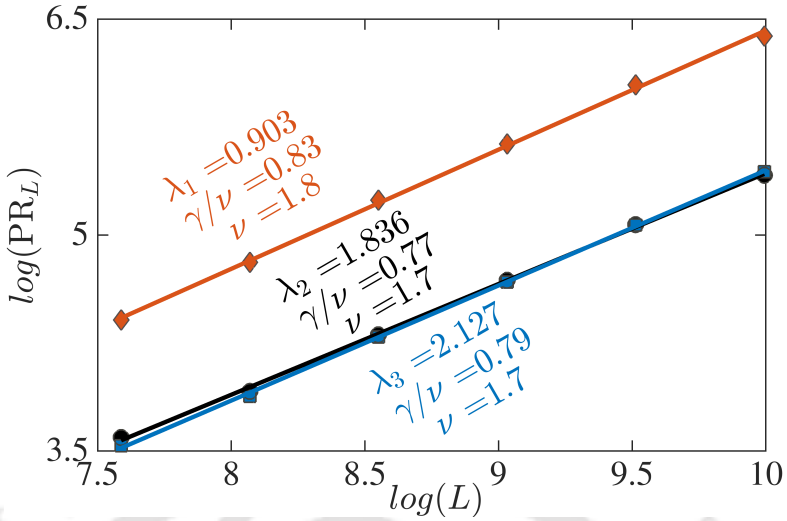

Figure 5.10: The exponent ratio γ/ν is calculated via plotting the $log(PR_L)$ as a function of $log(L)$ for different system sizes of L = 1974, 3194, 5168, 8362, 13530, 21892 corresponding to three different critical points such as λ_1, λ_2, and λ_3.

second critical region as depicted in Fig. 5.1. This involves two transitions, namely, localized-intermediate and intermediate - localized transitions at the critical points λ_3 and λ_4 respectively. Following a similar scaling hypothesis as above, for the localized - intermediate transition, we obtain the crossing of R $[L, L']$ data at a single point as depicted in Fig. 5.8 (c) resulting in a value of $\lambda_3 = 2.127$. Further, by using the value of λ_3, a perfect data collapse is achieved in the $\sigma^2 L^{1-\gamma/\nu}$ versus $\varepsilon L^{1/\nu}$ plot by setting $\gamma/\nu = 0.79 \pm 0.03$ and $\nu = 1.7$ as shown in the inset of Fig. 5.8 (c). This suggests that the two transitions occurring at λ_2 and λ_3 corresponding to the transitions to and from the first localised phase (intermediate - localized and localized - intermediate) belong to the same universality class.

It is now expected that the transition to the second localized phase i.e. the fourth transition occuring at λ_4 falls under the same universality class as that of the second and third transitions observed at λ_2 and λ_3. However, in our scal-

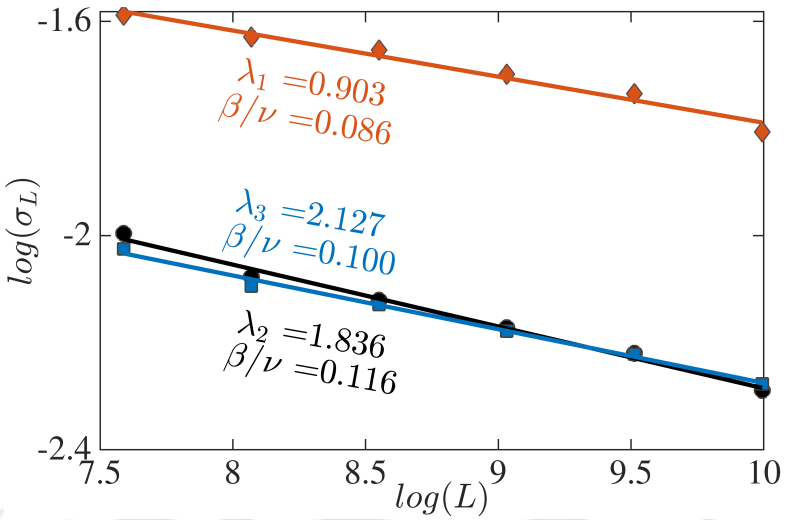

Figure 5.11: The exponent ratio, β/ν is calculated via plotting the order parameter, σ_L as a function of different system lengths (L) corresponding to three different critical potential strengths, namely, λ_1, λ_2, and λ_3.

ing analysis, we find an anomalous scaling behaviour of R [L, L'], which is why we have failed to achieve an accurate critical point λ_4 and the associated exponents (see Fig. 5.9). The actual reason for this behaviour can be attributed to the anomalous distribution of extended state (NPR≠ 0) near the transition.

Furthermore, we reconfirm that the critical exponents from the scaling relation of the PR_L which denotes the participation ratio corresponding to different system sizes using Eq. 2.25 and can be written as $PR_L \sim L^{\gamma/\nu}$. From this relation, a plot between $log(PR_L)$ and $log(L)$ for different lengths L at the critical point should result in a straight line with slope γ/ν. We performed this analysis at all the three critical points, such as λ_1, λ_2 and λ_3 in Fig. 5.10 and obtain the values of γ/ν as 0.83 ± 0.05, 0.77 ± 0.04 and 0.79 ± 0.03 respectively. The exponents obtained in our analysis should satisfy a hyper-scaling law expressed as, [103]

$$\frac{2\beta}{\nu} + \frac{\gamma}{\nu} = 1. \tag{5.2}$$

Using the hyper-scaling relation given in Eq. 5.2, it will be possible to extract another ratio of the exponents i.e. β/ν via

$$\frac{\beta}{\nu} = \frac{1}{2}\left(1 - \frac{\gamma}{\nu}\right). \tag{5.3}$$

Since at the critical point $\xi = L$, from Eq. 2.25 we have $\sigma_L \sim L^{-\beta/\nu}$. In order to establish the hyper-scaling relation we plot $\log(\sigma_L)$ as a function of $log(L)$ for different system sizes corresponding to the three critical points λ_1, λ_2, and λ_3 as depicted in Fig. 5.11. The slopes of the curves yield the exponent ratios $\beta/\nu = 0.086 \pm 0.03$, 0.116 ± 0.02 and 0.1 ± 0.02 for $\lambda_1 = 0.903$, $\lambda_2 = 1.836$ and $\lambda_3 = 2.127$ respectively. These values of the exponent ratios γ/ν (0.83, 0.77 and 0.79) and β/ν (0.086, 0.116 and 0.100) clearly satisfy the hyper-scaling relation (Eq. 5.2) at the critical points.

5.3.4 Hausdorff dimension

In our case, we also compute the Hausdorff dimension D_H by following Eq. 2.8 (for details see [sec. 2.2.2]) in two different critical regions corresponding to $\lambda = 1.2$ and 2.5, which respectively denote the first and the second intermediate regimes. In Fig. 5.12, we plot the total number of required box N_l as a function of box length l which exhibits a power law behaviour with exponent $D_H = 0.61$ (blue squares) and 0.85 (green diamonds) for $\lambda = 1.2$ (first intermediate regime) and 2.5 (second intermediate regime) respectively. For comparison, we have plotted the corresponding AA limit ($\delta = 1$, $\lambda_A = \lambda_B = \lambda = 2$) (red circles) which yields $D_H = 0.5$ [61]. We identify the former case as 'DIM' while the latter case is specified as 'AA'. From the analysis, it is realized that the Hausdorff dimension, in this case, is different from the standard AA model. It is observed that

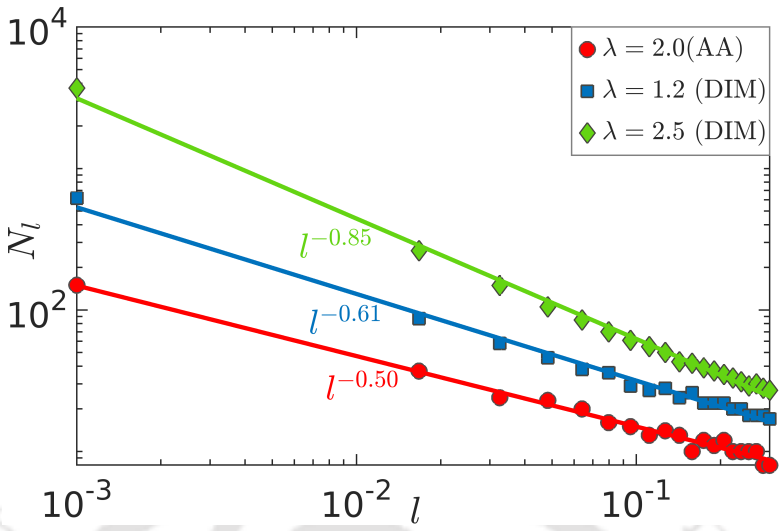

Figure 5.12: Figure shows N_l as a function of box length l in the log-log scale corresponding to $\lambda = 1.2$ (blue squares) and $\lambda = 2.5$ (green diamonds). We identify these two cases as 'DIM' and the corresponding chosen $\delta = 2.2$. For comparison, we have shown the result for the pure AA limit ($\delta = 1$ red circles). We identify the case as 'AA'. The slopes of these plots give the Hausdorff dimensions which are obtained as $D_H = 0.61$ and 0.85 for $\lambda = 1.2$ and 2.5 respectively. Note that for the AA model $D_H = 0.5$. The system size considered for the calculation is $L = 13530$.

the D_H corresponding to the first intermediate region possesses a larger value than the pure AA case, comparatively describing a less dense energy spectrum. Therefore, more number of mini gaps appear in the spectrum, resulting in a fractal nature. In addition to that, the second intermediate region holds a larger value of D_H compared to the pure AA and the first intermediate region of the dimerized model, thereby indicating a more fractal nature. Hence, we conclude that the energy spectrum is fractal in the presence of quasiperiodic potential. However, the combined effect of dimerization and the staggered quasiperiodic potential causes the spectrum to be more fractal than the pure AA model. In addition, the spectrum of the second intermediate region is more fractal than the first one.

5.4 Conclusions

A one-dimensional quasiperiodic lattice model in the presence of hopping dimerization and a staggered on-site quasiperiodic potential exhibits re-entrant localization transitions. The transitions occur for a range of dimerization strength through two intermediate phases resulting in four critical points. In this work, we have performed the multifractal analysis of the eigenstates and found that the states within the intermediate phases are multifractal in nature. Further, we characterize these transition points by using appropriate critical state analysis for different order parameters. We also obtain the associate critical exponents which are found to obey the hyper-scaling laws. It is also observed that the second (intermediate - localized) and the third (localized - intermediate) phase transitions belong to the same universality class. Note that while we are able to accurately determine the first three critical points associated to the first localization transition, we fail to determine the last critical point of transition to the second localized phase. Finally, we have calculated the Hausdorff dimension at the two critical regions which are found to be different from the standard AA limit.

CHAPTER 6

CRITICAL ANALYSIS AND TOPOLOGICAL PHASES OF DIMERIZED KITAEV CHAIN IN PRESENCE OF QUASIPERIODIC POTENTIAL

6.1 Introduction

In the previous chapters, we have explored a reentrant localization transition and critical properties associated with it in a one-dimensional dimerized model (SSH model [sec. 2.5]) in presence of staggered quasiperiodic (QP) potential. We further plan to explore another aspect of this dimerized model in the QP potential background as detailed below. It is known that the SSH model looses its topological properties due to the breakdown of the chiral symmetry in the presence of an onsite potential. However, incorporating *p*-wave superconducting correlations, in combination with the SSH model (or in other words, dimerized hopping), aids in the topological features of the model due to another symmetry, namely the particle-hole symmetry, which is present inherently in a superconductor. A theoretical paradigmatic model to study a one-dimensional *p*-wave superconductor is known as the Kitaev chain model [sec. 2.6]. Among the members of the generalized Kitaev model [153, 154, 155, 52, 156], we are interested in a dimerized Kitaev chain, which is shown to have significant interest [114, 157, 158, 159]. A dimerized Kitaev chain is a hybrid model with a one-dimensional SSH chain and a Kitaev chain which possesses very rich physics and symmetry properties. There are signatures of a trivial phase, SSH-like, and Kitaev-like topological phases present in a single system.

Further, the interplay of topology and disorder have gained a lot of attention in recent years. Up till now, it is known that a topological phase sur-

vives in presence of a weak disorder. However, there will be a transition from the topologically non-trivial phase to the topologically trivial phase in the strong disorder limit. Very recently there has been a remarkable observation where the presence of disorder can drive a trivial phase to a topological phase, known as the topological Anderson insulator[160]. Subsequently, several other models have reported the same behavior theoretically and experimentally [161, 162, 163, 164, 165]. The dimerized Kitaev chain in the presence of a random potential has also demonstrated a similar behavior [166].

Drawing motivations from the above results, in this chapter we consider a dimerized Kitaev chain in the presence of onsite QP potential. Here, we study the localization and the topological properties of this model via computing several important physical quantities. We observe a series of phase transitions occurring in the system, such as extended-critical-localized phases due to the competition between the dimerization and the QP potential strength. We infer that our model hosts a critical phase consisting of two different anomalous mobility edges separating the extended and the localized phases, and a second one intervening the critical and the localized phases. Hence a broad regime with critical (multifractal) states arise, resulting in an extended multifractal phase. This is a significant result. In addition to this, we study the properties of the zero-energy edge modes. We find that the onsite QP potential will drive the system from a topologically trivial to a non-trivial (Topological Anderson) phase beyond a certain critical dimerization strength. Beyond this critical strength, it exhibits another transition from a topologically non-trivial phase to the Anderson localized phase in presence of a strong QP potential.

The rest of the chapter is organized as follows. First, we describe the model

in sec. 6.2. Further, the results are reported and analyzed in sec. 6.3. Here, we discuss the localization properties in sec. 6.3.1 and topological features in sec. 6.3.7. Finally, we conclude our observations in sec. 6.4.

6.2 Model

Here we consider a one-dimensional spinless fermionic chain comprising of two distinct atoms (sublattices) in a unit cell. The hopping and the p-wave superconducting pairing strengths are assumed to alternate between strong (within the unit cell) and weak bonds (between the unit cells). Moreover, the onsite chemical potentials (μ) at the two sublattices within a unit cell are modulated quasiperiodically. The Hamiltonian of such a system is represented by [167],

$$\begin{aligned} H = &-t\sum_{m=1}^{N}\Big((1+\delta)\hat{c}^{\dagger}_{m,B}\hat{c}_{m,A} + \text{H.c.}\Big) - t\sum_{m=1}^{N-1}\Big((1-\delta)\hat{c}^{\dagger}_{m+1,A}\hat{c}_{m,B} + \text{H.c.}\Big) \\ &+\Delta\sum_{m=1}^{N}\Big((1+\delta)\hat{c}^{\dagger}_{m,B}\hat{c}^{\dagger}_{m,A} + \text{H.c.}\Big) + \Delta\sum_{m=1}^{N-1}\Big((1-\delta)\hat{c}^{\dagger}_{m+1,A}\hat{c}^{\dagger}_{m,B} + \text{H.c.}\Big) \\ &-\sum_{m=1}^{N}[\mu_A c^{\dagger}_{m,A}c_{m,A} + \mu_B c^{\dagger}_{m,B}c_{m,B}) \end{aligned} \tag{6.1}$$

where the quasiperiodically modulated onsite chemical potentials at the two sublattices are denoted by,

$$\mu_A = \lambda_A \cos[2\pi\beta(2m-1) + \phi]$$

$$\mu_B = \lambda_B \cos[2\pi\beta(2m) + \phi].$$

Here, the length of the chain is represented by $L = 2N$ with the unit cell index m (= 1, 2, . . ., N). In each unit cell, there are two sublattice sites, namely, A and B with the corresponding number operators being $\hat{n}_{m,A}$ and $\hat{n}_{m,B}$, respectively. The creation (annihilation) operators to create an electron at the sublattice sites

(m, A) and (m, B) are given by $\hat{c}^{\dagger}_{m,A}$ ($\hat{c}_{m,A}$) and $\hat{c}^{\dagger}_{m,B}$ ($\hat{c}_{m,B}$), respectively. The intra-cell (strong) and inter-cell (weak) hopping strengths are defined by $t(1+\delta)$ and $t(1-\delta)$ with t and δ being the nearest-neighbour hopping strength and the dimensionless dimerization strength, respectively. To keep the hopping term positive, we impose a constraint on the dimerization strength, namely, $|\delta| < 1$. Similarly, the intracell (strong) and intercell (weak) p-wave superconducting paring strength of the system are defined by $\Delta(1+\delta)$ and $\Delta(1-\delta)$. The onsite quasiperiodic potential strengths at the two sublattices are denoted by λ_A and λ_B, respectively. The periodicity of the potential is given by $1/\beta$. In this work, β is taken as the golden ratio, that is, $\beta = \frac{(\sqrt{5}-1)}{2}$. The phase term of the potential is represented by ϕ which is taken as zero. We keep the p-wave pairing strength to be real and positive, that is, $\Delta = 0.5$. Additionally, we choose the onsite quasiperiodic potential strengths λ_A and λ_B to be equal and opposite in magnitude, that is, $\lambda_A = -\lambda_B = \lambda$. We have taken t as the unit of energy throughout, that is, $t = 1$.

In the presence of a p-wave superconducting pairing, the Hamiltonian has terms quadratic in the fermionic creation (and annihilation) operators. Thus, the Hamiltonian can be solved by using the Bogoliubov-de Gennes (BdG) transformation. In order to do that, we define a quasiparticle operator obtained via superposition of the single-particle creation ($c^{\dagger}$) and annihilation (c) operators, namely,

$$\phi^{\dagger}_{n} = \sum_{m=1,\alpha=A,B}^{N} [u^{(n)}_{m,\alpha} c^{\dagger}_{m,\alpha} + v^{(n)}_{m,\alpha} c_{m,\alpha}] \tag{6.2}$$

where α and n denote the sublattice index and the energy band index, respectively. $u^{(n)}_{m,\alpha}$ and $v^{(n)}_{m,\alpha}$ are the amplitudes of the wavefunction at the sublattice sites

(m, α), which we are taken to be real. Subsequently, the wavefunction becomes,

$$|\psi_n\rangle = \phi_n^\dagger|0\rangle \tag{6.3}$$

$$= \sum_{m=1,\alpha=A,B}^{N} [u_{m,\alpha}^{(n)} c_{m,\alpha}^\dagger + v_{m,\alpha}^{(n)} c_{m,\alpha}]|0\rangle. \tag{6.4}$$

Hence, the Schrödinger equation, can be written as,

$$\begin{pmatrix} A & B \\ -B & -A \end{pmatrix} \begin{pmatrix} u_{m,\alpha}^{(n)} \\ v_{m,\alpha}^{(n)} \end{pmatrix} = E_n \begin{pmatrix} u_{m,\alpha}^{(n)} \\ v_{m,\alpha}^{(n)} \end{pmatrix} \tag{6.5}$$

where A and B are matrices, whose components are given by,

$$\begin{aligned} A_{m,\alpha} = & -t(1+\delta)\Big[\delta_{(m,A),(m,B)} + \delta_{(m,B),(m,A)}\Big] \\ & - t(1-\delta)\Big[\delta_{(m+1,A),(m,B)} + \delta_{(m,B),(m+1,A)}\Big] \\ & - \mu_A \delta_{(m,A),(m,A)} - \mu_B \delta_{(m,B),(m,B)} \end{aligned} \tag{6.6}$$

$$\begin{aligned} B_{m,\alpha} = & \Delta(1+\delta)\Big[\delta_{(m,A),(m,B)} - \delta_{(m,B),(m,A)}\Big] \\ & \Delta(1-\delta)\Big[\delta_{(m,B),(m+1,A)} - \delta_{(m+1,A),(m,B)}\Big]. \end{aligned} \tag{6.7}$$

Using the BdG equations in (Eq. 6.5), the single-quasiparticle spectrum (E_n), and the amplitudes $u_{m,\alpha}^{(n)}$ and $v_{m,\alpha}^{(n)}$ of the wavefunction can be calculated.

The particle-hole symmetry is inherently present in the BdG Hamiltonian. Thus corresponding to each particle-like solution ($u_\alpha^{(n)}$ and $v_\alpha^{(n)}$) with eigenenergies $+E$, there will be a hole-like solution with $-E$. Only the zero-energy states ($E = 0$) are self-conjugate.

6.3 Results

In this chapter, we shall study the effect of an onsite QP potential on the localization properties via analysing the eigenenergies and the eigenstates of the Hamiltonian, and explore the topological properties using the real-space winding number and the number of the of MZMs present in the system. The results will elucidate the critical properties of the model and shed light on the topological features as well [167].

6.3.1 Localization properties

In this section, we explore the localization properties of the eigenstates of the system under periodic boundary condition. In order to do that, we use two diagnostic tools, such as inverse participation ratio (IPR) and the normalized participation ratio (NPR) to distinguish between the extended, critical, and localized properties. The IPR and the NPR corresponding to the n^{th} eigenstate of the BdG Hamiltonian are defined as [140],

$$\mathrm{IPR}^{(n)} = \sum_{m=1,\alpha=A,B}^{N} \left[|u_{m,\alpha}^{(n)}|^4 + |v_{m,\alpha}^{(n)}|^4 \right] \tag{6.8}$$

and

$$\mathrm{NPR}^{(n)} = \left[L \sum_{m=1,\alpha=A,B}^{N} \left[|u_{m,\alpha}^{(n)}|^4 + |v_{m,\alpha}^{(n)}|^4 \right] \right]^{-1} \tag{6.9}$$

where $u_{m,\alpha}^{(n)}$ and $v_{m,\alpha}^{(n)}$ are the solutions of the BdG equations. It is known that the IPR value of an extended state goes to zero, while for the localized state, it is always stays finite and acquires a value '1' in the thermodynamic limit. On the other hand, the NPR value denotes finite values corresponding to an extended state, while, for the localized state, it tends to zero in the thermodynamic limit.

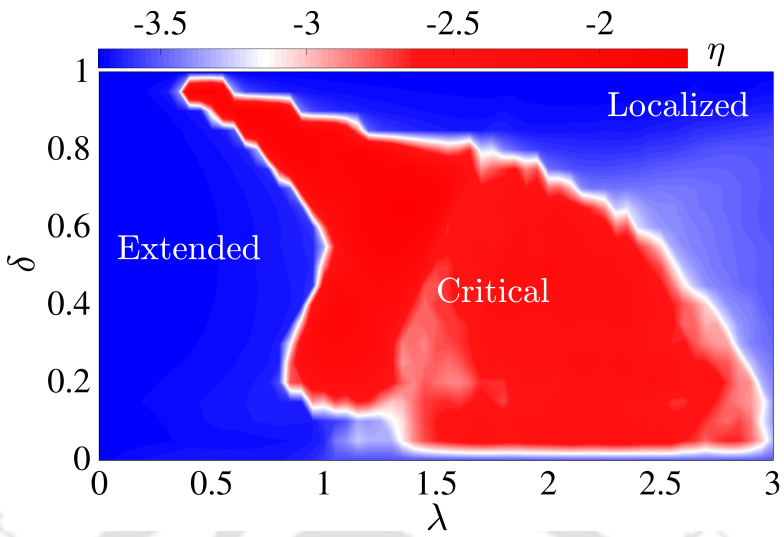

Figure 6.1: The phase diagram is shown using the variable η as a function of δ and λ. The length of the chain we consider for the calculation is $L = 5168$.

Moreover, we are interested in the global properties of the model. Since our system respects the particle-hole symmetry, we only consider the quasiparticle spectra of the BdG Hamiltonian in our calculations. Hence, the average of the IPR and the NPR are given by [140],

$$\begin{aligned} \langle \text{IPR} \rangle &= \tfrac{1}{L} \textstyle\sum_{n=1}^{L} \text{IPR}^{(n)} \\ \langle \text{NPR} \rangle &= \tfrac{1}{L} \textstyle\sum_{n=1}^{L} \text{NPR}^{(n)}. \end{aligned} \tag{6.10}$$

6.3.2 Phase diagrams

To begin with, we present a phase diagram with the help of $\langle \text{IPR} \rangle$ and $\langle \text{NPR} \rangle$ in the parameter space defined by the dimerization strength (δ) and the QP potential strength (λ) in Fig 6.1. In order to obtain a detailed illustration of the phase diagram, we need to segregate different phases, such as the extended, critical (intermediate), and the localized phases. The coexistence of different types of

states gives rise to the critical phase. Thus, we introduce the quantity, η which is discussed in Eq. 4.2. Although, the value of η distinguishes the critical phase from the extended and the localized ones, it is, however incapable of distinguishing between the localized phase from the delocalized phase. Thus, it only helps us to identify the critical phase in the phase diagram. Hence, we need another quantity to discern the localized phase from the delocalized phase.

Following Eq. 2.5, the average value of the fractal dimension calculated over a narrow band comprising of a few low-lying quasiparticle states and the BdG quasiparticle spectrum are denoted by $\langle D_2 \rangle$ and $\overline{D_2}$, respectively. Again, the average value of the fractal dimension will not capture the overall nature of the system. Thus, we need to consider both the quantities, namely, η and the average value of the fractal dimension $\langle D_2 \rangle$ together to acquire a good knowledge on the emergent phases of the system.

In Fig 6.1, we show the phase diagram using η in the parameter space spanned by δ (dimerization strength) and λ (QP potential). It denotes the global nature of the system, with the 'Blue' color corresponding to the extended and the localized phases and the 'red' color refers to the critical phase of the system. Therefore, the system hosts a critical phase over a large parameter regime denoted by δ and λ. Among the two extreme cases, that is, when no dimerization is present ($\delta = 0$), it is observed that, all the eigenstates are extended in nature up to a value $\lambda \simeq 1$. Upon increasing the potential strength, the eigenstates become critical (multifractal). On the contrary, in the strong dimerization limit ($\delta = 1$), all the states are localized irrespective of the values of λ. Further, at an intermediate point of the dimerization strength, say, $\delta \simeq 0.6$, it is observed that an extended phase persists up to $\lambda \sim 1$, beyond which, a critical phase appears

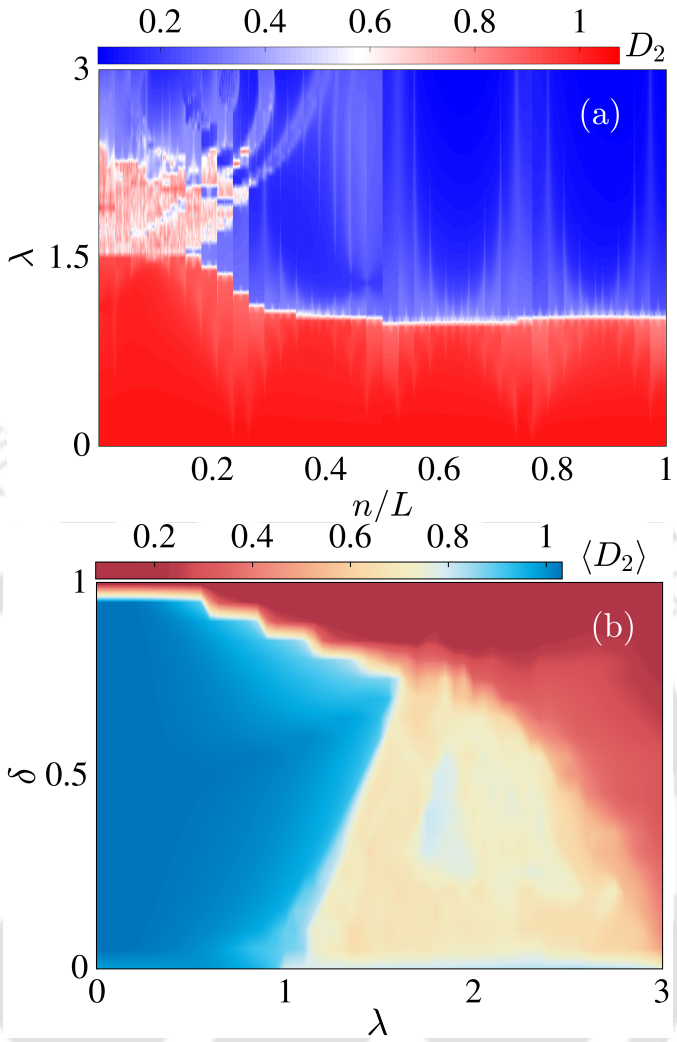

Figure 6.2: (a) The fractal dimensions (D_2) are shown for the the BdG quasiparticle spectrum as a function of λ. The system length is taken as $L = 8362$. (b) A phase diagram using the fractal dimensions ($\langle D_2 \rangle$) is plotted as a function of δ and λ. In this calculation, we consider only a band of low-lying energy states from the quasiparticle spectrum. The length of the chain we consider for the calculation is $L = 5168$.

which persists up to a value given by $\lambda_c \simeq 2.4$. Finally, the localization transition occurs at values larger than the critical λ_c, leading to a completely localized phase.

In Fig 6.2 (a), we show an intuitive picture of the eigenspectrum and their

sensitivity to the variation of λ for $\delta = 0.6$. Hence, we plot D_2 corresponding to the BdG quasiparticle spectrum as a function of the QP potential strength, λ. Different eigenstates experience localization transitions at different values of the potential indicating the presence of an energy-dependent phase transition. In this situation, since mobility edge is not appropriate terminology, we wish to address it as an anomalous mobility edge onwards. Thus an anomalous mobility edge should be observed in the presence of the dimerization and the staggered potential. In general, it is observed that the lower energy states of the spectrum (near the zero energy) are necessary to demonstrate a localization transition at large values of λ. In comparison, the higher energy states undergo a transition at weaker potential strengths. For small values of λ, all the quasiparticle eigenstates are extended in nature, thereby giving rise to a completely delocalized phase. Beyond this, the onset of localization occurs at $\lambda \simeq 1$ corresponding to of the higher energy states, leading to a critical phase comprising of a mixture of the extended and the localized states. Hence, an anomalous mobility edge appears between the extended and the localized states. Interestingly, while with the increase in λ, the critical phase persists, the extended nature corresponding to the lower energy states is replaced by the critical (multifractal) states within a range of λ given by $1.5 < \lambda < 2.5$. Thus we observe another anomalous mobility edge, which arises between the critical (multifractal) and the localized states. Finally, at a higher value of λ, all states become localized.

Therefore, we infer that the lower energy eigenstates experience a series of transitions, namely, from the extended to critical (multifractal) and hence to the localized one. This indicates the presence of a critical region sandwiched between the extended and the localized phases. However, corresponding to the higher energy states, there is a sharp transition from an extended to a local-

ized phase. Thus, our results offer two different anomalous mobility edges, one between the extended and the localized and another between the critical (multifractal) and the localized phases. Hence obtaining two different anomalous mobility edges in the dimerized Kitaev chain model in presence of a QP potential comprises of an important highlight of our work.

In Fig 6.2 (b), we show the average value of the fractal dimension ($\langle D_2 \rangle$) in the parameter space spanned by of δ and λ corresponding to a band of lower energy states appearing in Fig 6.2 (a). It is depicted that in the case of weaker potential strengths (small λ), all the eigenstates are extended in nature irrespective of the value of δ ($0 < \delta < 1$). Beyond the critical point, $\lambda \simeq 1$, a critical phase appears with critical (multifractal) nature of the eigenstates within $0.2 < \delta < 0.8$. These multifractal states are affected by larger values of δ, resulting in shrinking of the critical phase. Finally, a complete localization occurs at stronger potential strengths. Therefore, we observe three distinct phases, such as, the extended, critical (multifractal), and the localized as a function of the QP potential strength λ.

It is noticeable that, in Fig 6.1 and Fig 6.2 (b), the area of the extended phase are not identical, it rises in Fig 6.2 (b). In Fig 6.1, the phase diagram is shown via computing a quantity η. In addition, Fig. 2(b) is obtained via computing the average value of the fractal dimension by considering some of the low-lying quasiparticle states. In the first case, the extended phase comprises of all the eigenstates which are extended in nature. On the other hand, the critical phase hosts a mixture of the extended and the localized states. Therefore, in the calculation of the average value of a fractal dimension, some of the contributions of the extended states from the critical phase enhance the area of the extended

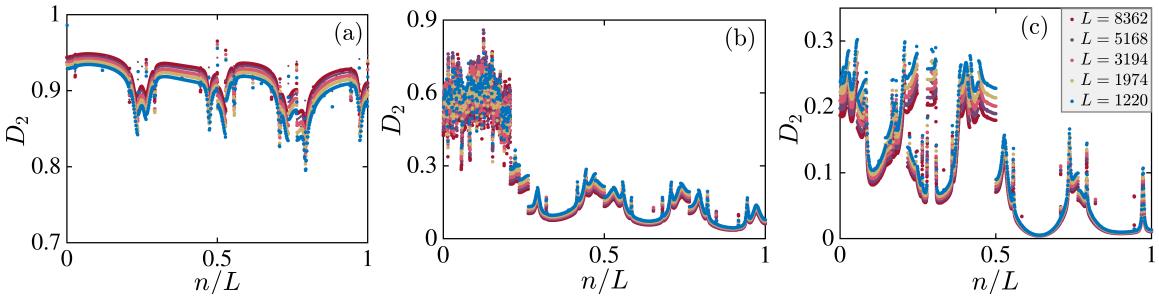

Figure 6.3: The fractal dimension (D_2) as a function of eigenstate index ratio (n/L) are shown in (a) $\lambda = 0.50$, $\delta = 0.60$, (b) $\lambda = 1.70$, $\delta = 0.60$, and (c) $\lambda = 3.00$, $\delta = 0.60$ for various system sizes, mentioned in the figure.

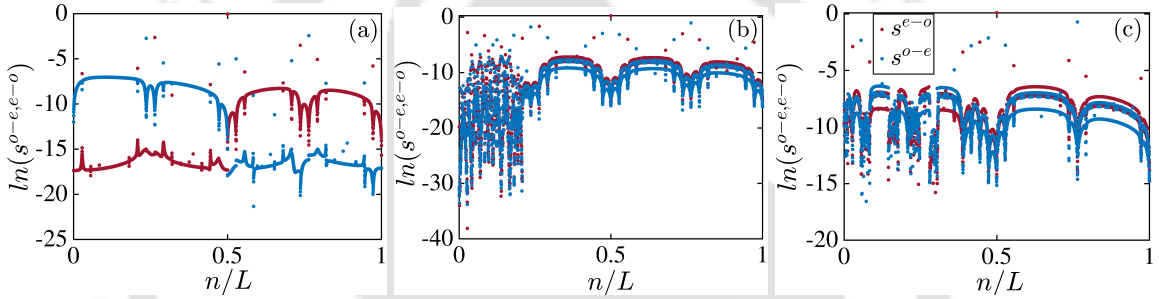

Figure 6.4: The level spacing as a function of eigenstate index ratio (n/L) are shown in (a) $\lambda = 0.50$, $\delta = 0.60$, (b) $\lambda = 1.70$, $\delta = 0.60$, and (c) $\lambda = 3.00$, $\delta = 0.60$. The system length is taken as $L = 8362$.

phase in Fig 6.2 (b), which can be seen from Fig 6.2 (a).

6.3.3 Fractal dimension

In order to have a complete understanding of these different phases, we study D_2 by considering different system sizes, such that, $L = 8362,\ 5168,\ 3194,\ 1974,$ and 1220, which are shown via different colors in Fig 6.3. In Fig 6.3, we plot D_2 as a function of the eigenstate index ratio (n/L) corresponding to three representative points (parameter values) from each of the phases. For the dimerization

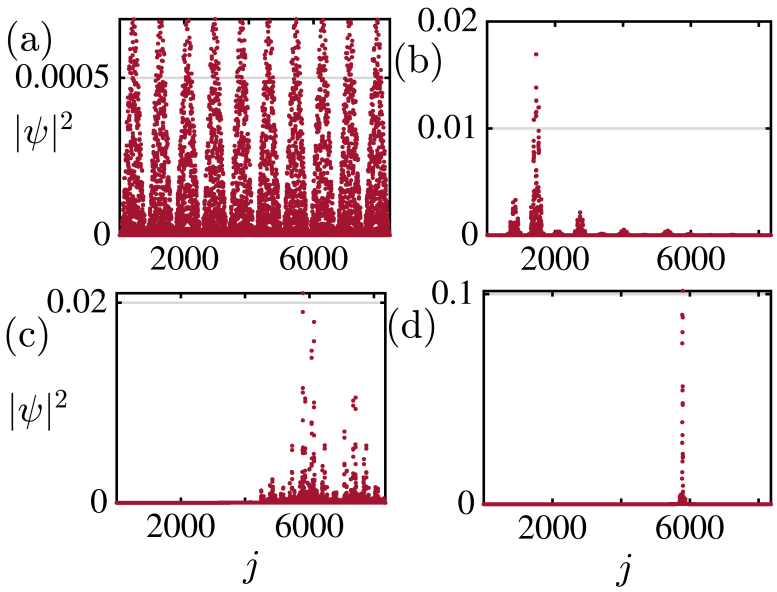

Figure 6.5: The probability distribution of eigenstates as a function of site indices (j) are shown for (a) $\lambda = 1.5$, (b) $\lambda = 1.55$, (c) $\lambda = 2.4$, and (d) $\lambda = 2.45$ corresponding to $\delta = 0.6$. The system size we consider here is $L = 8362$.

strength, $\delta = 0.6$, we choose $\lambda = 0.5$ for the extended phase, $\lambda = 1.7$ for the critical (multifractal) phase, and $\lambda = 3.0$ for the localized phase. In Fig 6.3 (a), it is observed that, the values of D_2 corresponding to all the states move towards the value $D_2 = 1$ as L increases, implying a the presence of a completely extended phase in the thermodynamic limit. Most interestingly, in Fig 6.3 (b), the values of D_2 fluctuate around a value $D_2 \simeq 0.6$ for different L, thereby demonstrating a fractal nature. However, the higher energy states approach towards a value $D_2 = 0$ with increasing L, indicating a localized behavior. Thus we observe an anomalous mobility edge to occur between the multifractal and the localized states. Finally, in Fig 6.3 (c), we find that all the states corresponding to both the lower and the higher energies approach zero with increasing L, thereby exhibiting a completely localized phase.

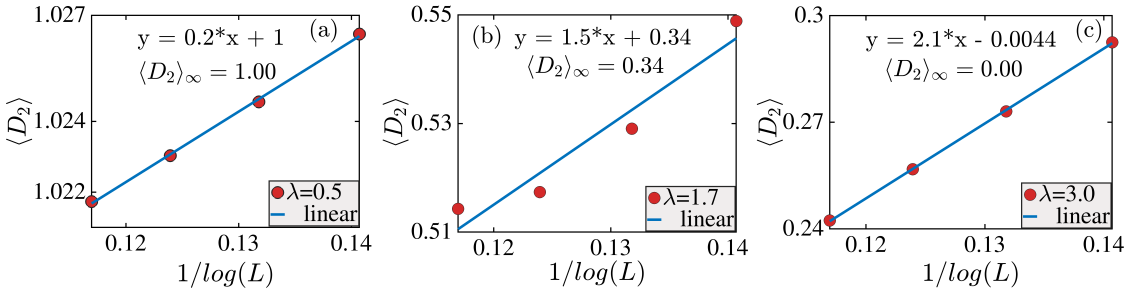

Figure 6.6: The average value of fractal dimension ($\langle D_2 \rangle$) as a function of system sizes are shown in (a) $\lambda = 0.50$, $\delta = 0.60$, (b) $\lambda = 1.70$, $\delta = 0.60$, and (c) $\lambda = 3.00$, $\delta = 0.60$. The system sizes are taken as $L = 5168,\ 3194,\ 1974$, and 1220.

6.3.4 Level-spacing

Following the theory of level-spacing, which is explained in sec. 2.2.1, we study the localization properties of the system via eigenenergies. In Fig 6.4 we plot the level-spacing corresponding to the same parameter choices as that for the calculation of D_2 in Fig 6.3, which are $\lambda = 0.5,\ 1.7$, and 3.0 for $\delta = 0.6$. In this study, we expect to witness a gap in the extended phase corresponding to $\lambda = 0.5$ shown in Fig 6.4 (a). Later, for $\lambda = 1.7$ in Fig 6.4 (b), distinctly noticeable fluctuations occur in the lower energy spectrum. While the higher energy states are localized in nature. Further, at $\lambda = 3$ in Fig 6.4 (c), no gap between s_n^{e-o} and s_n^{o-e} is observed thereby indicating a localized behavior.

6.3.5 Probability distribution

The nature of an extended state is to spread over the entire lattice, while the localized states only span over a very few lattice sites. In contrast, a multifractal state is fundamentally different from the above two, implying neither an extended nor a localized behavior. To have a clear visualization of the phase

transition, we plot the probability distribution of the eigenstates as a function of the site indices in Fig 6.5. We observe that, the probability distribution at $\lambda = 1.5$ and $\delta = 0.6$ (Fig 6.5 (a)) spreads uniformly over the entire lattice, hence denoting an extended nature. Further, at $\lambda = 1.55$ and $\delta = 0.6$ (Fig 6.5 (b)), we observe a fluctuating nature of the states, which aids us in identifying it as multifractal states. Afterwards, at $\lambda = 2.4$ and $\delta = 0.6$ (Fig 6.5 (c)) the state is a multifractal, and finally at $\lambda = 2.45$ and $\delta = 0.6$ (Fig 6.5 (d)), the states are highly localized and span over only a few of the lattice sites.

6.3.6 Finite-size analysis

Finally, to have a concrete validation of the extended-critical-localized phase transition, we perform a finite-size scaling analysis of the fractal dimension. In order to do that, we calculate $\langle D_2 \rangle$ using a narrow band consisting of low-lying quasiparticle eigenstates, which is plotted as a function of the system lengths. The system sizes are taken as $L = 5168,\ 3194,\ 1974$, and 1220. The intercept of the linear plot will provide the value of $\langle D_2 \rangle$ in the thermodynamic limit. In Fig 6.6, we show the scaling behavior of $\langle D_2 \rangle$ with the system sizes corresponding to $\lambda = 0.5$ (extended) in Fig 6.6(a), $\lambda = 1.7$ (critical) in Fig 6.6 (b), and $\lambda = 3.0$ (localized) in Fig 6.6 (c) for a dimerization strength $\delta = 0.6$. Following this, we also show $\langle D_2 \rangle$ as a function of λ corresponding to various δ values in Fig 6.7 (a). The results clearly distinguish between the three phases by demonstrating a value 1 for the extended phase, a fractional value (between 0 to 1) for the critical phase, and zero for the localized phase, which we have also inferred earlier from the phase diagram presented in Fig 6.2 (b). In addition to this, we also study the variation of the average D_2 ($\overline{D_2}$) over the quasiparticle spectra as a

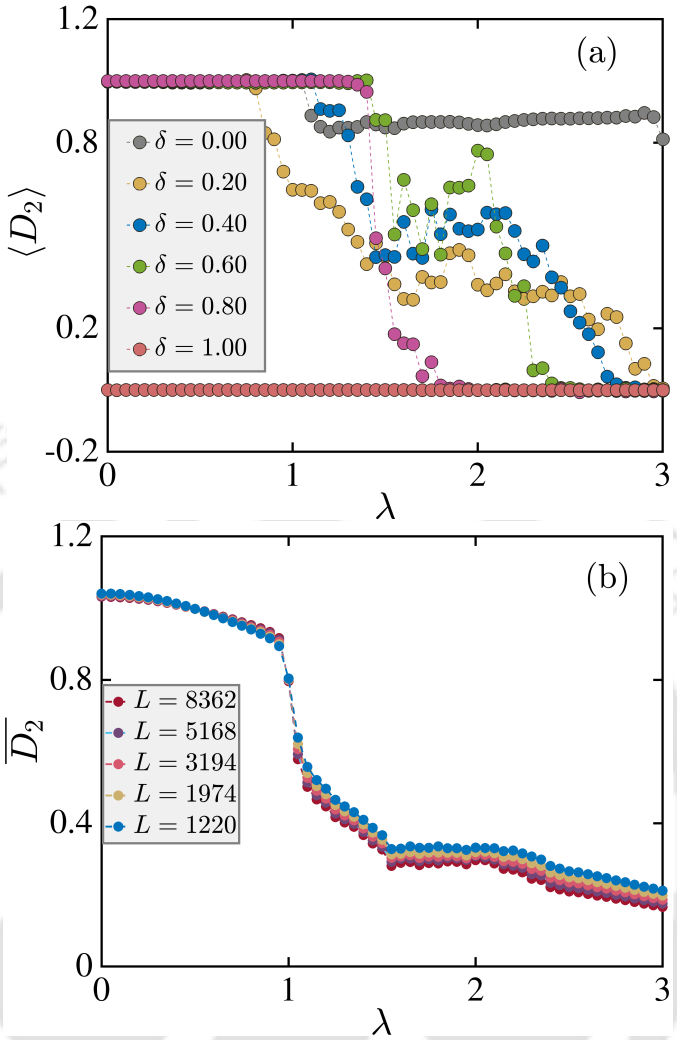

Figure 6.7: (a) The average value of D_2 ($\langle D_2 \rangle$) over a narrow band of states and (b) The average value of D_2 ($\overline{D_2}$) over the quasiparticle spectrum as a function of λ are shown.

function of λ for L = 8362, 5168, 3194, 1974, and 1220 in Fig 6.7 (b) corresponding to $\delta = 0.6$. The crossing of the curves at $\lambda_c \simeq 1$ implies a phase transition from an extended to a critical phase. However, the critical to the localized phase transition is not clearly captured. The results match with the phase diagram presented in Fig 6.1.

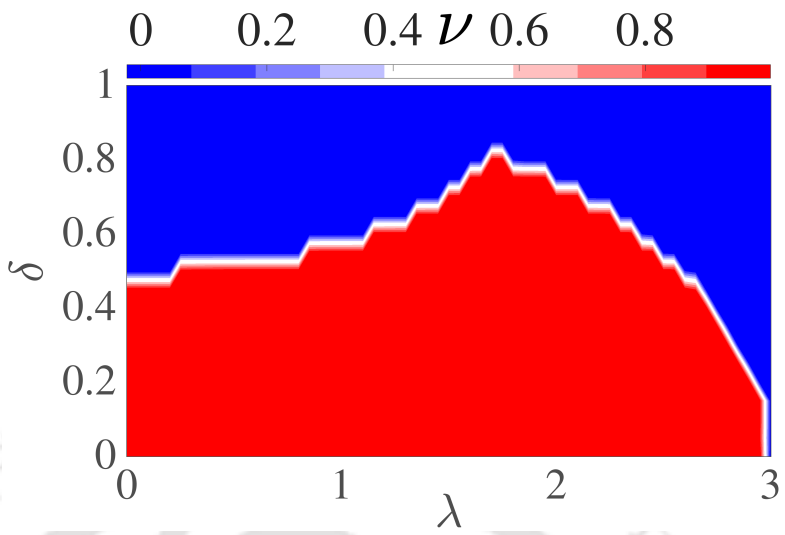

Figure 6.8: The real-space winding number is plotted as a function of λ. The length of the chain we consider for the calculation is $L = 5168$.

6.3.7 Topological properties

In this section, we investigate the topological properties of the zero-energy edge modes that emerge in our model. In general, it is known that the topologically non-trivial phase appears to be robust for weak values of potential. However, there is a phase transition from the topological non-trivial to the trivial phase in presence large QP potential. Thus a topological invariant is required to identify them separately. Here, we shall characterize the topological nature by the topological invariant (see below) and the number of the MZMs. Since the potential breaks the translational symmetry, we shall use the real-space winding number as the topological invariant which is explained in sec. 2.6.5.

6.3.8 Topological and universal Phase diagrams

In Fig 6.8, we show the phase diagram via the real-space winding number ν as a function of δ and λ using periodic boundary condition. While ν has a value 1 corresponding to the topological phase, it is 0 for the trivial phase. Here, we observe a topologically non-trivial phase up to $\lambda \simeq 3$ corresponding to no dimerization ($\delta = 0$). In addition, the model has a topologically trivial phase at the strong dimerization limit ($\delta = 1$). However, a certain region of δ, namely, $0.5 < \delta < 0.8$ shows an intriguing nature. It is illustrated that, in this region, the system is in a topologically trivial phase for the clean limit ($\lambda = 0$). With increasing λ and beyond the moderate values, the system enters into a topologically non-trivial regime which spans over a range of λ. Finally, the model exhibits a transition from the topologically non-trivial to an Anderson localized phase at large QP potential strengths.

In the absence of the onsite potential, that is, $\lambda = 0$, the system possesses the translational invariance which allows us to write the Hamiltonian in the momentum space,

$$H(k) = \sum_k \psi_k^\dagger H_0(k) \psi_k \tag{6.11}$$

where $\psi_k = (c_{k,A}, c_{k,B}, c^\dagger_{-k,A}, c^\dagger_{-k,B})$. Hence, the Bloch Hamiltonian is given by,

$$H_0(k) = \begin{pmatrix} 0 & h(k) & 0 & g(k) \\ h^*(k) & 0 & -g^*(k) & 0 \\ 0 & -g(k) & 0 & -h(k) \\ g^*(k) & 0 & -h^*(k) & 0 \end{pmatrix} \tag{6.12}$$

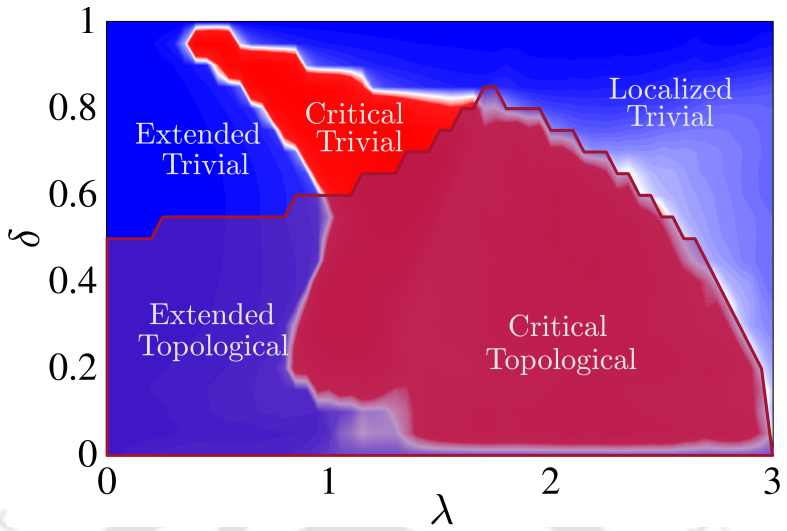

Figure 6.9: A universal phase diagram as a function of dimerization strength (δ) and QP potential strength (λ) is shown. We obtained three phases such as extended, localized, and critical, corresponding to the bulk states of the system. In addition to that, depending on the properties of the localized zero-energy edge modes, topological and trivial phases are specified.

where

$$h(k) = -t(1+\delta) - t(1-\delta)e^{-ika}$$

and

$$g(k) = -\Delta(1+\delta) + \Delta(1-\delta)e^{-ika}.$$

Here a is the lattice constant which is taken to be unity in the following calculation. Hence, the spectrum of the Hamiltonian is given by,

$$E(k) = \pm\sqrt{|h(k)|^2 + |g(k)|^2 \pm \sqrt{[h(k)g^*(k) + g(k)h^*(k)]^2}}. \tag{6.13}$$

From the energy spectrum, we find at $k = 0$ and π,

$$E(0) = \pm 2\Delta\delta \pm \sqrt{4t^2} \tag{6.14}$$

and

$$E(\pi) = \pm 2\Delta \pm \sqrt{4t^2\delta^2} \tag{6.15}$$

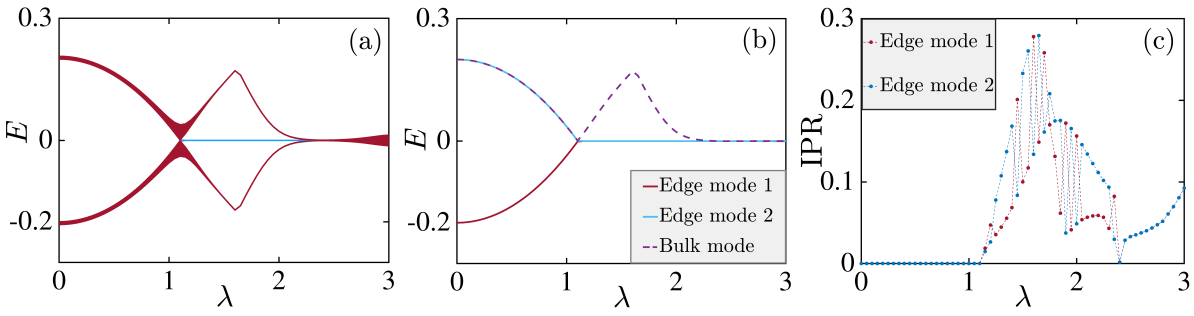

Figure 6.10: Eigenenergies are shown as function of λ in (a). Zero-energy edge modes and a bulk mode are plotted as a function of λ in (b). IPR value corresponding to the zero-energy edge modes as function of λ is shown in (c). The length of the chain we consider for the calculation is $L = 8362$.

The corresponding gap closing condition from Eq. 6.14 is given by,

$$4t^2 = 4\Delta^2\delta^2 \tag{6.16}$$

which using Eq. 6.15 yields,

$$4\Delta^2 = 4t^2\delta^2. \tag{6.17}$$

Therefore, from Eq. 6.17, we have,

$$\Delta^2 = \delta^2 \quad \text{when } t = 1 \tag{6.18}$$

$$\Delta = \pm\delta. \tag{6.19}$$

Since we have considered $\Delta = 0.5$ in our analysis, we observe the gap closing occurring at $\delta = 0.5$ corresponding to $\lambda = 0$.

We also include a universal phase diagram that contains information on both the localization properties and the topological features in Fig. 6.9. In the parameter space defined by $\delta - \lambda$, we show trivial and topological phases in the extended, localized, and the critical regimes which are shown in the figure.

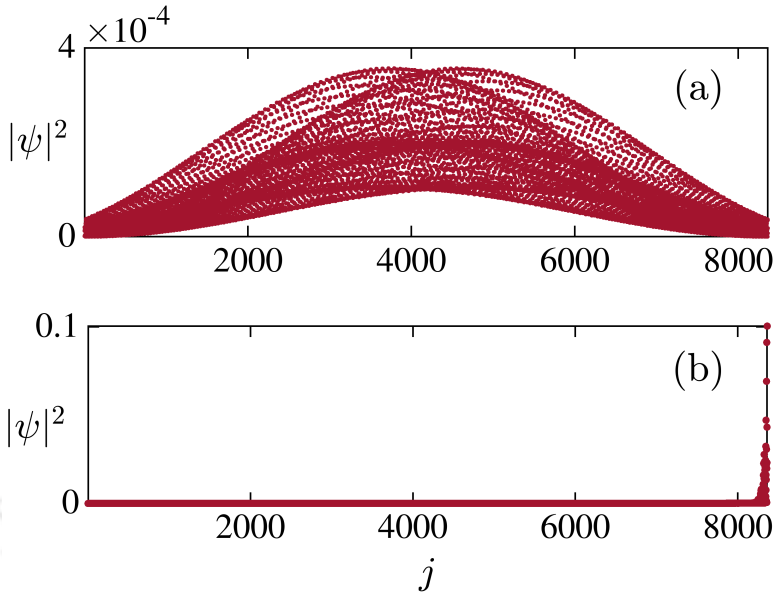

Figure 6.11: The probability distribution of eigenstates (near first transition) as a function of site indices (j) are shown corresponding to (a) $\lambda = 1.1$, $\delta = 0.6$ and (b) $\lambda = 1.15$, $\delta = 0.6$. The length of the chain we consider for the calculation is $L = 8362$.

6.3.9 Bulk-boundary correspondence

The real-space winding number extracts the details of the topological properties using the bulk states of the Hamiltonian. We also need the information on the edge modes to understand the bulk-boundary correspondence. Thus, we show some of the energy eigenvalues around the zero-energy as a function of λ corresponding to $\delta = 0.6$ in Fig 6.10 (a). The result exclusively shows that the bulk gap closes at $\lambda \simeq 1.1$. Later, with increasing λ, the zero modes persist up to $\lambda \simeq 2.4$. Finally, the two edge modes hybridize and merge with the bulk bands. For a clear visualization, we plot the zero energy edge modes and a single bulk mode in Fig 6.10 (b). Moreover, it is also fascinating to learn about the localization properties of these two edge modes. Thus, we show the IPR value corresponding to both of them as a function of λ in Fig 6.10 (c). It is observed

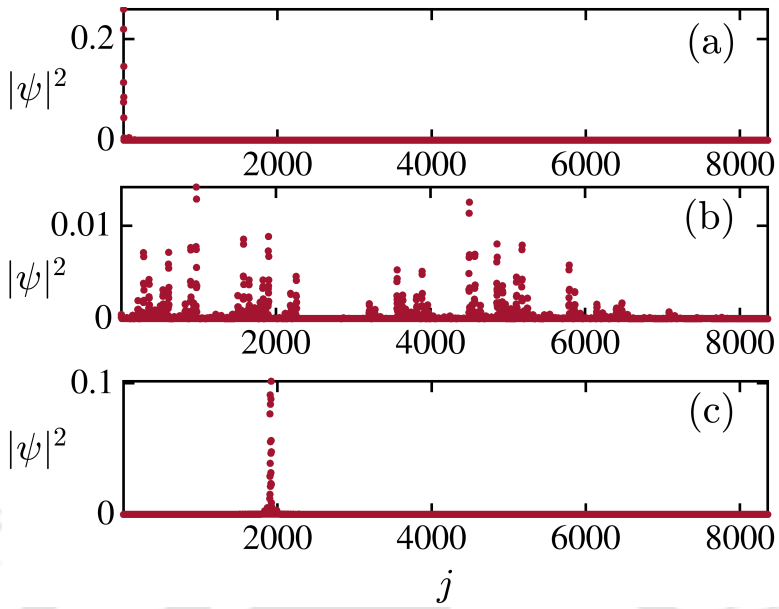

Figure 6.12: The probability distribution of the eigenstates (near second transition) as a function of site indices (j) are shown corresponding to (a) $\lambda = 2.35$, $\delta = 0.6$, (b) $\lambda = 2.40$, $\delta = 0.6$, and (c) $\lambda = 2.45$, $\delta = 0.6$. The length of the chain we consider for the calculation is $L = 8362$.

that the modes are extended in nature with IPR= 0 up to $\lambda \simeq 1.1$. With increasing λ, the states are localized at the two edges of the lattice up to a value such that $\lambda < 2.4$. Beyond $\lambda \geq 2.4$, the edge modes get hybridized with the bulk bands, and a complete Anderson localization transition occurs.

6.3.10 Probability distribution

We shall complement these results with the probability distribution of the energy eigenstates corresponding to the zero modes. In Fig 6.11, we plot the probability distribution of the edge states as a function of the first gap closing point. While in Fig 6.11 (a), the eigenstates are distributed uniformly throughout the lattice, Fig 6.11(b) shows that localization occurs at the edges of the lattice, in-

dicating a topological behavior. Further, in Fig 6.12, we plot the probability distributions of three of the eigenstates corresponding to three closely values of second transition point of λ, namely, $\lambda = 2.35,\ 2.4$, and 2.45. Following the previous analysis, the distribution shows that the eigenstates are located at the edges in Fig 6.12 (a), thereby demonstrating the presence of the zero-energy edge mode. Fig 6.12 (b) shows fluctuations that are occurring across the lattice sites, indicating an emergence of a multifractal behavior, and hence implies the presence of a critical point. Finally, in Fig 6.12 (c), the eigenstates show localized behavior that spans over a few of the sites in the bulk of the lattice, signalling the emergence of the localized states due to Anderson localization transition.

6.3.11 Finite-size analysis

Finally, we show the finite size analysis to characterize the topological phase transition corresponding to $\delta = 0.6$ in Fig 6.13. In this calculation, we chose the system sizes, such as, $L = 8362,\ 5168,\ 3194,\ 1974$, and 1220, which are shown with different colors. In Fig 6.13 (a), we plot the real-space winding number ν as a function of λ for different system sizes. The variation of ν with λ shows an sharp transition from 0 to 1 (beyond $\lambda = 1$), indicating a phase transition from a topologically trivial to non-trivial (Topological Anderson) at a particular value λ_1. The phase appears to persist up to a value λ_2 for all system sizes. Later, a second transition occurs, from a topologically non-trivial (Topological Anderson) to an Anderson localized phase. The same behavior is also obtained from the plot of the counts of the number of zero energy edge modes (Majorana zero modes (MZM)) as a function of λ in Fig 6.13 (b). The information exactly matches the results from the real-space winding number calculations. We also

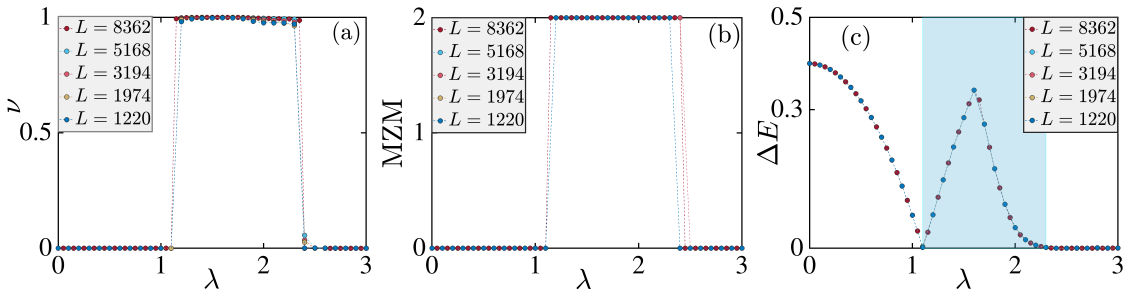

Figure 6.13: The real-space winding number (ν) as a function of λ is shown in (a). The number of Majorana zero modes (MZMs) as a function of λ is shown in (b). The energy bulk gap ΔE as a function of λ is shown in (c). all the plots are shown for $\delta = 0.6$ and various system sizes, mentioned in the figure.

calculate the bulk gap $\Delta E = E_2 - E_1$ in Fig 6.13 (c) where $\Delta E = 0$ represents the gap closing points. Here we show the presence of the topologically non-trivial phase via a shaded region that in blue color.

6.4 Conclusions

In this chapter, we have studied the localization and topological properties of a one-dimensional dimerized Kitaev chain in the presence of an onsite QP potential. The localization properties demonstrate phase transitions from an extended to a critical and hence to a localized phases due to the competition between the dimerization strength and the QP potential strength. One of the prime observations is the existence of the critical phase comprising of two different anomalous mobility edges separating the extended-localized and critical-localized phases. Hence a broad region of the critical states are results in a multifractal phase. Additionally, the topological properties of the model computed via the winding number in real-space and the number of Majorana zero modes existence in

the system, have shown that a moderate value of the QP potential can induce a topologically trivial to a non-trivial (Topological Anderson) phase transition beyond a certain critical dimerization strength. Beyond this, a non-trivial phase will undergo another transition to the Anderson localized phase at large values of the QP potential.

CHAPTER 7

PHASES OF INTERACTING BOSONS IN PRESENCE OF QUASIPERIODIC POTENTIAL

7.1 Introduction

In this chapter, we wish to explore an interacting model in presence of quasiperiodic (QP) potential within a mean-field theory (MFT). We choose interacting bosons loaded in in (optical) lattices which are described by the Bose-Hubbard model (BHM) [135, 168]. The preliminaries of the model are explained elaborately in sec. 2.7. By tuning the system parameters, namely hopping and interparticle interaction a transition from a superfluid (SF) to a Mott insulator (MI) phase can be experimentally observed in a clean environment [169]. Apart from the role of interaction, the interplay of disorder and interaction assumes a crucial role in hosting the new quantum phases in this system. Engineering random disorder using speckle laser beams, multi-component Bose gas or non-commensurate multi-chromatic lattices etc is common, and yield a glassy phase [170, 171, 172, 173, 174] characterized by finite compressibility and vanishing SF order parameter [170, 171, 175, 176, 170, 91, 177], known as the Bose glass phase.

Here instead of a random potential, we include a QP potential which can be contemplated as arising from a two-color sublattice with wavelength, λ_1 and λ_2 that are incommensurate with each other. We investigate how such a QP potential influences the phase diagram of interacting bosons on a lattice. Very recently, the ground state phase diagram of a two-dimensional ultracold Bose gas in optical lattices in presence of QP potential has been studied using quantum Monte Carlo (QMC) [178] and mean-field approximation (MFA) [179, 180] tech-

niques. In addition to the BG phase, they have found signatures of an additional phase, namely, the quasiperiodic induced mixed (QM) phase. It is observed that in the QM phase, majority of the lattice sites belongs to the MI phase while rest of the lattice sites will show finite value of the SF order parameter. Through numeric computation of the site decoupled Bose Hubbard Hamiltonian, we have reconfirmed the presence of such phases. Additionally, we have performed critical state analysis corresponding to the phase transitions.

In this chapter we shall study a system of interacting particles on a 2D optical lattice in presence of a QP potential using MFA. Additionally, the phase transitions are tracked more accurately via percolation theory. Further, we have performed a finite-size scaling analysis to find out the nature of the BG-SF or the QM-SF phase transitions.

The rest of the chapter is organized as follows. First, we describe the model in sec. 7.2 which is followed by the discussion of the results in [sec. 7.3.1-sec. 7.3.5]. Finally we conclude our results in sec. 7.4.

7.2 Model

Here we consider a BHM that describes the general properties of ultracold atoms loaded in a two dimensional (2D) square lattice in the presence of the QP potential. The corresponding Hamiltonian is written as [135, 181, 178],

$$H = -t \sum_{<i,j>} (\hat{a}_i^\dagger \hat{a}_j + h.c.) - \sum_i (\mu - \epsilon_i)\hat{n}_i + \sum_i \frac{U}{2}\hat{n}_i(\hat{n}_i - 1) \tag{7.1}$$

where $\hat{a}_i^\dagger$ ($\hat{a}_i$) denotes the creation (annihilation) operator and $\hat{n}_i$ represents the occupation number operator at site i. t refers the hopping amplitude between

the nearest-neighbor lattice sites, i and j. The particle density can be controlled via the chemical potential μ, while the repulsive on-site interaction strength is denoted by U. Here, ϵ_i represents the two dimensional QP potential at a site in a 2D square lattice, $i \in (n, m)$ which is given by, [178, 179, 180, 182]

$$\epsilon_i = -\lambda\Big(\cos\left[2\pi\beta(n+m)+\alpha\right] + \cos\left[2\pi\beta(n-m)+\alpha\right]\Big) \tag{7.2}$$

where λ denotes the strength of the potential, n, m being the site indices and $\alpha = [0, 2\pi]$ is a phase factor. β determines the periodicity of the QP potential. In our work, we have assumed $\beta = M/L$ where M and L are co-prime integers. Our assumption is based on the continued fraction expansion [183] which allows one to incorporate the periodic boundary conditions on a square lattice, $L \times L$. We choose $\beta = \frac{1}{\sqrt{2}}$, which fixes the possible system sizes to be $L = 55, 99$ and 239 etc [184].

In order to study the phase transition between different quantum phases, we shall employ the MFA to decouple the hopping term as follows [185, 186],

$$\hat{a}_i^\dagger \hat{a}_j \simeq \langle \hat{a}_i^\dagger \rangle \hat{a}_j + \hat{a}_i^\dagger \langle \hat{a}_j \rangle - \langle \hat{a}_i^\dagger \rangle \langle \hat{a}_j \rangle \tag{7.3}$$

where $\langle\ \rangle$ denotes the equilibrium value of an operator and defining the SF order parameter at site i as, $\psi_i = \langle \hat{a}_i \rangle$. Now substituting the superfluid order parameter in Eq.(7.1), the BHM can be written as a sum of single site Hamiltonians as, $H = \sum_i H_i^{MF}$ where,

$$\begin{aligned} H_i^{MF} &= -zt(\phi_i^* \hat{a}_i + h.c.) + zt\phi_i^* \psi_i - (\mu - \epsilon_i)\hat{n}_i + \\ &\quad \frac{U}{2}\hat{n}_i(\hat{n}_i - 1). \end{aligned} \tag{7.4}$$

Here $\phi_i = (\frac{1}{z}) \sum_j \psi_j$ and the sum over j includes all nearest-neighbors of a site i in a square lattice, z is the coordination number.

Randomly chosen initial local order parameters are used to get local ground state by diagonalizing the mean field Hamiltonian [Eq.(7.4)]. This process is repeated at all lattice sites, and hence the state corresponding to the entire lattice generates a global ground state. The self-consistency is checked at each step of the process, until the global order parameters converge within a certain accuracy (in our computation, the accuracy is taken an 0.001). By using the global ground state $|\Psi_G\rangle$ of the Hamiltonian, various physical quantities, such as, the SF order parameter ψ_i, the occupation number, ρ_i, and the compressibility k_i are computed using the following relations,

$$\psi_i = \langle\Psi_G|a_i|\Psi_G\rangle; \;\; \rho_i = \langle\Psi_G|n_i|\Psi_G\rangle; \;\; k_i = \Big[\sum_{i=1}^{L^2}[\rho_i^2 - (\rho_i)^2\Big]. \tag{7.5}$$

In addition to that, the average SF order parameter ($\bar{\Psi}$) and the compressibility ($\bar{\kappa}$) are defined via,

$$\bar{\Psi} = \Big[\Big(\frac{1}{L^2}\Big)\sum_{i=1}^{L^2}\psi_i\Big]_{config}; \;\; \bar{\kappa} = \Big[\Big(\frac{1}{L^2}\Big)\sum_{i=1}^{L^2}[\rho_i^2 - (\rho_i)^2]\Big]_{config} \tag{7.6}$$

where the $config$ in the subscript refers to the fact that results are averaged over different QP realizations within the range $\alpha = [0 : 2\pi]$. To explore the role of a QP potential, here we shall use three representative values implying weak, moderate and strong potential strengths, namely, λ/U to be 0.18, 0.30, and 0.55 [187].

7.3 Results

A phase diagram in a clean system is described in sec. 2.7 where a SF to MI phase transition is observed. In presence of the QP potential, a direct transition from the SF to MI phase is intervene by a BG or QM phases depending on the strength of chemical potential. In the MI phase, each lattice site hosts same

(and integer) number of bosons, and has vanished SF order parameter and compressibility, while the SF phase comprises of non-integer occupation densities, finite superfluid order parameter, and compressibility. A non-integer occupation number emerges corresponding to the BG phase; however, the superfluid order parameter remains zero. On the other hand, the QM phase looks more insulating in nature, and less like the SF phase. Thus it behaves as a pseudo-SF or weak-SF phase.

7.3.1 SF order parameter and compressibility

To understand the critical nature of the BG or the QM phase, and also to locate the transition points separating one quantum phase from another, we shall now study the behaviour of the site average SF order parameter ($\bar{\Psi}$), and the compressibility ($\bar{\kappa}$) for different strengths of QP potential. To this effect, two representative values of the chemical potential are considered, such as, $\mu/U = 0.4$ specifically while focusing on the BG phase, and $\mu/U = 1.0$ for discussing the QM phase. The choice of the values for the chemical potential will becomes clear as we go ahead with the discussion. The variation of $\bar{\Psi}$ and $\bar{\kappa}$ are shown in the Fig.7.1 (a) for BG and Fig.7.1 (b) for QM phases corresponding to $config = 50$ realizations of the QP potential.

For $\mu/U = 0.4$, a small QP strength, that is, $\lambda/U = 0.18$ becomes sufficient to destroy the MI phase and induce the BG phase, resulting in the MI-SF phase transition to occur at a relatively small value of the hopping strength, namely, at $zt_c/U \approx 0.134$ [Fig.7.1 (a)]. With gradual increase of the potential strength, the BG phase now encroaches in between the MI and the SF phases by suppressing

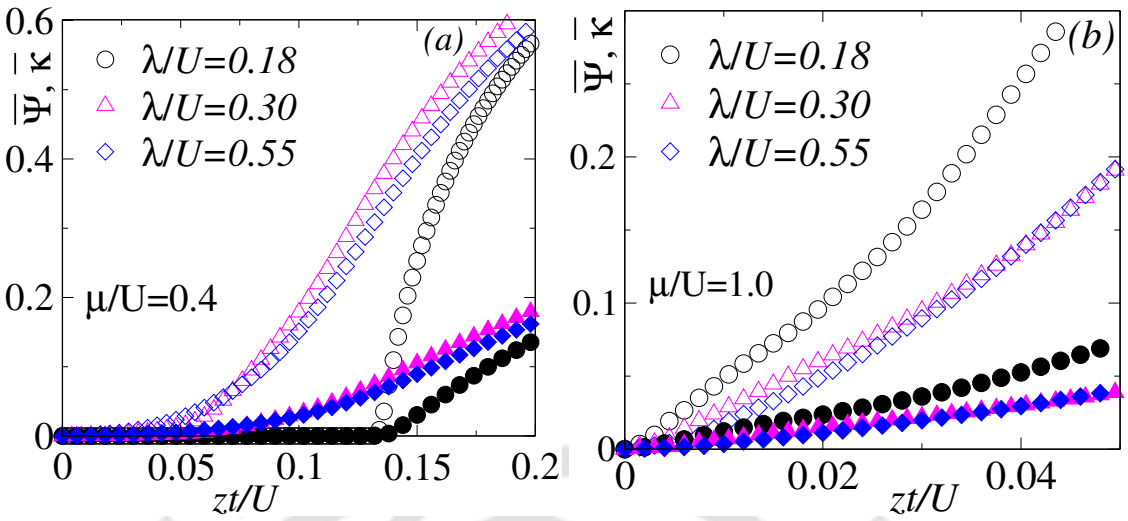

Figure 7.1: The variation of the average SF order parameter $\bar{\Psi}$ (open symbols) and compressibility $\bar{\kappa}$ (filled symbols) are shown in (a) for the MI-BG-SF ($\mu/U = 0.4$) and in (b) for the QM-SF ($\mu/U = 1.0$) phases corresponding to the different QP potential strengths.

the Mott insulating phase, thereby lowering the values for the critical transition point. While a slightly higher value of QP strength almost destroys the MI phase, leaving the system to only consist of the BG and SF phases at $\lambda/U \geq 0.3$.

For $\mu/U = 1.0$, the behavior of $\bar{\Psi}$ and $\bar{\kappa}$ indicate different features in Fig.7.1 (b). In particular, we obtain the SF order parameter, $\bar{\Psi} \approx 0.2$ and the compressibility, $\bar{\kappa} < 0.1$ for $\lambda/U = 0.18$. With increasing λ/U, $\bar{\Psi}$ and $\bar{\kappa}$ become vanishingly small at $zt_c/U \approx 0.04$, thereby pointing towards an insulator like phase. Such a phase seems to be more dominant than the SF phase, and possibly gives an insight on the QM-SF phase transition.

Although by looking at the $\bar{\Psi}$ and $\bar{\kappa}$, one can get the qualitative information about the critical zt_c/U separating different quantum phases. However, it fails to provide more information about the appearance of the QM phase, and precisely locate the the critical tunneling strengths for the phase transitions. Thus

we suggest of a more elegant technique, namely, the percolation technique by introducing a new quantity, namely, indicator in the following subsection.

7.3.2 Indicators of MI, BG, QM and SF phases

General conclusions achieved from $\bar{\Psi}$ and $\bar{\kappa}$ indicate that it is reasonable to define an indicator (χ) as [188, 189]

$$\chi = \frac{\text{sites with } \psi_i \neq 0 \text{ and } \rho_i \neq \textit{integer}}{\text{total number of sites}}. \tag{7.7}$$

In addition, we can also define another quantity, namely $\tilde{\chi}$ by changing the numerator of the above Eq.(7.7) to the ″sites with $\psi_i = 0$ *and* $\rho_i =$ integer″. These definitions imply that the MI phase corresponds to $\tilde{\chi} = 1$, while the SF phase is characterized by $\chi = 1$. Any intermediate value, such as $0 < \chi < 1$ signifies the presence of the BG phase. For numerical convergence, we have set the tolerance of $\psi_i < O(10^{-1})$ and $\rho_i = m \pm \delta$, where $\delta \sim O(10^{-3})$ and m is an integer for the MI phase. The variation of χ and $\tilde{\chi}$ for the parameters discussed above are shown as a function of zt/U in Fig. 7.2 (a) for $\mu/U = 0.4$, and Fig. 7.2 (b) for $\mu/U_0 = 1.0$.

For $\mu/U = 0.4$, it is observed that the MI phase exists up to a value $zt/U \approx 0.132$ corresponding to $\lambda/U = 0.18$ [Fig. 7.2(a)]. Similar numbers have been inferred from the plots of the average SF order parameter, and the compressibility as well. Beyond these critical hopping strengths, the values of ρ_i turn from integer to fractions, giving rise to the SF phase characterized by finite values of ψ_i. With increasing the potential strength to $\lambda/U = 0.3$, it is seen that, χ becomes finite at a lower value, that is, of $zt/U = 0.028$. Further rise to $\lambda/U \geq 0.55$, the presence of the BG phase is stabilized over a broader region with larger values of zt/U. Also, the MI phase corresponds to a narrow region of $zt/U \simeq 0.020$

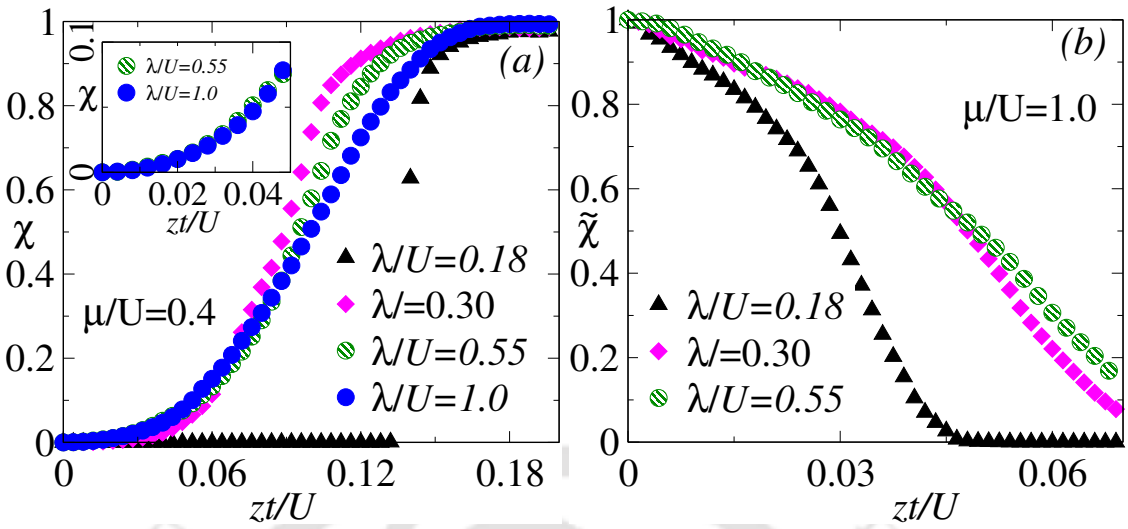

Figure 7.2: The variation of the indicator as a function of the hopping strength zt/U is shown in (a) for the MI-BG-SF ($\mu/U = 0.4$) and (b) for the QM-SF ($\mu/U = 1.0$) phases corresponding to the different QP potential strengths.

which is shown in Fig. 7.2 (a) (inset). Thus the MI phase becomes unstable in presence of a large QP potential, since the order parameters at individual site delocalize across the lattice, thereby resulting in the presence of only BG and SF phases.

For the other choice of the chemical potential, that is, $\mu/U = 1.0$, we have plotted $\tilde{\chi}$ (instead of χ) to access the signature of the QM phase corresponding to different values of the potential strengths. It shows that $\tilde{\chi} \neq 0$ till $zt/U \approx 0.046$ for $\lambda/U = 0.18$, and with QP strength increasing up to $\lambda/U \geq 0.3$, one gets $\tilde{\chi} \neq 0$ at higher values of zt/U [Fig. 7.2(b)]. This implies that the insulating phase is now distributed over a large region of the parameter space, thus paving the way for the appearance of the QM phase. The QM phase behaves mostly like an insulating phase, with very weak superfluid character. Thus one can expect that the majority of the lattice sites will host integer occupation densities, except for a tiny region where strong particle correlations will exist. Consequently, we

infer that the QM phase corresponds to $\tilde{\chi} > 0.5$ with a patch of the SF region.

The above observations suggest that the determination of a precise transition point from the MI-BG phase can be done via χ or $\tilde{\chi}$. But the presence of the QM phase, and hence determination of the BG-SF or the QM-SF phase boundaries remain challenging. We shall turn our attention to the percolation analysis to overcome these hurdles in the next subsection.

7.3.3 Percolation appearance and cluster size distribution

Since we are interested in the BG and the QM phases, our primary focus will be on the BG-SF and the QM-SF phase transitions, and hence compute the critical points to enumerate the nature of the BG and the QM phases. The BG phase constitutes of a number of isolated SF clusters that are surrounded by the MI clusters. The SF cluster is an island that is formed by the non-integer occupation densities, while the MI cluster is formed with sites having integer occupation densities. Thus the onset of superfluidity begins when these separated SF clusters coalesce together to percolate or span through the entire lattice for the first time. The QM phase hosts a situation where the majority of the lattice sites belong to the MI cluster, with at least one SF percolating cluster. Therefore, our requirements culminate into finding out the first percolating cluster exhibited in the SF phase corresponding to both the types of potential.

To facilitate a visual understanding, we show the real space density plots, ρ_i are shown in Fig. 7.3 corresponding to a single realization of the QP potential, for $\lambda/U = 0.2$. The light green circles indicate ρ_i =integer, while the red circles are for ρ_i ≠integer values. The horizontal (vertical) axis is the lattice site along

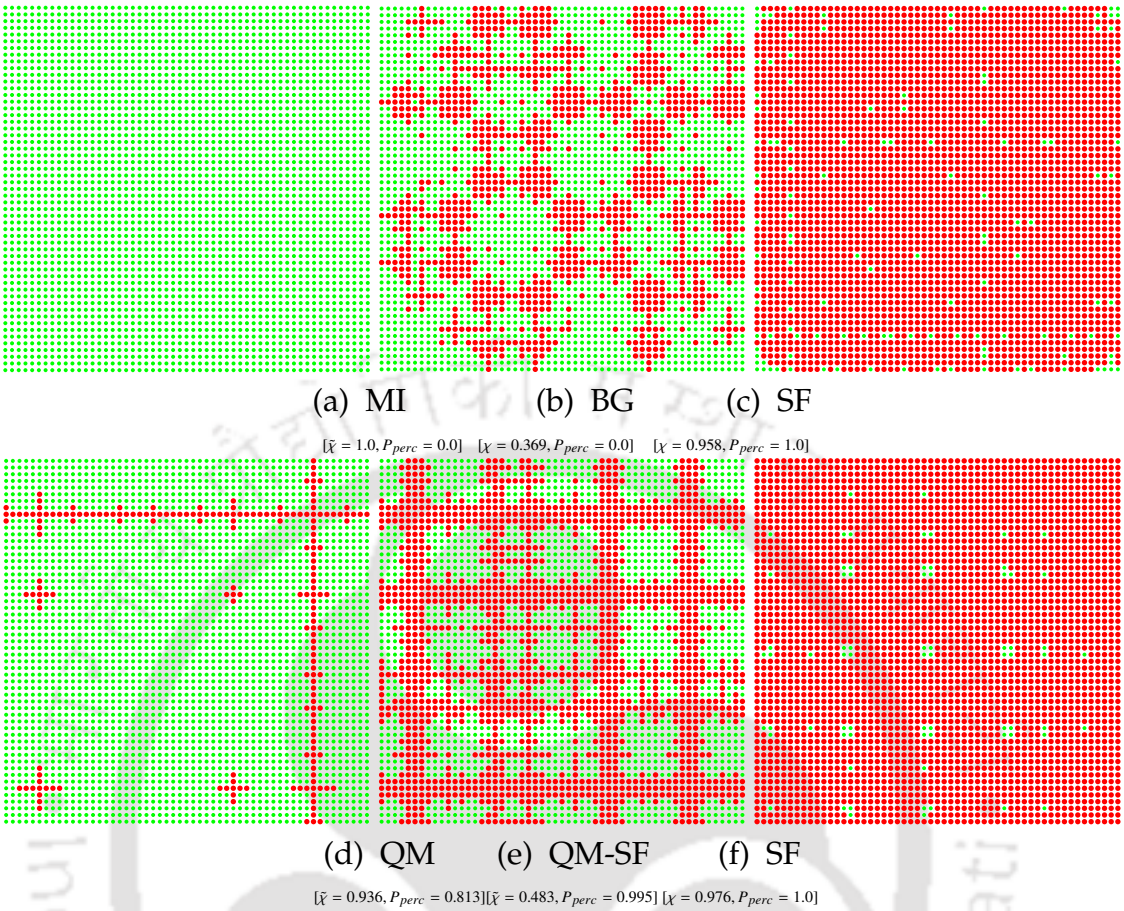

Figure 7.3: The real space plots of the occupation densities, ρ_i for lattice size $L \times L = 55 \times 55$ for the MI, QM, BG and SF phases corresponding to QP potential, $\lambda/U = 0.2$. Top row shows the phase evolution from MI ($zt/U = 0.0$) (a) - BG ($zt/U = 0.101$) (b) - SF ($zt/U = 0.12$) (c) at $\mu/U_0 = 0.4$. Bottom row shows the phase evolution from QM ($zt/U = 0.005$) (d) - Near QM-SF ($zt/U = 0.025$) (e) - SF ($zt/U = 0.04$) (f) at $\mu/U_0 = 1.0$.

the x (y) direction. In all the three cases, there is a clear evolution from one quantum phase to another. Let us discuss them below.

Fig. 7.3 (top row) shows the phase evolution from MI ($zt/U = 0.0$) (a) - BG ($zt/U = 0.1$) (b) - SF ($zt/U = 0.12$) (c) at $\mu/U_0 = 0.4$ for $\lambda/U = 0.2$. The MI phase in (a) gradually transforms into the BG phase, having scattered or island-like SF clusters that are surrounded by the MI clusters (b). Finally these SF clusters

percolate into the superfluid phase resulting the formation of a spanning cluster across the lattice (c).

Fig. 7.3 (bottom row) displays the phase evolution from QM ($zt/U = 0.005$) (d) - near QM-SF ($zt/U = 0.025$) (e) - SF ($zt/U = 0.04$) (f) at $\mu/U_0 = 1.0$ for $\lambda/U = 0.2$. In Fig. 7.3(d), one can easily understand that the majority of the lattice sites with $\tilde{\chi} > 0.5$ remain in the MI phase, while there is one SF percolating cluster, which is essentially the signature of the QM phase. Subsequently, this QM phase gradually transforms into the SF phase, whence one or more SF percolating clusters appear with $\tilde{\chi} < 0.5$ from a region near the QM-SF phase (e) to the SF phase (f).

In order to understand the QM and BG phases more rigorously, and to get an idea of the first percolating cluster, that we shall compute the mean cluster size which is defined as [190],

$$M_{cs}(\chi) = \frac{\sum_p^{\infty} p^2 s_p(\chi)}{\sum_p^{\infty} p s_p(\chi)} \tag{7.8}$$

where $ps_p(\chi)$ represents the total number of the occupied sites corresponding to the p-th cluster, with the percolating clusters are not included in the sum. Here, we shall employ the well known Hoshen-Kopelman algorithm that is mostly used in percolation problems. It works under the union-find principle to compute the the SF cluster formation [191].

The variation of M_{cs} corresponding to different lattice sizes is shown for the BG-SF in Fig. 7.4(a-b), and the QM-SF phase transitions in Fig. 7.4(c) for $\lambda/U = 0.55$. For BG-SF phase corresponding to $\mu/U = 0.35$, M_{cs} increases as a function of χ and attains a maximum at a critical value, $\chi_c(L)$ [Fig. 7.4]. Beyond this, $\chi_c(L)$, M_{cs} starts to decrease hinting at the formation of the first percolating cluster across the lattice. This behaviour seems to be analogous to that of

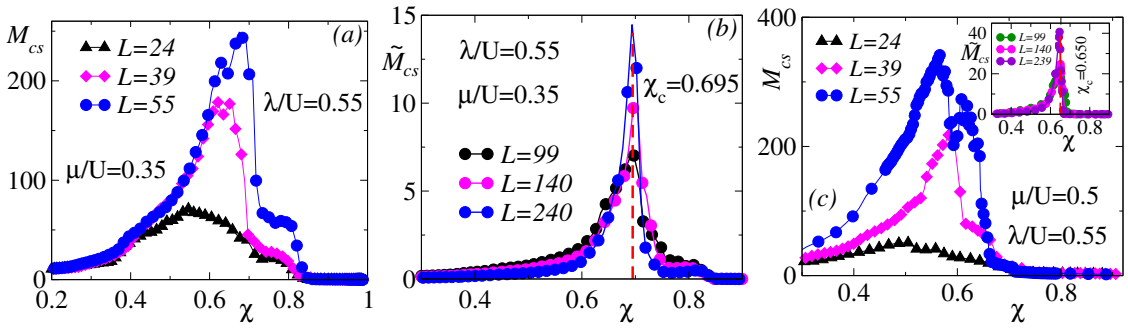

Figure 7.4: The Mean cluster size, M_{cs} in (a) and $\tilde{M}_{cs} = M_{cs}/L$ in (b) for the BG-SF phase and the QM-SF phase in (c) as a function of χ corresponding to the different lattice size.

the 2D random percolation problem, where M_{cs} attains a peak value at a critical threshold $\chi_c(L \to \infty) = 0.592$. Thus we can infer that the values of $\chi_c(L)$ are 0.546 , 0.621, and 0.674, and thus it moves away from the critical point $\chi_c(L \to \infty)$ [Fig. 7.4(a)] with increasing system sizes. Here the corresponding system sizes are chosen as $L = 24, 39$, and 55 respectively for the QP potential. This clearly indicates that the system experiences a finite size effect which we discuss in the next section.

We have shown the mean cluster size for QM-SF phase transition corresponding to $\mu/U = 0.5$ in Fig. 7.4(c) for $\lambda/U = 0.55$. For $\mu/U = 0.5$ [Fig. 7.4(c)], M_{cs} is nearly symmetric with respect to variation in χ, and the overall behaviour remains similar to that of the BG-SF phase as shown in Fig. 7.4(a-b). It attains a maximum value at $\chi_c(L) = 0.513,\ 0.583,$ and 0.567 for the system sizes stated above, which is again a value close to $\chi_c(L \to \infty)$.

However, the re-scaled mean cluster size, that is, $\tilde{M}_{cs} = M_{cs}/L$ shows that all the curves overlap onto each other, and become maximum at a single critical point, namely, $\chi_c(L \geq 99) = 0.695$ for the BG-SF [Fig. 7.4(b)] and $\chi_c(L \geq 99) = 0.650$ for the QM-SF [Fig. 7.4(c)(inset)] phase transitions for large system sizes.

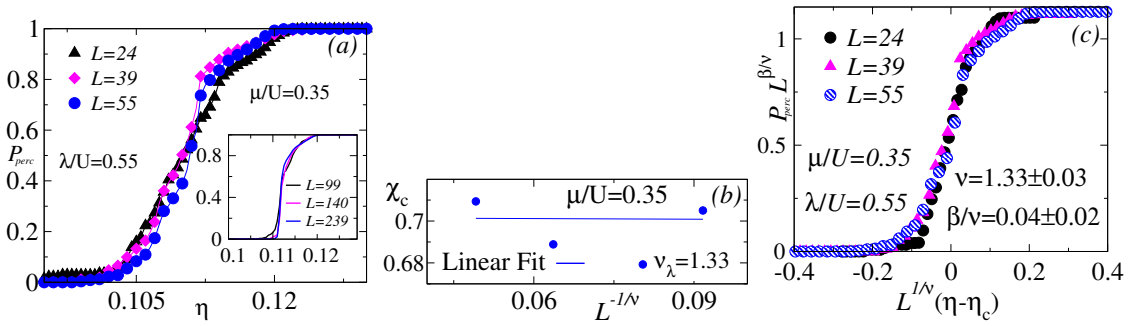

Figure 7.5: The percolation probability, P_{perc} as a function of $\eta = zt/U$ in the BG-SF phase for different lattice size corresponding to QP in (a). $\chi_c(L)$ vs $L^{-1/\nu}$ plot for QP and random potential in (b). Finite-size scaling for QP potential is shown in (c).

This implies there is no explicit finite size dependence of the system for $L \geq 99$.

7.3.4 Finite-size scaling and critical exponents

Endowed with the understanding of the mean cluster size, and how to deal with the finite size effects, it is therefore necessary to look into the extent of the percolating cluster in real space at the onset of the BG-SF or QM-SF phases. For that purpose, we define another quantity, P_{perc} via [190, 192, 193],

$$P_{perc} = \frac{\text{Sites in a spanning cluster}}{\text{Total number of occupied sites}}. \tag{7.9}$$

It is expected that the $P_{perc} = 0$ in both the MI and the BG phases, while $P_{perc} \neq 0$ for the SF and the QM phases. To explore the finite size effects, the variation of P_{perc} is shown in Fig. 7.5 for the BG-SF phase, and Fig. 7.6 for the QM-SF phase corresponding to different system sizes, L by considering $config =$ 100 different realizations.

For the BG-SF phase, we have shown P_{perc} as a function of zt/U (say, $\eta =$

zt/U) for $\lambda/U = 0.55$ and $\mu/U = 0.35$ in Fig. 7.5(a). It shows that all the three curves pass through a critical point, namely, $\eta_c \approx 0.1105$ for a smaller system size, namely, $L \leq 55$. Thus the finite-size effects can be taken care by using a universal scaling form.

At the critical point, η_c, P_{perc} follows a scaling behavior, which may be assume as, [190, 192, 193],

$$P_{perc}(L, \eta) = L^{-\beta/\nu} \tilde{p}(\eta - \eta_c) L^{1/\nu} \tag{7.10}$$

where $\tilde{p}$ is the universal scaling function, and β, ν are the critical exponents. By choosing proper values of β, ν, and with the values η_c obtained earlier, the observables show a length invariant behaviour, where different curves collapse on to each other which validates the existence of a universal scaling function (see Eq. 7.10). It can be shown that the average size $\langle S_m \rangle$ of the SF percolating cluster varies with system size, L at the percolation threshold (χ_c) via, $\langle S_m \rangle \approx L^{d_f}$ where d_f is the fractal dimension of the SF percolating cluster. It is related to the critical exponents and the system dimension d through $d_f = d - \beta/\nu$ [190, 192, 193].

In order to find a suitable value of the exponent ν, we need to locate $\chi_c(L)$ at which a spanning cluster appears for the first time. This can be obtained through the mean value of the distribution defined by the derivative of P_{perc} with respect to χ, namely, $\frac{dP_{perc}}{d\chi(\eta)}$ via $\chi_c(L) = \int_0^1 \chi \frac{dP_{perc}}{d\chi} \propto L^{-1/\nu}$, where $\chi_c(L)$ can be identified as the value for which $\frac{dP_{perc}}{d\eta}$ corresponds to a maximum.

We have plotted $\chi_c(L)$ against $L^{-1/\nu}$, and found that the best straight line fit is observed for $\nu_\lambda = 1.33 \pm 0.03$ for the QP potential [Fig. 7.5 (b)]. Such a value is again close to one corresponding to the random potential in 2D obtained via QMC studies [190, 194]. Finally, having obtained ν and η_c values and choosing

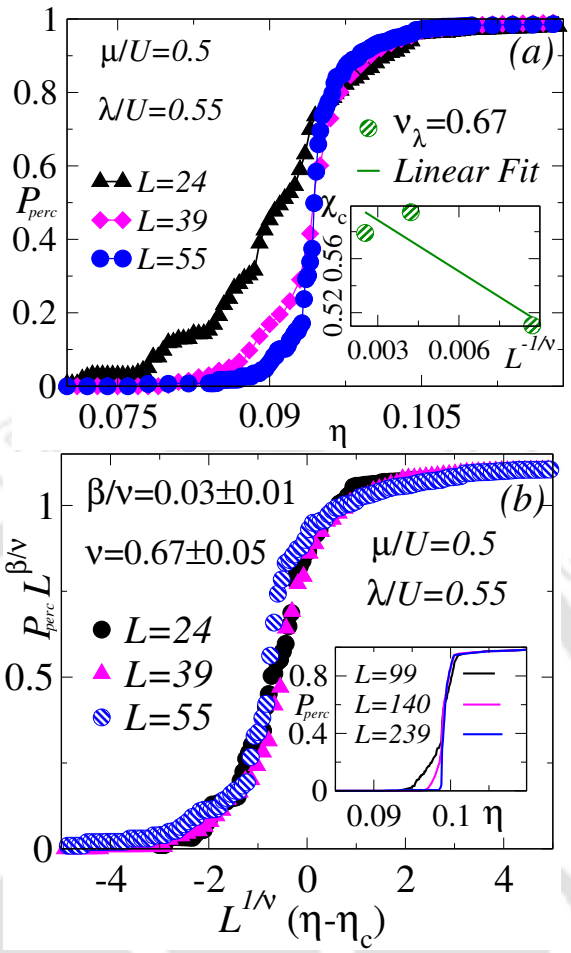

Figure 7.6: The Percolation probability, P_{perc} as a function of $\eta = zt/U$ in the QM-SF phase for different lattice sizes in (a) and finite-size scaling in (b) for QP potential.

$\beta/\nu = 0.04 \pm 0.02$, a suitable data collapse is observed [Fig. 7.5(c)]. Subsequently, the fractal dimension, d_f appears to be $d_f \approx 1.96 \pm 0.02$. Therefore, we can conclude that, the phase transitions from the BG to the SF phase belong to the same universality class for the QP potential.

For the QM-SF phase, the variation of P_{perc} with $\eta = zt/U$ is shown in Fig. 7.6(a) for $\mu/U = 0.5$ at $\lambda/U = 0.55$. Here, all the three curves cross at the critical hopping strength given by $\eta_c \approx 0.0963$ [Fig. 7.6(a)]. $\chi_c(L)$ against $L^{-1/\nu}$ plot shows a best fit straight line for $\nu_\lambda = 0.67 \pm 0.05$ [Fig. 7.6(a)(inset)]. With

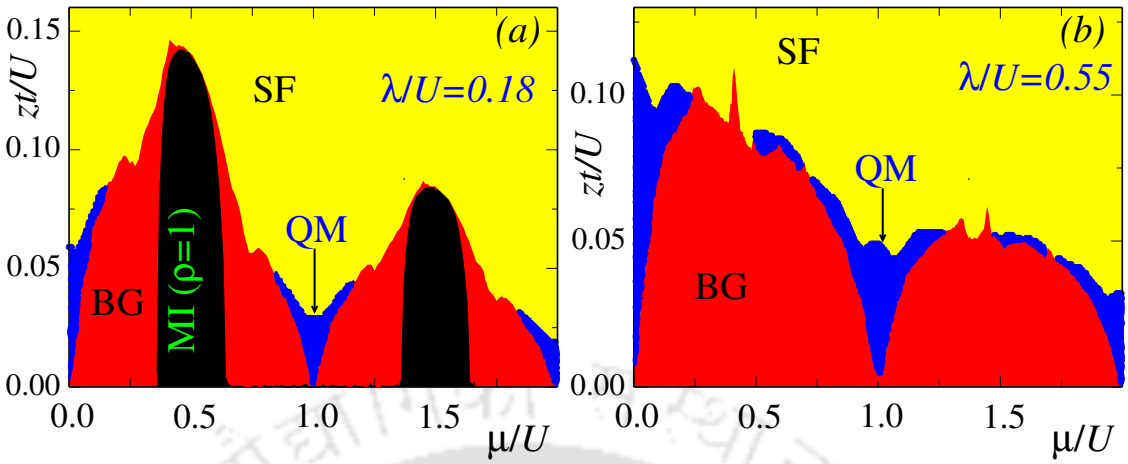

Figure 7.7: Phase diagrams (top row) are shown for (a) $\lambda/U = 0.18$, and (b) $\lambda/U = 0.55$ corresponding to QP potential.

these value of ν, and $\beta/\nu = 0.03 \pm 0.01$, we have achieved a perfect data collapse for the QM-SF phase [Fig. 7.6(b)]. The value of such a critical exponent (ν) calculated using our percolation based mean field approach agrees very well with that from the QMC results obtained in Ref.[178] for the QM-SF phase transition. Moreover, the phase transition from the QM-SF phase belongs to a different universality class as that for the BG-SF phase transition.

For large system sizes, all the curves collapse onto each other, thereby justifying that a further scaling is not required for the BG-SF [Fig. 7.5(a)(inset)], and the QM-SF phase transitions [Fig. 7.6(b)(inset)] for $L \geq 99$.

7.3.5 Phase Diagram

The quantum phases can be characterized based on the SF percolating cluster which is summarized in Table 7.1. The resultant phase diagrams in the $\mu - zt$ plane are shown in Fig. 7.7 where we have only scanned up to the second MI

lobe for $config = 30$ realizations.

	MI	QM	BG	SF
$1^*\chi\ (\tilde{\chi})$	$\tilde{\chi} = 1$	$\tilde{\chi} > 0.5$	$0 < \chi < \chi_c$	$\chi_c \leq \chi \leq 1$
1^*P_{perc}	0	$\neq 0$	0	$\neq 0$

Table 7.1: Characterization of the quantum phases based on $\chi\ (\tilde{\chi})$ and P_{perc}

For $\lambda/U = 0.18$, the phase diagram consists of all four phases, such as, the MI, BG, QM and the SF phases which are marked by different colours in Fig. 7.7(a). The BG phase portrays a lobe structure similar to the MI lobe, and the chemical potential is now shifted by an amount $\pm 2\lambda/U$ on either side of the MI lobes. Apart form the BG phase, we have also found the signature of the QM phase, which forms like an envelope over the BG phase for small values of μ/U. The feature is more pronounced at $\mu/U = 1$, which is a degenerate point between the two consecutive MI lobes.

With increasing strength of the QP potential, the MI phase becomes more vulnerable, and the BG phase completely destroys the insulating phase at a critical value, $\lambda_c/U = 0.25$. Further rise in the strength of the potential, for example to a value $\lambda/U = 0.55$, the system consists of all the phases, except the MI phase, and the regions spanned by the BG and the QM phases dominate due to the localization effects [Fig. 7.7(b)]. Thus the QM phase behaves as a pseudo or a weak superfluid (wSF) phase and stabilizes with increasing QP strengths. All these phase diagrams are in qualitative agreement with the QMC [178] and the MFA results obtained in Ref.[179, 180], where the signature of the QM phase, namely, the wSF or the weak BG (wBG) is also observed, and the wSF phase seems to stabilize at larger values of λ/U.

7.4 Conclusions

In conclusion, we have studied a two-dimensional Bose-Hubbard model in presence of a quasiperiodic (QP) potential and realized the emergence of various quantum phases, such as MI, BG, QM, and the SF phase in the phase diagram. A site decoupling mean field approach (MFA) aided by the percolation scenario is used to track various transition points accurately. While, as expected, the QP potential intervenes between the MI and the SF phases, a new phase more like the insulating phase, denoted as the QM phase is realized. In addition, a finite-size scaling analysis is performed and universal scaling relation is obtained. The critical exponents reveal that the BG to the SF and the QM to SF phase transition belong to a different universality classes. Besides, no explicit finite-size dependence for large system sizes has been observed. We have found that our critical exponents are in good agreements with those obtained from the QMC results.

CHAPTER 8

CONCLUSIONS

The electronic transport properties in disordered systems have been an intense subject of study in physics through the years. The theoretical and experimental inquiries of solid-state materials result in an unavoidable property, namely the presence of disorder, which begets the localization phenomenon. After the discovery of the localization transition by P. W. Anderson in random potential systems, the topic became a fundamental prototype in several arenas of condensed matter physics due to its novel applicabilities not only in solids but also in sound, light, and ultracold atomic gases. One of the significant consequences of the localization phenomenon is a metal-insulator transition in three dimensions, which is an example of a quantum phase transition. However, it was soon realized that a system suffers a complete localization in one and two dimensions at an infinitesimal disorder, thereby demonstrating no phase transition. Such a transition is only possible in three dimensions. On the contrary, this localization transition is possible to achieve in the one-dimensional system in presence of quasiperiodic (QP) potential. Such potential is a key ingredient of this thesis.

A theoretical model to study the QP potential is the Aubry-André (AA) model. The model shows a sharp localization transition in a one-dimensional system, thereby exhibiting no evidence of mobility edge (ME). However, there is a possibility to observe ME in a quantum system in presence of QP potential by destroying the self-dual symmetry, which is one of the fundamental properties of the AA model. Among several possibilities of breaking this symmetry, we particularly choose a dimer model. Thus, the presence of intra-cell and inter-cell hopping in a one-dimensional chain, popularly known as the Su-Schriffer-

Hegger (SSH) model, suits our purpose. In addition, this model has intriguing topological characteristics, which have been studied as an example of a paradigmatic model of a topological insulator. Thus motivated by these two aspects, such as localization properties due to the QP potential and topological properties in the dimer model, we set our theoretical background to investigate further into the metal insulator transition and beyond.

To begin with, we consider the SSH model in presence of QP potential at the two sites in a unit cell. The strength of the potential applying to both the sublattices is equal and opposite, termed as staggered disorder case. According to common wisdom, it is known that once the localization sets in, it remains localized as a function of disorder strength. However, our observation contradicts this behavior. In the staggered disordered case, the system hosts the first localization transition corresponding to a potential strength, hence inducing a complete localization. By increasing the potential strength further, some of the eigenstates become extended again, resulting in occurrence of ME in the system. Finally, at a large value of the potential strength, the system undergoes another localization transition, and eventually at very large potential strengths, one encounters a complete localization. Therefore, we infer that our system hosts a reentrant localization transition as a function of QP potential strength corresponding to a specific range of the dimerization strength due to the competition between them. The observations are performed via participation ratio, eigenenergies, density of states, and finite-size scaling analysis.

In the next chapter, we have explored the critical behavior associated with the reentrant phase transition observed in the model discussed in the previous paragraph. In particular, the reentrant transition occurs through two intermedi-

ate (critical) phases hosting MEs. Hence, we have investigated the eigenstates that belong to these critical phases by performing multifractal analysis. In addition, four transitions occur from an extended → intermediate → localized → intermediate→ localized phases as a function of the QP potential strength through four critical points. Using the critical state analysis, we are able to compute the critical potential strengths and critical exponents corresponding to the first, second, and third transitions. However, due to the quantum fluctuation of the observables, the fourth critical point was hand to find. Moreover, it was noticeable that the second and third phase transitions belong to the same universality class. In addition to the analysis of the eigenstates, we have also explored the eigenenergies at the two critical regions by computing the Hausdorff dimension. The results indicated distinct values of this quantity, namely the Hausdorff dimension corresponding to both these regions.

The onsite QP potential in the SSH model is unable to preserve its topological properties by energizing the zero energy edge modes. Hence the sublattice (chiral) symmetry disappears. Thus, until now, we have not encountered any topological properties in our system. In our next chapter, we aim to bring back the discussion of the topological properties of the SSH model in presence of onsite QP potential. In order to do that, we have incorporated p-wave superconducting correlations in our model. Consequently, the model shows a topological nature due to particle-hole symmetry, which is intrinsic in the superconductor. The theoretical model to study the p- wave superconductor is known as the Kitaev chain model. This model is particularly interesting for its application in quantum computation. Our model thus becomes a hybrid model comprising of a one-dimensional SSH chain and the Kitaev chain, known as the dimerized Kitaev chain model. In this chapter, our aim is to study the localization and

the topological properties of the dimerized Kitaev chain model in presence of QP potential. In the analysis of the localization properties via participation ratio, fractal dimension, and level spacing, the system hosts several phase transitions from extended to intermediate/critical, subsequently critical to localized, as a result of the competition between the dimerization and the QP potential strength. In addition, we have observed that the critical phase comprising of two distinct anomalous MEs. While one of the anomalous ME appears between the extended and localized states, the other one separates multifractal states from the localized one, resulting in hosting a multifractal phase. Moreover, we have studied the topological properties of this model via computing the real-space winding number as the topological invariant and the number of Majorana zero modes. It is illustrated that the system exhibits a phase transition from a topologically trivial to a non-trivial, that is, a topological Anderson phase as a function of QP potential beyond a specific critical dimerization strength. Finally, at a large value of the QP potential, the system undergoes another transition from the topological Anderson phase to the Anderson localized phase.

To go beyond the paradigm of the non-interacting one-dimensional systems, we also have explored a two-dimensional interacting system in our last chapter. Here, we have studied interacting bosons in a square lattice in presence of QP potential using mean-field theory (MFT). There are several phases, such as Mott-insulator (MI) and superfluid (SF), in addition to the Bose-glass (BG) and a new phase known as the quasiperiodically induced mixed phase (QM), are observed in the phase diagram. Using the percolation analysis aided by the finite-size scaling analysis, we have calculated the critical transition point and critical exponents corresponding to the BG to the SF and the QM to the SF phase transition.

We believe that our findings on the effects of the QP potential on different quantum models, and the critical analysis performed in this thesis shall initiate further studies to unravel more information on the subject.

BIBLIOGRAPHY

[1] Juliette Billy, Vincent Josse, Zhanchun Zuo, Alain Bernard, Ben Hambrecht, Pierre Lugan, David Clément, Laurent Sanchez-Palencia, Philippe Bouyer, and Alain Aspect. Direct observation of anderson localization of matter waves in a controlled disorder. *Nature*, 453(7197):891–894, 2008.

[2] Aart Lagendijk, Bart Van Tiggelen, and Diederik S Wiersma. Fifty years of anderson localization. *Phys. today*, 62(8):24–29, 2009.

[3] Immanuel Bloch. Ultracold quantum gases in optical lattices. *Nature physics*, 1(1):23–30, 2005.

[4] Giacomo Roati, Chiara D'Errico, Leonardo Fallani, Marco Fattori, Chiara Fort, Matteo Zaccanti, Giovanni Modugno, Michele Modugno, and Massimo Inguscio. Anderson localization of a non-interacting bose–einstein condensate. *Nature*, 453(7197):895–898, 2008.

[5] Christian Aulbach, André Wobst, Gert-Ludwig Ingold, Peter Hänggi, and Imre Varga. Phase-space visualization of a metal–insulator transition. *New Journal of Physics*, 6(1):70, 2004.

[6] H Eugene Stanley. Scaling, universality, and renormalization: Three pillars of modern critical phenomena. *Reviews of modern physics*, 71(2):S358, 1999.

[7] Arnab Kumar Pariari. Atoms to topological electronic materials: A bedtime story for beginners. *Indian Journal of Physics*, 95(12):2639–2660, 2021.

[8] Noor Sk Nabi. Quantum phases of a spin-1 bose gas in an optical lattice: A focus on mean field and perturbative approaches. *Thesis*, 2018.

[9] F. Bloch. Über die quantenmechanik der elektronen in kristallgittern. *Zeitschrift für physik*, 52(7):555–600, 1929.

[10] P. W. Anderson. Absence of diffusion in certain random lattices. *Phys. Rev.*, 109:1492–1505, Mar 1958.

[11] E. Abrahams, P. W. Anderson, D. C. Licciardello, and T. V. Ramakrishnan. Scaling theory of localization: Absence of quantum diffusion in two dimensions. *Phys. Rev. Lett.*, 42:673–676, Mar 1979.

[12] P. A. Lee and T. V. Ramakrishnan. Disordered electronic systems. *Rev. Mod. Phys.*, 57:287–337, Apr 1985.

[13] B. Kramer and A. MacKinnon. Localization: theory and experiment. *Reports on Progress in Physics*, 56(12):1469, 1993.

[14] Michele Modugno. Exponential localization in one-dimensional quasi-periodic optical lattices. *New Journal of Physics*, 11(3):033023, mar 2009.

[15] J. Biddle, B. Wang, D. J. Priour, and S. Das Sarma. Localization in one-dimensional incommensurate lattices beyond the aubry-andré model. *Phys. Rev. A*, 80:021603, Aug 2009.

[16] Xiao Li, Xiaopeng Li, and S. Das Sarma. Mobility edges in one-dimensional bichromatic incommensurate potentials. *Phys. Rev. B*, 96:085119, Aug 2017.

[17] J.B Sokoloff. Unusual band structure, wave functions and electrical conductance in crystals with incommensurate periodic potentials. *Physics Reports*, 126(4):189–244, 1985.

[18] Serge Aubry and Gilles André. Analyticity breaking and anderson localization in incommensurate lattices. *Ann. Israel Phys. Soc*, 3(133):18, 1980.

[19] P G Harper. Single band motion of conduction electrons in a uniform magnetic field. *Proceedings of the Physical Society. Section A*, 68(10):874–878, oct 1955.

[20] Douglas R Hofstadter. Energy levels and wave functions of bloch electrons in rational and irrational magnetic fields. *Physical review B*, 14(6):2239, 1976.

[21] L. Sanchez-Palencia and L. Santos. Bose-einstein condensates in optical quasicrystal lattices. *Phys. Rev. A*, 72:053607, Nov 2005.

[22] X Deng, S Ray, S Sinha, GV Shlyapnikov, and L Santos. One-dimensional quasicrystals with power-law hopping. *Phys. Rev. Lett.*, 123(2):025301, 2019.

[23] Attila Szabó and Ulrich Schneider. Non-power-law universality in one-dimensional quasicrystals. *Phys. Rev. B*, 98(13):134201, 2018.

[24] Sthitadhi Roy, Ivan M. Khaymovich, Arnab Das, and Roderich Moessner. Multifractality without fine-tuning in a Floquet quasiperiodic chain. *SciPost Phys.*, 4:25, 2018.

[25] Taylor Cookmeyer, Johannes Motruk, and Joel E. Moore. Critical properties of the ground-state localization-delocalization transition in the many-particle aubry-andré model. *Phys. Rev. B*, 101:174203, May 2020.

[26] Archak Purkayastha, Abhishek Dhar, and Manas Kulkarni. Nonequilibrium phase diagram of a one-dimensional quasiperiodic system with a single-particle mobility edge. *Phys. Rev. B*, 96:180204, Nov 2017.

[27] Ashirbad Padhan, Mrinal Kanti Giri, Suman Mondal, and Tapan Mishra. Emergence of multiple localization transitions in a one-dimensional quasiperiodic lattice. *Phys. Rev. B*, 105:L220201, Jun 2022.

[28] Miguel Gonçalves, Bruno Amorim, Eduardo Castro, and Pedro Ribeiro. Hidden dualities in 1d quasiperiodic lattice models. *SciPost Physics*, 13(3):046, 2022.

[29] S. Das Sarma, Akiko Kobayashi, and R. E. Prange. Proposed experimental realization of anderson localization in random and incommensurate artificially layered systems. *Phys. Rev. Lett.*, 56:1280–1283, Mar 1986.

[30] J. Biddle and S. Das Sarma. Predicted mobility edges in one-dimensional incommensurate optical lattices: An exactly solvable model of anderson localization. *Phys. Rev. Lett.*, 104:070601, Feb 2010.

[31] Sriram Ganeshan, J. H. Pixley, and S. Das Sarma. Nearest neighbor tight binding models with an exact mobility edge in one dimension. *Phys. Rev. Lett.*, 114:146601, Apr 2015.

[32] M. L. Sun, G. Wang, N. B. Li, and T. Nakayama. Localization-delocalization transition in self-dual quasi-periodic lattices. *EPL (Europhysics Letters)*, 110(5):57003, jun 2015.

[33] Sarang Gopalakrishnan. Self-dual quasiperiodic systems with power-law hopping. *Phys. Rev. B*, 96:054202, Aug 2017.

[34] Archak Purkayastha, Abhishek Dhar, and Manas Kulkarni. Nonequilibrium phase diagram of a one-dimensional quasiperiodic system with a single-particle mobility edge. *Phys. Rev. B*, 96:180204, Nov 2017.

[35] Fangli Liu, Somnath Ghosh, and Y. D. Chong. Localization and adiabatic pumping in a generalized aubry-andré-harper model. *Phys. Rev. B*, 91:014108, Jan 2015.

[36] J. Biddle and S. Das Sarma. Predicted mobility edges in one-dimensional incommensurate optical lattices: An exactly solvable model of anderson localization. *Phys. Rev. Lett.*, 104:070601, Feb 2010.

[37] Yucheng Wang, Xu Xia, Long Zhang, Hepeng Yao, Shu Chen, Jiangong You, Qi Zhou, and Xiong-Jun Liu. One-dimensional quasiperiodic mosaic lattice with exact mobility edges. *Phys. Rev. Lett.*, 125(19):196604, 2020.

[38] Attila Szabó and Ulrich Schneider. Mixed spectra and partially extended states in a two-dimensional quasiperiodic model. *Phys. Rev. B*, 101:014205, Jan 2020.

[39] Xiao Li, Xiaopeng Li, and S. Das Sarma. Mobility edges in one-dimensional bichromatic incommensurate potentials. *Phys. Rev. B*, 96:085119, Aug 2017.

[40] J. Biddle, D. J. Priour, B. Wang, and S. Das Sarma. Localization in one-dimensional lattices with non-nearest-neighbor hopping: Generalized anderson and aubry-andré models. *Phys. Rev. B*, 83:075105, Feb 2011.

[41] Xiao Li and S. Das Sarma. Mobility edge and intermediate phase in one-dimensional incommensurate lattice potentials. *Phys. Rev. B*, 101:064203, Feb 2020.

[42] Alexander Duthie, Sthitadhi Roy, and David E. Logan. Self-consistent theory of mobility edges in quasiperiodic chains. *Phys. Rev. B*, 103:L060201, Feb 2021.

[43] Carlo Danieli, Joshua D. Bodyfelt, and Sergej Flach. Flat-band engineering of mobility edges. *Phys. Rev. B*, 91:235134, Jun 2015.

[44] Dave J. Boers, Benjamin Goedeke, Dennis Hinrichs, and Martin Holthaus. Mobility edges in bichromatic optical lattices. *Phys. Rev. A*, 75:063404, Jun 2007.

[45] Fangzhao Alex An, Karmela Padavić, Eric J. Meier, Suraj Hegde, Sriram Ganeshan, J. H. Pixley, Smitha Vishveshwara, and Bryce Gadway. Ob-

servation of tunable mobility edges in generalized Aubry-André lattices. *arXiv e-prints*, page arXiv:2007.01393, July 2020.

[46] Fangzhao Alex An, Eric J Meier, and Bryce Gadway. Engineering a flux-dependent mobility edge in disordered zigzag chains. *Phys. Rev. X*, 8(3):031045, 2018.

[47] Fangzhao Alex An, Karmela Padavić, Eric J. Meier, Suraj Hegde, Sriram Ganeshan, J. H. Pixley, Smitha Vishveshwara, and Bryce Gadway. Interactions and mobility edges: Observing the generalized aubry-andré model. *Phys. Rev. Lett.*, 126:040603, Jan 2021.

[48] Thomas Kohlert, Sebastian Scherg, Xiao Li, Henrik P. Lüschen, Sankar Das Sarma, Immanuel Bloch, and Monika Aidelsburger. Observation of many-body localization in a one-dimensional system with a single-particle mobility edge. *Phys. Rev. Lett.*, 122:170403, May 2019.

[49] Henrik P. Lüschen, Sebastian Scherg, Thomas Kohlert, Michael Schreiber, Pranjal Bordia, Xiao Li, S. Das Sarma, and Immanuel Bloch. Single-particle mobility edge in a one-dimensional quasiperiodic optical lattice. *Phys. Rev. Lett.*, 120:160404, Apr 2018.

[50] Ferdinand Evers and Alexander D. Mirlin. Anderson transitions. *Rev. Mod. Phys.*, 80:1355–1417, Oct 2008.

[51] Tong Liu, Xu Xia, Stefano Longhi, and Laurent Sanchez-Palencia. Anomalous mobility edges in one-dimensional quasiperiodic models. *SciPost Phys.*, 12:027, 2022.

[52] Wade DeGottardi, Diptiman Sen, and Smitha Vishveshwara. Majorana fermions in superconducting 1d systems having periodic, quasiperiodic, and disordered potentials. *Phys. Rev. Lett.*, 110:146404, Apr 2013.

[53] Yucheng Wang, Long Zhang, Sen Niu, Dapeng Yu, and Xiong-Jun Liu. Realization and detection of nonergodic critical phases in an optical raman lattice. *Phys. Rev. Lett.*, 125:073204, Aug 2020.

[54] Dmitry A. Abanin, Ehud Altman, Immanuel Bloch, and Maksym Serbyn. Colloquium: Many-body localization, thermalization, and entanglement. *Rev. Mod. Phys.*, 91:021001, May 2019.

[55] Arijeet Pal and David A. Huse. Many-body localization phase transition. *Phys. Rev. B*, 82:174411, Nov 2010.

[56] Bo-Bo Wei. Fidelity susceptibility in one-dimensional disordered lattice models. *Phys. Rev. A*, 99:042117, Apr 2019.

[57] Mahito Kohmoto, Bill Sutherland, and Chao Tang. Critical wave functions and a cantor-set spectrum of a one-dimensional quasicrystal model. *Phys. Rev. B*, 35:1020–1033, Jan 1987.

[58] Chao Tang and Mahito Kohmoto. Global scaling properties of the spectrum for a quasiperiodic schrödinger equation. *Phys. Rev. B*, 34:2041–2044, Aug 1986.

[59] J. H. Han, D. J. Thouless, H. Hiramoto, and M. Kohmoto. Critical and bicritical properties of harper's equation with next-nearest-neighbor coupling. *Phys. Rev. B*, 50:11365–11380, Oct 1994.

[60] Hepeng Yao, Hakim Khoudli, Léa Bresque, and Laurent Sanchez-Palencia. Critical behavior and fractality in shallow one-dimensional quasiperiodic potentials. *Phys. Rev. Lett.*, 123(7):070405, 2019.

[61] Kazuhiro Ikezawa and Mahito Kohmoto. Energy spectrum and the critical wavefunctions of the quasiperiodic harper equation–the silver mean case–. *Journal of the Physical Society of Japan*, 63(6):2261–2268, 1994.

[62] Shankar Iyer, Vadim Oganesyan, Gil Refael, and David A. Huse. Many-body localization in a quasiperiodic system. *Phys. Rev. B*, 87:134202, Apr 2013.

[63] Henrik P. Lüschen, Pranjal Bordia, Sebastian Scherg, Fabien Alet, Ehud Altman, Ulrich Schneider, and Immanuel Bloch. Observation of slow dynamics near the many-body localization transition in one-dimensional quasiperiodic systems. *Phys. Rev. Lett.*, 119:260401, Dec 2017.

[64] Pranjal Bordia, Henrik Lüschen, Sebastian Scherg, Sarang Gopalakrishnan, Michael Knap, Ulrich Schneider, and Immanuel Bloch. Probing slow relaxation and many-body localization in two-dimensional quasiperiodic systems. *Phys. Rev. X*, 7:041047, Nov 2017.

[65] Xiao-Liang Qi and Shou-Cheng Zhang. Topological insulators and superconductors. *Rev. Mod. Phys.*, 83:1057–1110, Oct 2011.

[66] Yaacov E. Kraus and Oded Zilberberg. Topological equivalence between the fibonacci quasicrystal and the harper model. *Phys. Rev. Lett.*, 109:116404, Sep 2012.

[67] Sriram Ganeshan, Kai Sun, and S. Das Sarma. Topological zero-energy modes in gapless commensurate aubry-andré-harper models. *Phys. Rev. Lett.*, 110:180403, May 2013.

[68] Mahito Kohmoto. Metal-insulator transition and scaling for incommensurate systems. *Phys. Rev. Lett.*, 51:1198–1201, Sep 1983.

[69] Konrad Viebahn, Matteo Sbroscia, Edward Carter, Jr-Chiun Yu, and Ulrich Schneider. Matter-wave diffraction from a quasicrystalline optical lattice. *Phys. Rev. Lett.*, 122(11):110404, 2019.

[70] Y. Lahini, R. Pugatch, F. Pozzi, M. Sorel, R. Morandotti, N. Davidson, and Y. Silberberg. Observation of a localization transition in quasiperiodic photonic lattices. *Phys. Rev. Lett.*, 103:013901, Jun 2009.

[71] Mor Verbin, Oded Zilberberg, Yaacov E. Kraus, Yoav Lahini, and Yaron Silberberg. Observation of topological phase transitions in photonic quasicrystals. *Phys. Rev. Lett.*, 110:076403, Feb 2013.

[72] Mor Verbin, Oded Zilberberg, Yoav Lahini, Yaacov E. Kraus, and Yaron Silberberg. Topological pumping over a photonic fibonacci quasicrystal. *Phys. Rev. B*, 91:064201, Feb 2015.

[73] Yaacov E. Kraus, Yoav Lahini, Zohar Ringel, Mor Verbin, and Oded Zilberberg. Topological states and adiabatic pumping in quasicrystals. *Phys. Rev. Lett.*, 109:106402, Sep 2012.

[74] Peng Wang, Yuanlin Zheng, Xianfeng Chen, Changming Huang, Yaroslav V Kartashov, Lluis Torner, Vladimir V Konotop, and Fangwei Ye. Localization and delocalization of light in photonic moiré lattices. *Nature*, 577(7788):42–46, 2020.

[75] Wenting Cheng, Emil Prodan, and Camelia Prodan. Experimental demonstration of dynamic topological pumping across incommensurate bilayered acoustic metamaterials. *Phys. Rev. Lett.*, 125:224301, Nov 2020.

[76] David J. Apigo, Wenting Cheng, Kyle F. Dobiszewski, Emil Prodan, and

Camelia Prodan. Observation of topological edge modes in a quasiperiodic acoustic waveguide. *Phys. Rev. Lett.*, 122:095501, Mar 2019.

[77] D. Tanese, E. Gurevich, F. Baboux, T. Jacqmin, A. Lemaître, E. Galopin, I. Sagnes, A. Amo, J. Bloch, and E. Akkermans. Fractal energy spectrum of a polariton gas in a fibonacci quasiperiodic potential. *Phys. Rev. Lett.*, 112:146404, Apr 2014.

[78] Valentin Goblot, Antonio Štrkalj, Nicolas Pernet, Jose L Lado, C Dorow, Aristide Lemaître, Luc Le Gratiet, Abdelmounaim Harouri, Isabelle Sagnes, Sylvain Ravets, et al. Emergence of criticality through a cascade of delocalization transitions in quasiperiodic chains. *Nature Physics*, 16(8):832–836, 2020.

[79] Leon Balents, Cory R Dean, Dmitri K Efetov, and Andrea F Young. Superconductivity and strong correlations in moiré flat bands. *Nature Physics*, 16(7):725–733, 2020.

[80] Pedram Roushan, Charles Neill, J Tangpanitanon, Victor M Bastidas, A Megrant, Rami Barends, Yu Chen, Z Chen, B Chiaro, A Dunsworth, et al. Spectroscopic signatures of localization with interacting photons in superconducting qubits. *Science*, 358(6367):1175–1179, 2017.

[81] Diederik S Wiersma, Paolo Bartolini, Ad Lagendijk, and Roberto Righini. Localization of light in a disordered medium. *Nature*, 390(6661):671–673, 1997.

[82] Shayan Mookherjea, Jung S Park, Shun-Hui Yang, and Prabhakar R Bandaru. Localization in silicon nanophotonic slow-light waveguides. *Nature Photonics*, 2(2):90–93, 2008.

[83] Sanli Faez, Anatoliy Strybulevych, John H Page, Ad Lagendijk, and Bart A van Tiggelen. Observation of multifractality in anderson localization of ultrasound. *Physical review letters*, 103(15):155703, 2009.

[84] Hefei Hu, A Strybulevych, JH Page, Sergey E Skipetrov, and Bart A van Tiggelen. Localization of ultrasound in a three-dimensional elastic network. *Nature Physics*, 4(12):945–948, 2008.

[85] R. Dalichaouch, JP Armstrong, S. Schultz, PM Platzman, and SL McCall. Microwave localization by two-dimensional random scattering. *Nature*, 354(6348):53–55, 1991.

[86] Anthony Richardella, Pedram Roushan, Shawn Mack, Brian Zhou, David A Huse, David D Awschalom, and Ali Yazdani. Visualizing critical correlations near the metal-insulator transition in ga1-x mn x as. *science*, 327(5966):665–669, 2010.

[87] K Hashimoto, C Sohrmann, J Wiebe, T Inaoka, F Meier, Y Hirayama, RA Römer, R Wiesendanger, and M Morgenstern. Quantum hall transition in real space: from localized to extended states. *Physical Review Letters*, 101(25):256802, 2008.

[88] Klaus Drese and Martin Holthaus. Exploring a metal-insulator transition with ultracold atoms in standing light waves? *Phys. Rev. Lett.*, 78:2932–2935, Apr 1997.

[89] Alain Aspect and Massimo Inguscio. Anderson localization of ultracold atoms. *Phys. Today*, 62(8):30, 2009.

[90] Yoav Lahini, Assaf Avidan, Francesca Pozzi, Marc Sorel, Roberto Morandotti, Demetrios N Christodoulides, and Yaron Silberberg. Anderson localization and nonlinearity in one-dimensional disordered photonic lattices. *Phys. Rev. Lett.*, 100(1):013906, 2008.

[91] L. Fallani, J. E. Lye, V. Guarrera, C. Fort, and M. Inguscio. Ultracold atoms in a disordered crystal of light: Towards a bose glass. *Phys. Rev. Lett.*, 98:130404, Mar 2007.

[92] Tal Schwartz, Guy Bartal, Shmuel Fishman, and Mordechai Segev. Transport and anderson localization in disordered two-dimensional photonic lattices. *Nature*, 446(7131):52–55, 2007.

[93] D. J Thouless. Electrons in disordered systems and the theory of localization. *Physics Reports*, 13(3):93–142, 1974.

[94] Steven Chu. Nobel lecture: The manipulation of neutral particles. *Reviews of Modern Physics*, 70(3):685, 1998.

[95] Claude N Cohen-Tannoudji. Nobel lecture: Manipulating atoms with photons. *Reviews of Modern Physics*, 70(3):707, 1998.

[96] William D Phillips. Nobel lecture: Laser cooling and trapping of neutral atoms. *Reviews of Modern Physics*, 70(3):721, 1998.

[97] Rudolf Grimm, Matthias Weidemüller, and Yurii B Ovchinnikov. Optical dipole traps for neutral atoms. In *Advances in atomic, molecular, and optical physics*, volume 42, pages 95–170. Elsevier, 2000.

[98] Richard I Epstein, Melvin I Buchwald, Bradley C Edwards, Timothy R Gosnell, and Carl E Mungan. Observation of laser-induced fluorescent cooling of a solid. *Nature*, 377(6549):500–503, 1995.

[99] Serge Aubry and Gilles André. Analyticity breaking and anderson localization in incommensurate lattices. *Ann. Israel Phys. Soc*, 3(133):18, 1980.

[100] Svetlana Ya. Jitomirskaya. Metal-insulator transition for the almost mathieu operator. *Annals of Mathematics*, 150(3):1159–1175, 1999.

[101] Xiao Li, Xiaopeng Li, and S. Das Sarma. Mobility edges in one-dimensional bichromatic incommensurate potentials. *Phys. Rev. B*, 96:085119, Aug 2017.

[102] Xiao Li and S. Das Sarma. Mobility edge and intermediate phase in one-dimensional incommensurate lattice potentials. *Phys. Rev. B*, 101:064203, Feb 2020.

[103] Y Hashimoto, K Niizeki, and Y Okabe. A finite-size scaling analysis of the localization properties of one-dimensional quasiperiodic systems. *Journal of Physics A: Mathematical and General*, 25(20):5211–5221, oct 1992.

[104] M. Z. Hasan and C. L. Kane. Colloquium: Topological insulators. *Rev. Mod. Phys.*, 82:3045–3067, Nov 2010.

[105] A. Bansil, Hsin Lin, and Tanmoy Das. Colloquium: Topological band theory. *Rev. Mod. Phys.*, 88:021004, Jun 2016.

[106] M Zahid Hasan and Charles L Kane. Colloquium: topological insulators. *Reviews of modern physics*, 82(4):3045, 2010.

[107] Masatoshi Sato and Yoichi Ando. Topological superconductors: a review. *Reports on Progress in Physics*, 80(7):076501, may 2017.

[108] W. P. Su, J. R. Schrieffer, and A. J. Heeger. Solitons in polyacetylene. *Phys. Rev. Lett.*, 42:1698–1701, Jun 1979.

[109] Sankar Das Sarma, Michael Freedman, and Chetan Nayak. Topologically protected qubits from a possible non-abelian fractional quantum hall state. *Phys. Rev. Lett.*, 94:166802, Apr 2005.

[110] Chetan Nayak, Steven H. Simon, Ady Stern, Michael Freedman, and Sankar Das Sarma. Non-abelian anyons and topological quantum computation. *Rev. Mod. Phys.*, 80:1083–1159, Sep 2008.

[111] Jason Alicea. New directions in the pursuit of majorana fermions in solid state systems. *Reports on Progress in Physics*, 75(7):076501, jun 2012.

[112] Steven R. Elliott and Marcel Franz. Colloquium: Majorana fermions in nuclear, particle, and solid-state physics. *Rev. Mod. Phys.*, 87:137–163, Feb 2015.

[113] A Yu Kitaev. Unpaired majorana fermions in quantum wires. *Physics-Uspekhi*, 44(10S):131–136, oct 2001.

[114] Ryohei Wakatsuki, Motohiko Ezawa, Yukio Tanaka, and Naoto Nagaosa. Fermion fractionalization to majorana fermions in a dimerized kitaev superconductor. *Phys. Rev. B*, 90:014505, Jul 2014.

[115] M. Yahyavi, B. Hetényi, and B. Tanatar. Generalized aubry-andré-harper model with modulated hopping and *p*-wave pairing. *Phys. Rev. B*, 100:064202, Aug 2019.

[116] Doru Sticlet, Luis Seabra, Frank Pollmann, and Jérôme Cayssol. From fractionally charged solitons to majorana bound states in a one-dimensional interacting model. *Phys. Rev. B*, 89:115430, Mar 2014.

[117] Yuxuan Wang, Mao Lin, and Taylor L. Hughes. Weak-pairing higher order topological superconductors. *Phys. Rev. B*, 98:165144, Oct 2018.

[118] Yuval Oreg, Gil Refael, and Felix von Oppen. Helical liquids and majorana bound states in quantum wires. *Phys. Rev. Lett.*, 105:177002, Oct 2010.

[119] Jay D. Sau, Sumanta Tewari, Roman M. Lutchyn, Tudor D. Stanescu, and S. Das Sarma. Non-abelian quantum order in spin-orbit-coupled semiconductors: Search for topological majorana particles in solid-state systems. *Phys. Rev. B*, 82:214509, Dec 2010.

[120] Önder Gül, Hao Zhang, Jouri DS Bommer, Michiel WA de Moor, Diana Car, Sébastien R Plissard, Erik PAM Bakkers, Attila Geresdi, Kenji Watanabe, Takashi Taniguchi, et al. Ballistic majorana nanowire devices. *Nature nanotechnology*, 13(3):192–197, 2018.

[121] Vincent Mourik, Kun Zuo, Sergey M Frolov, SR Plissard, Erik PAM Bakkers, and Leo P Kouwenhoven. Signatures of majorana fermions in hybrid superconductor-semiconductor nanowire devices. *Science*, 336(6084):1003–1007, 2012.

[122] Roman M Lutchyn, Erik PAM Bakkers, Leo P Kouwenhoven, Peter Krogstrup, Charles M Marcus, and Yuval Oreg. Majorana zero modes in superconductor–semiconductor heterostructures. *Nature Reviews Materials*, 3(5):52–68, 2018.

[123] Sangjun Jeon, Yonglong Xie, Jian Li, Zhijun Wang, B Andrei Bernevig, and Ali Yazdani. Distinguishing a majorana zero mode using spin-resolved measurements. *Science*, 358(6364):772–776, 2017.

[124] Benjamin E Feldman, Mallika T Randeria, Jian Li, Sangjun Jeon, Yonglong Xie, Zhijun Wang, Ilya K Drozdov, B Andrei Bernevig, and Ali Yazdani. High-resolution studies of the majorana atomic chain platform. *Nature Physics*, 13(3):286–291, 2017.

[125] Michael Ruby, Benjamin W Heinrich, Yang Peng, Felix von Oppen, and Katharina J Franke. Exploring a proximity-coupled co chain on pb (110) as a possible majorana platform. *Nano letters*, 17(7):4473–4477, 2017.

[126] T Andrews. Xviii. the bakerian lecture.—on the continuity of the gaseous and liquid states of matter. *Phil. Trans. R. Soc.*, (159):575–590, 1869.

[127] B Widom. Surface tension and molecular correlations near the critical point. *The Journal of Chemical Physics*, 43(11):3892–3897, 1965.

[128] M Vojta. Quantum phase transitions. *Reports on Progress in Physics*, 66(12):2069, 2003.

[129] C Kittel. Semiconductor band gaps. *Introduction to Solid State Physics, 6th Ed., New York: John Wiley*, page 185, 1986.

[130] M V Berry. Quantal phase factors accompanying adiabatic changes. *Pro-*

ceedings of the Royal Society of London. A. Mathematical and Physical Sciences, 392(1802):45–57, 1984.

[131] Ian Mondragon-Shem, Taylor L. Hughes, Juntao Song, and Emil Prodan. Topological criticality in the chiral-symmetric aiii class at strong disorder. *Phys. Rev. Lett.*, 113:046802, Jul 2014.

[132] Ling-Zhi Tang, Shu-Na Liu, Guo-Qing Zhang, and Dan-Wei Zhang. Topological anderson insulators with different bulk states in quasiperiodic chains. *Phys. Rev. A*, 105:063327, Jun 2022.

[133] J Hubbard. Electron correlations in narrow energy bands. ii. the degenerate band case. *Proceedings of the Royal Society of London. Series A. Mathematical and Physical Sciences*, 277(1369):237–259, 1964.

[134] Matthew P. A. Fisher, Peter B. Weichman, G. Grinstein, and Daniel S. Fisher. Boson localization and the superfluid-insulator transition. *Phys. Rev. B*, 40:546–570, Jul 1989.

[135] D. Jaksch, C. Bruder, J. I. Cirac, C. W. Gardiner, and P. Zoller. Cold bosonic atoms in optical lattices. *Phys. Rev. Lett.*, 81:3108–3111, Oct 1998.

[136] I Bloch, J Dalibard, and W Zwerger. Many-body physics with ultracold gases. *Rev. Mod. Phys.*, 80:885–964, Jul 2008.

[137] D. van Oosten, D. B. M. Dickerscheid, B. Farid, P. van der Straten, and H. T. C. Stoof. Inelastic light scattering from a mott insulator. *Phys. Rev. A*, 71:021601, Feb 2005.

[138] CM Soukoulis and EN Economou. Localization in one-dimensional lattices in the presence of incommensurate potentials. *Phys. Rev. Lett.*, 48(15):1043, 1982.

[139] Shilpi Roy and Saurabh Basu. Interplay of off-diagonal random disorder and quasiperiodic potential in a one-dimensional aubry-andré model. *EPL (Europhysics Letters)*, 128(4):47005, 2020.

[140] Shilpi Roy, Tapan Mishra, B. Tanatar, and Saurabh Basu. Reentrant localization transition in a quasiperiodic chain. *Phys. Rev. Lett.*, 126:106803, Mar 2021.

[141] Ian Mondragon-Shem, Taylor L. Hughes, Juntao Song, and Emil Prodan.

Topological criticality in the chiral-symmetric aiii class at strong disorder. *Phys. Rev. Lett.*, 113:046802, Jul 2014.

[142] Christoph Jürß and Dieter Bauer. High-harmonic generation in su-schrieffer-heeger chains. *Phys. Rev. B*, 99:195428, May 2019.

[143] F Munoz, Fernanda Pinilla, J Mella, and Mario I Molina. Topological properties of a bipartite lattice of domain wall states. *Scientific reports*, 8(1):1–9, 2018.

[144] Myles Scollon and Malcolm P. Kennett. Persistence of chirality in the su-schrieffer-heeger model in the presence of on-site disorder. *Phys. Rev. B*, 101:144204, Apr 2020.

[145] Beatriz Pérez-González, Miguel Bello, Álvaro Gómez-León, and Gloria Platero. Interplay between long-range hopping and disorder in topological systems. *Phys. Rev. B*, 99:035146, Jan 2019.

[146] Tong Liu and Hao Guo. Topological phase transition in the quasiperiodic disordered su–schriffer–heeger chain. *Physics Letters A*, 382(45):3287 – 3292, 2018.

[147] With a configuration where λ has a positive sign at the leftmost site and a negative sign at the rightmost site of the chain.

[148] Lohse M., Schweizer C., Zilberberg O., Aidelsburger M., and Bloch I. A thouless quantum pump with ultracold bosonic atoms in an optical superlattice. *Nature Physics*, 12:350, dec 2015.

[149] Sylvain de Léséleuc, Vincent Lienhard, Pascal Scholl, Daniel Barredo, Sebastian Weber, Nicolai Lang, Hans Peter Büchler, Thierry Lahaye, and Antoine Browaeys. Observation of a symmetry-protected topological phase of interacting bosons with rydberg atoms. *Science*, 365(6455):775–780, 2019.

[150] Henrik P. Lüschen, Sebastian Scherg, Thomas Kohlert, Michael Schreiber, Pranjal Bordia, Xiao Li, S. Das Sarma, and Immanuel Bloch. Single-particle mobility edge in a one-dimensional quasiperiodic optical lattice. *Phys. Rev. Lett.*, 120:160404, Apr 2018.

[151] Shuta Nakajima, Nobuyuki Takei, Keita Sakuma, Yoshihito Kuno, Pasquale Marra, and Yoshiro Takahashi. Disorder-induced Thouless

pumping of ultracold atoms in an optical lattice. *arXiv e-prints*, page arXiv:2007.06817, July 2020.

[152] Shilpi Roy, Sourav Chattopadhyay, Tapan Mishra, and Saurabh Basu. Critical analysis of the reentrant localization transition in a one-dimensional dimerized quasiperiodic lattice. *Physical Review B*, 105(21):214203, 2022.

[153] Alexander Altland, Dmitry Bagrets, Lars Fritz, Alex Kamenev, and Hanno Schmiedt. Quantum criticality of quasi-one-dimensional topological anderson insulators. *Phys. Rev. Lett.*, 112:206602, May 2014.

[154] Suhas Gangadharaiah, Bernd Braunecker, Pascal Simon, and Daniel Loss. Majorana edge states in interacting one-dimensional systems. *Phys. Rev. Lett.*, 107:036801, Jul 2011.

[155] Olexei Motrunich, Kedar Damle, and David A. Huse. Griffiths effects and quantum critical points in dirty superconductors without spin-rotation invariance: One-dimensional examples. *Phys. Rev. B*, 63:224204, May 2001.

[156] Xiaoming Cai, Li-Jun Lang, Shu Chen, and Yupeng Wang. Topological superconductor to anderson localization transition in one-dimensional incommensurate lattices. *Phys. Rev. Lett.*, 110:176403, Apr 2013.

[157] Yucheng Wang, Jian-Jian Miao, Hui-Ke Jin, and Shu Chen. Characterization of topological phases of dimerized kitaev chain via edge correlation functions. *Phys. Rev. B*, 96:205428, Nov 2017.

[158] Motohiko Ezawa. Exact solutions and topological phase diagram in interacting dimerized kitaev topological superconductors. *Phys. Rev. B*, 96:121105, Sep 2017.

[159] Gennady Y. Chitov. Local and nonlocal order parameters in the kitaev chain. *Phys. Rev. B*, 97:085131, Feb 2018.

[160] Jian Li, Rui-Lin Chu, J. K. Jain, and Shun-Qing Shen. Topological anderson insulator. *Phys. Rev. Lett.*, 102:136806, Apr 2009.

[161] C. W. Groth, M. Wimmer, A. R. Akhmerov, J. Tworzydło, and C. W. J. Beenakker. Theory of the topological anderson insulator. *Phys. Rev. Lett.*, 103:196805, Nov 2009.

[162] Kai Li, Jiong-Hao Wang, Yan-Bin Yang, and Yong Xu. Symmetry-protected topological phases in a rydberg glass. *Phys. Rev. Lett.*, 127:263004, Dec 2021.

[163] Weixuan Zhang, Deyuan Zou, Qingsong Pei, Wenjing He, Jiacheng Bao, Houjun Sun, and Xiangdong Zhang. Experimental observation of higher-order topological anderson insulators. *Phys. Rev. Lett.*, 126:146802, Apr 2021.

[164] Gui-Geng Liu, Yihao Yang, Xin Ren, Haoran Xue, Xiao Lin, Yuan-Hang Hu, Hong-xiang Sun, Bo Peng, Peiheng Zhou, Yidong Chong, and Baile Zhang. Topological anderson insulator in disordered photonic crystals. *Phys. Rev. Lett.*, 125:133603, Sep 2020.

[165] Takuya Okugawa, Tanay Nag, and Dante M. Kennes. Correlated disorder induced anomalous transport in magnetically doped topological insulators. *Phys. Rev. B*, 106:045417, Jul 2022.

[166] Chun-Bo Hua, Rui Chen, Dong-Hui Xu, and Bin Zhou. Disorder-induced majorana zero modes in a dimerized kitaev superconductor chain. *Phys. Rev. B*, 100:205302, Nov 2019.

[167] Shilpi Roy, Sk Noor Nabi, and Saurabh Basu. Critical and topological phases of dimerized kitaev chain in presence of quasiperiodic potential. *arXiv preprint arXiv:2209.06255*, 2022.

[168] Benjamin Blaß, Heiko Rieger, Gerg ő Roósz, and Ferenc Iglói. Quantum relaxation and metastability of lattice bosons with cavity-induced long-range interactions. *Phys. Rev. Lett.*, 121:095301, Aug 2018.

[169] Markus Greiner, Olaf Mandel, Tilman Esslinger, Theodor W. Hänsch, and Immanuel Bloch. Quantum phase transition from a superfluid to a mott insulator in a gas of ultracold atoms. *Nature*, 415(6867):39–44, Jan 2002.

[170] M. White, M. Pasienski, D. McKay, S. Q. Zhou, D. Ceperley, and B. DeMarco. Strongly interacting bosons in a disordered optical lattice. *Phys. Rev. Lett.*, 102:055301, Feb 2009.

[171] Carolyn Meldgin, Ushnish Ray, Philip Russ, David Chen, David M. Ceperley, and Brian DeMarco. Probing the bose glass–superfluid transition using quantum quenches of disorder. *Nature Physics*, 12(7):646–649, Jul 2016.

[172] J. E. Lye, L. Fallani, M. Modugno, D. S. Wiersma, C. Fort, and M. Inguscio. Bose-einstein condensate in a random potential. *Phys. Rev. Lett.*, 95:070401, Aug 2005.

[173] M. Pasienski, D. McKay, M. White, and B. DeMarco. A disordered insulator in an optical lattice. *Nature Physics*, 6(9):677–680, Sep 2010.

[174] S. Ospelkaus, C. Ospelkaus, O. Wille, M. Succo, P. Ernst, K. Sengstock, and K. Bongs. Localization of bosonic atoms by fermionic impurities in a three-dimensional optical lattice. *Phys. Rev. Lett.*, 96:180403, May 2006.

[175] Ronan Gautier, Hepeng Yao, and Laurent Sanchez-Palencia. Strongly interacting bosons in a two-dimensional quasicrystal lattice. *Phys. Rev. Lett.*, 126:110401, Mar 2021.

[176] Hepeng Yao, Thierry Giamarchi, and Laurent Sanchez-Palencia. Lieb-liniger bosons in a shallow quasiperiodic potential: Bose glass phase and fractal mott lobes. *Phys. Rev. Lett.*, 125:060401, Aug 2020.

[177] Chao Zhang and Heiko Rieger. Phase diagrams of the disordered bose-hubbard model with cavity-mediated long-range and nearest-neighbor interactions. *The European Physical Journal B*, 93(2):1–7, 2020.

[178] C. Zhang, A. Safavi-Naini, and B. Capogrosso-Sansone. Equilibrium phases of two-dimensional bosons in quasiperiodic lattices. *Phys. Rev. A*, 91:031604, Mar 2015.

[179] Dean Johnstone, Patrik Öhberg, and Callum W Duncan. The mean-field bose glass in quasicrystalline systems. *Journal of Physics A: Mathematical and Theoretical*, 54(39):395001, sep 2021.

[180] Dean Johnstone, Patrik Öhberg, and Callum W Duncan. Barriers to macroscopic superfluidity and insulation in a 2d aubry–andré model. *Journal of Physics B: Atomic, Molecular and Optical Physics*, 55(12):125302, may 2022.

[181] Yancheng Wang, Wenan Guo, and Anders W. Sandvik. Anomalous quantum glass of bosons in a random potential in two dimensions. *Phys. Rev. Lett.*, 114:105303, Mar 2015.

[182] X. Deng, R. Citro, E. Orignac, and A. Minguzzi. Superfluidity and an-

derson localisation for a weakly interacting bose gas in a quasiperiodic potential. *The European Physical Journal B*, 68(3):435–443, Apr 2009.

[183] Serge Lang. *Introduction to Diophantine Approximations*. Springer-Verlag, 1995.

[184] *M can be obtained via continued fraction approximation as discussed in Ref.[183].*

[185] Ramesh V. Pai, Jamshid Moradi Kurdestany, K. Sheshadri, and Rahul Pandit. Bose-hubbard models in confining potentials: Inhomogeneous mean-field theory. *Phys. Rev. B*, 85:214524, Jun 2012.

[186] D. van Oosten, P. van der Straten, and H. T. C. Stoof. Quantum phases in an optical lattice. *Phys. Rev. A*, 63:053601, Apr 2001.

[187] Sk Noor Nabi, Shilpi Roy, and Saurabh Basu. Phase properties of interacting bosons in presence of quasiperiodic and random potential. *Annals of Physics*, 448:169171, 2023.

[188] Barman, A., Dutta, S., Khan, A., and Basu, S. Understanding the bose glass phase via a percolation scenario. *Eur. Phys. J. B*, 86(7):308, 2013.

[189] Sk Noor Nabi and Saurabh Basu. Percolation analysis of a disordered spinor bose gas. *Journal of Physics B: Atomic, Molecular and Optical Physics*, 49(12):125301, may 2016.

[190] D. Stauffer and A. Aharony. *Introduction To Percolation Theory*. Taylor & Francis, 1994.

[191] J. Hoshen and R. Kopelman. Percolation and cluster distribution. i. cluster multiple labeling technique and critical concentration algorithm. *Phys. Rev. B*, 14:3438–3445, Oct 1976.

[192] Bappaditya Roy and S.B. Santra. Finite size scaling study of a two parameter percolation model: Constant and correlated growth. *Physica A: Statistical Mechanics and its Applications*, 492:969–979, 2018.

[193] Bappaditya Roy and S. B. Santra. First-order transition in a percolation model with nucleation and preferential growth. *Phys. Rev. E*, 95:010101, Jan 2017.

[194] A E Niederle and H Rieger. Superfluid clusters, percolation and phase transitions in the disordered, two-dimensional bose–hubbard model. *New Journal of Physics*, 15(7):075029, jul 2013.